6GSNS

Co-funded by the European Union

SEamless integratioN of efficient 6G WirelesS tEchnologies for Communication and Sensing

D3.2 Final report on the development of 6G-SENSES infrastructure building blocks

January 2026

6G-SENSES project has received funding from the Smart Networks and Services Joint Undertaking (SNS JU) under the European Union's Horizon Europe research and innovation programme under Grant Agreement 101139282

Project Start Date: 2024-01-01 **Duration**: 30 months

Call: HORIZON-JU-SNS-2023 **Date of delivery**: 2026-01-09

Topic: HORIZON-JU-SNS-2023-STREAM-B-01-02 **Version**: 1.0

Type: Report (R)

Grant Agreement Number:	101139282
Project Name:	SEamless integratioN of efficient 6G WirelesS tEchnologies for Communication and Sensing
Project Acronym:	6G-SENSES
Document Number:	**D3.2**
Document Title:	Final report on the development of 6G-SENSES infrastructure building blocks
Version:	1.0
Delivery Date:	2025-12-31 (**2026-01-09**)
Responsible:	TU Braunschweig (**TUBS**)
Editor(s):	Eduard Jorswieck, Xi Ding (**TUBS**)
Authors:	Xi Ding, Malte Eggers, Eduard Jorswieck (**TUBS**), Jessica Sanson, Yazhou Zhu (**INT**), Diego Cuevas, Jesús Ibáñez, Ignacio Santamaría (**UC**), Vladica Sark, Mert Özates, Batuhan Sütbas, Jesús Gutiérrez (**IHP**), Chieh-Chun Chen, Mikel Irazabal, Khai Nguyen, Navid Nikaein (**BR**), Muhammad Umar, Muhammad Sajjad Ahmad, Padmanava Sen (**BI**), Muhammad Saadi, Shahid Mumtaz (**NTU**).
Keywords:	Wireless Access Technologies (WATs), Integrated Sensing and Communication (ISAC), Software Defined Radio (SDR), Cell-Free MIMO (CF-MIMO), Analog Front-End (AFE), Programmable Platforms, Open RAN (O-RAN).
Status:	Final
Dissemination Level	Public (PU)
Project URL:	https://www.6g-senses.eu

Revision History

Rev. N	Description	Author	Date
0.0	Draft Table of Contents (ToC)	Xi Ding (TUBS)	2025-10-30
0.1	Initial contributions to Chapter 2	Vladica Sark, Jesús Gutiérrez, Batuhan Sütbas (IHP) Muhammad Umar, Muhammad Sajjad Ahmad, Padmanava Sen (BI), Jessica Sanson, Yazhou Zhu (INT)	2025-11-10
0.15	Initial contributions to Chapter 4	Diego Cuevas, Jesús Ibáñez, Ignacio Santamaría (UC)	2025-11-10
0.2	Initial contributions to Chapter 3	Xi Ding, Malte Eggers, Eduard Jorswieck (TUBS), Mert Özates (IHP)	2025-11-10
0.3	Final contributions to Chapter 3	Xi Ding, Malte Eggers, Eduard Jorswieck (TUBS), Mert Özates (IHP)	2025-11-30
0.4	Final contributions to Chapter 4	Ignacio Santamaría (UC), Muhammad Saadi, Shahid Mumtaz (NTU)	2025-11-25
0.45	Final contributions to Chapter 2	Vladica Sark, Jesús Gutiérrez (IHP), Chieh-Chun Chen, Mikel Irazabal, Khai Nguyen, Navid Nikaein (BR), Vladica Sark, Jesús Gutiérrez, Batuhan Sütbas (IHP) Muhammad Umar, Muhammad Sajjad Ahmad, Padmanava Sen (BI), Jessica Sanson, Yazhou Zhu (INT)	2025-12-10
0.5	Final Technical Review	Ignacio Santamaría (UC), Eduard Jorswieck (TUBS)	2025-12-20
0.6	Final Review	Valerio Frascolla (INT)	2025-12-22
1.0	Last revision and submission of the document	Jesús Gutiérrez (IHP)	2026-01-09

Table of Contents

LIST OF FIGURES **6**

LIST OF TABLES **8**

EXECUTIVE SUMMARY **9**

1. INTRODUCTION **10**

1.1 Organization of the document **10**

2. ISAC ACTIVITIES **11**

2.1 Update of the ISAC platforms **11**
2.1.1 Wi-Fi subsystem design 11
2.1.2 Sub-6 13
2.1.3 mmWave 15
2.1.4 5G NR 16

2.2 Analog mmWave Front-End for ISAC **20**
2.2.1 Analog front-end chipset 21
2.2.2 Antenna-in-package 23
2.2.3 Benchmarking of 6G-SENSES ISAC chip 27

2.3 6G-SENSES ISAC Experimental Evaluation **28**
2.3.1 6G-SENSES PoC Target implementation 28
2.3.2 6G-SENSES OTFS-ISAC implementation 28

3. CELL-FREE MIMO ACTIVITIES **36**

3.1 CF-MIMO Implementation **36**
3.1.1 Configurations of the CF-MIMO platform 36
3.1.2 Simulation of the CF-MIMO Configurations 40

3.2 Unsourced Random Access in CF-mMIMO **41**

4. RIS SUPPORT FOR IMPROVED SPECTRAL AND ENERGY EFFICIENCY **45**

4.1 Introduction and outlook **45**

4.2 RIS simulation results **45**
4.2.1 RIS architectures 47
4.2.2 Spectral efficiency maximization in BD-RIS-assisted MIMO systems 48
4.2.3 Energy efficiency maximization in MU-MIMO systems 49
4.2.4 SE/EE trade-off region 51
4.2.5 RIS-aided RSMA for URLLC networks 52
4.2.6 Multi-RIS models 52

4.3 Laboratory Implementation of RIS-assisted CF-mMIMO 54

5. CONCLUSIONS 57

6. REFERENCES 58

7. ACRONYMS 63

List of Figures

Figure 2-1 Wi-Fi LiveSensing platform 12
Figure 2-2 a) Sensing with dynamic background modelling, b) sensing without background modelling 14
Figure 2-3 5G SA architecture with SDR-based sensing devices 15
Figure 2-4 a) Xilinx RFSoC ZCU 111 board with SDR functionality and HW implemented real-time OFDM baseband processor, b) 60 GHz dual-module full-duplex RF frontend 16
Figure 2-5 O-RAN integration into the 5G NR RAN 17
Figure 2-6 MX-RIC Block Diagram 18
Figure 2-7 Block diagram of Scenario 1 implementation 18
Figure 2-8 When UE is connected to gNB-DU-1 19
Figure 2-9 After handover to gNB-DU-2 19
Figure 2-10 Block diagram of Scenario 2 implementation 20
Figure 2-11 Micrographs of the fabricated 30-GHz DA and 60-GHz PA blocks 21
Figure 2-12 Measurement setup with the BPSK modulator probed and the key measured results at 60 GHz with 500 Mb/s 21
Figure 2-13 Measurement setup, TRx IC mounted on a carrier board for small- and large-signal tests, and the key measured results 22
Figure 2-14 Micrograph of the VCO and the measured tuning range and phase noise 23
Figure 2-15 Micrograph of the programmable divider and its measured phase noise when combined with the VCO 23
Figure 2-16 a) 60 GHz transceiver chip pad structure, b) simulated response with two different EM solvers (AWR Axiem and AWR Analyst) 24
Figure 2-17 3D simulation setup for the under development 60 GHz transceiver. Chipset mounted on a PCB with uncompensated chip-to-PCB bondwire interconnect and its simulation response 24
Figure 2-18 Simulation setup for the developed bondwire-inductance compensation with an auxiliary bondwire and PCB pad and its simulation response. 25
Figure 2-19 Proposed PCB stack-up for 60 GHz front-end module 25
Figure 2-20 Bondwire parasitic compensation networks through LCL approach: (a) with auxiliary bondwire and (b) with DGS structure. 26
Figure 2-21 Developed mmWave antenna elements. (a) inset feed, (b) aperture coupled metamaterial gain boosting lens and (c) dual port for simultaneous transmit receiver operation 27
Figure 2-22 Implementation of the 6G-SENSES architecture for PoC#1 28
Figure 2-23 SDR-based OTFS system for an indoor office environment 30
Figure 2-24 OTFS SDR System in indoor Office Environment 31
Figure 2-25 Results of Experiment 1: (a) Resulting BER vs. Rx Gain. (b) Resulting EVM vs. Rx Gain. (c) Resulting EVM vs. Rx Gain at different Rx gains 32
Figure 2-26 Results of Experiment 2. All of the selected modulation schemes are successfully recovered at receiver. 32

Figure 2-27 Office Scenario used for the sensing evaluation of OTFS 34
Figure 2-28 Sensing results in Office scenario: (a) single target, (b) two targets..... 34
Figure 2-29 a) Anechoic chamber test for a single target, b) Office scenario test for a single target 35
Figure 3-1 Massive MIMO System for CF-MIMO – Setup 36
Figure 3-2 Configuration A: Two RUs serve two different UEs separately through beamforming 37
Figure 3-3 Configuration B: both RU_1 and RU_2 are serving UE_1 and UE_2 on the same RB 38
Figure 3-4 Configuration C: both RUs serve both UEs with different beams, accounting for synchronization and phase offsets 39
Figure 3-5 Comparison of Sum-Rate versus SINR for the three configurations 40
Figure 3-6 An illustration of the decoding process of the proposed scheme with two BSs and one CPU [27] 41
Figure 3-7 Comparison of PUPE versus the number of active users for different BS configurations 42
Figure 3-8 Comparison of PUPE between different cooperation levels..... 42
Figure 3-9 PUPE comparison of proposed scheme with and without blockage for $\boldsymbol{\gamma = 0.15, 0.3}$. 43
Figure 3-10 Comparison of the required $\boldsymbol{Eb/N0}$ versus the number of active users for PUPE $\mathbf{Pe \leq 0.05}$.. 43
Figure 4-1 Multi-cell RIS-assisted MU-MIMO broadcast channel 46
Figure 4-2 Diagonal-RIS (left), Beyond-diagonal RIS or BD-RIS (center), and Simultaneous Transmitting and Receiving RIS or STAR-RIS (right) architectures, indicating the constraints on the scattering matrix..... 47
Figure 4-3 BD-RIS-assisted MIMO link. The left panel shows a typical deployment with the BD-RIS strategically deployed to have a dominant path (Ricean channels). The right panel shows the scenario used in the simulations. 48
Figure 4-4 Rate (left panel) and computational complexity (right panel) vs number of BD-RIS elements in a 4x4 MIMO link 49
Figure 4-5 Energy-Efficiency vs. packet length (left) and decoding error probability (right) in a RIS-aided MU-MIMO system. The architecture is a STAR-RIS with M=60 elements operating in a mode-switching scheme. 51
Figure 4-6 Left) Max-min energy efficiency vs. Max-min rate for different RIS architectures in a multi-cell downlink channel with 2 BSs and K=2 UEs per cell. Right) Max-min energy efficiency vs. static power consumption per tunable circuit. 52
Figure 4-7 Multi-RIS scenario 53
Figure 4-8 left) Achievable rate of the different channel models versus d (Tx-Rx distance on the x-axis) for a fixed dRIS = 0.5 [m]. right) Achievable rate of the different channel models versus dRIS (distance between RISs on the y-axis) for a fixed d=8 [m]. 53
Figure 4-9 a) View from the transmitter side, b) View from the receiver side 54
Figure 4-10 a) View from the transmitter side, b) View from the first RIS side, c) View from the second RIS side 55
Figure 4-11 Results for all link configuration cases 56

List of Tables

Table 2-1 Benchmark of the 6G-SENSES V-Band ISAC chip 27

Table 2-2 System Constraints 30

Table 2-3 System constraints for the experiments 31

Table 2-4 System Parameters 33

Table 4-1 Summary of RIS architectures, considered scenarios, and optimization metrics (KPIs) indicating the references of the papers where they have been studied in detail 46

Executive Summary

Deliverable **D3.2** is the final report of Work Package 3 (**WP3**) within the 6G-SENSES project. It consolidates the design, implementation, and evaluation of the data-plane infrastructure building blocks developed to support advanced communication and sensing capabilities in the project. Building upon the initial outcomes reported in deliverable **D3.1**, this document provides a mature and integrated view of **WP3** technologies and their readiness for integration and experimental validation in **WP5**.

Since the release of deliverable **D3.1**, significant design updates and refinements have been carried out across all **WP3** activities. In particular, the initial architectural concepts and early implementations have been extended toward more complete, scalable, and hardware-oriented solutions, addressing practical aspects such as real-time operation, distributed processing, and system-level integration.

WP3 has achieved substantial technical progress in the areas of Integrated Sensing and Communication (ISAC), Cell-Free MIMO (CF-MIMO), and Reconfigurable Intelligent Surface (RIS) technologies. These developments include the design and evaluation of ISAC waveforms and signal processing techniques, distributed CF-MIMO PHY-layer implementations, and RIS-assisted communication and sensing solutions, targeting improvements in coverage, spectral efficiency, and energy efficiency.

The developments have reached a level of maturity that enables their use as technical inputs for the PoC activities described in deliverable **D5.1**. The outcomes presented in this deliverable therefore constitute the technological foundation for the experimental validation phase of the project, complemented with **WP4** solutions for higher layer developments.

Overall, **D3.2** provides a consolidated and final description of the **WP3** infrastructure building blocks, ensuring coherence with the 6G-SENSES system architecture and enabling a smooth transition toward experimental validation.

1. Introduction

The 6G-SENSES project targets the design and validation of a flexible 6G wireless infrastructure, enabling future 6G services through the joint exploitation of communication and sensing. The project follows a multi-layer architecture aligned with O-RAN principles, supporting advanced data-plane technologies, intelligent control, and experimental validation [1], [2].

Deliverable **D3.2** is the final report of **WP3** and consolidates the results introduced in deliverable **D3.1** [3]. Its objective is to provide a mature and integrated description of the PHY-layer technologies, signal processing algorithms, and platform implementations developed within **WP3**.

This document is structured around three technology pillars: ISAC activities focusing on waveforms, platforms and sensing-oriented signal processing; CF-MIMO activities addressing distributed and scalable PHY-layer processing; and RIS-related activities investigating RIS architectures and RIS-assisted communication and sensing scenarios. Together, these contributions constitute the **WP3** data-plane building blocks of the 6G-SENSES infrastructure.

D3.2 finalizes and extends **D3.1**, which presented the initial **WP3** developments. The technologies described in this deliverable are aligned with the system architecture defined in **WP2** and provide the data-plane functionalities required to support higher-layer control and sensing services. Furthermore, the WP3 outcomes serve as inputs to the experimental validation activities conducted in **WP5** through Proof of Concepts (PoCs) and testbed evaluations.

This deliverable reports and advanced context of the 6G-SENSES data-plane infrastructure building blocks required to realize ISAC, CF-MIMO, and RIS technologies, that will be further integrated in **WP5** activities. This positioning provides a coherent transition from the architectural framework of **WP2** to the validation activities of **WP5** and introduces the technical chapters presented in the remainder of this document.

1.1 Organization of the document

This document comprises five chapters. Following the Executive Summary and Introduction sections:

Chapter 2 presents the activities concerning the development of ISAC strategies, implementation of these strategies onto the considered Wireless Access Technologies (WATs) that will be further used in WP5 and, finally, results stemming from small-scale ISAC testbeds that can be considered as outcomes of WP3 tasks.

Chapter 3 summarizes the CF-MIMO activities within the project, covering experimental CF-MIMO testbed investigations and simulation-based algorithmic studies on CF-MIMO unsourced random access (URA).

Chapter 4 presents the activities carried out in 6G-SENSES related to the design, optimization, and experimental evaluation of Reconfigurable Intelligent Surfaces (RISs) in various 6G use cases. In addition, it provides results that evaluate the influence of RISs on indoor wireless propagation, stemming from a set of controlled measurements carried out using a programmable RIS prototype.

Finally, Chapter 5 summarizes the document.

2. ISAC activities

ISAC activities in the 6G-SENSES project cover different topics that are interrelated with each other. Work has been in the design of suitable waveforms to perform communication and sensing, and in the design of technology platforms able to gather sensing data either in a radar-fashion or extracting the position of a user.

2.1 Update of the ISAC platforms

This section provides an update of the different WATs that can serve as ISAC platforms for assessing the developments carried out in 6G-SENSES and for running the PoCs in **WP5**.

From an architectural perspective, the way these sensing elements interact with the network is presented in deliverable **D2.3** [2], where the integration of non-3GPP sensing elements within the O-RAN architecture is described, so that they can be managed jointly with communication entities. This approach will allow both informed decision-making and comprehensive monitoring of the physical environment.

The implementation of the extension of the Near-Real-Time RAN Intelligent Controller (Near-RT RIC) to support sensing data exchange is common to most of the ISAC platforms described below, regardless of how it was originally obtained. The E2 interface, instantiated over Stream Control Transmission Protocol (SCTP), supports two key services, E2 Application Protocol (E2AP) and E2 Service Model (E2SM), enabling E2 nodes to publish data, while xApps in the Near-RT RIC subscribe to specific RAN functions. E2 communication is structured in terms of services, procedures and Information Elements (IEs), which define the data types and ranges exchanged between the Near-RT RIC and E2 nodes. The SM permits configuring the sensing resolution and information exchange.

2.1.1 Wi-Fi subsystem design

The Wi-Fi ISAC subsystem, designated as **LiveSense**, represents a significant advancement in transforming Commercial Off-The-Shelf (COTS) computing devices into high-precision sensing platforms. Designed as a cross-platform solution, it leverages standard Network Interface Cards (NICs)—specifically validated on **Intel AX211 (Wi-Fi 6E)** and **Intel BE201 (Wi-Fi 7)** modules—to enable centimetre-level Range-Doppler sensing. Uniquely, this subsystem operates in a monostatic active sensing configuration, utilizing one antenna for transmission and another for reception on the same device. This approach eliminates the need for external Software Defined Radios (SDRs) or complex bistatic infrastructure often required in prior sensing implementations, effectively unlocking radar-like capabilities on standard laptops.

Crucially, LiveSense preserves the device's simultaneous communication capabilities while extracting and processing Channel State Information (CSI) in real-time. The subsystem overcomes the inherent resolution challenges posed by the limited 160 MHz bandwidth of commercial Wi-Fi to deliver robust sensing outputs. By extracting fully synchronized CSI at frame rates exceeding 40 Hz, the platform supports a diverse set of applications, including the tracking of user distance and radial velocity, the detection of micro-motions such as respiration, and sub-decimetre ranging for hand gesture recognition.

2.1.1.1 Functional definition

The subsystem implements a full real-time sensing pipeline that processes CSI directly on the host device. The core functional blocks include:

- **Time-Phase Synchronization:** A three-stage alignment process comprising CSI cross-correlation for coarse timing, upsampled refinement for sub-sample delay correction, and per-frame phase unwrapping using the dominant Transmit-Receive (Tx-Rx) leakage as a calibration reference.

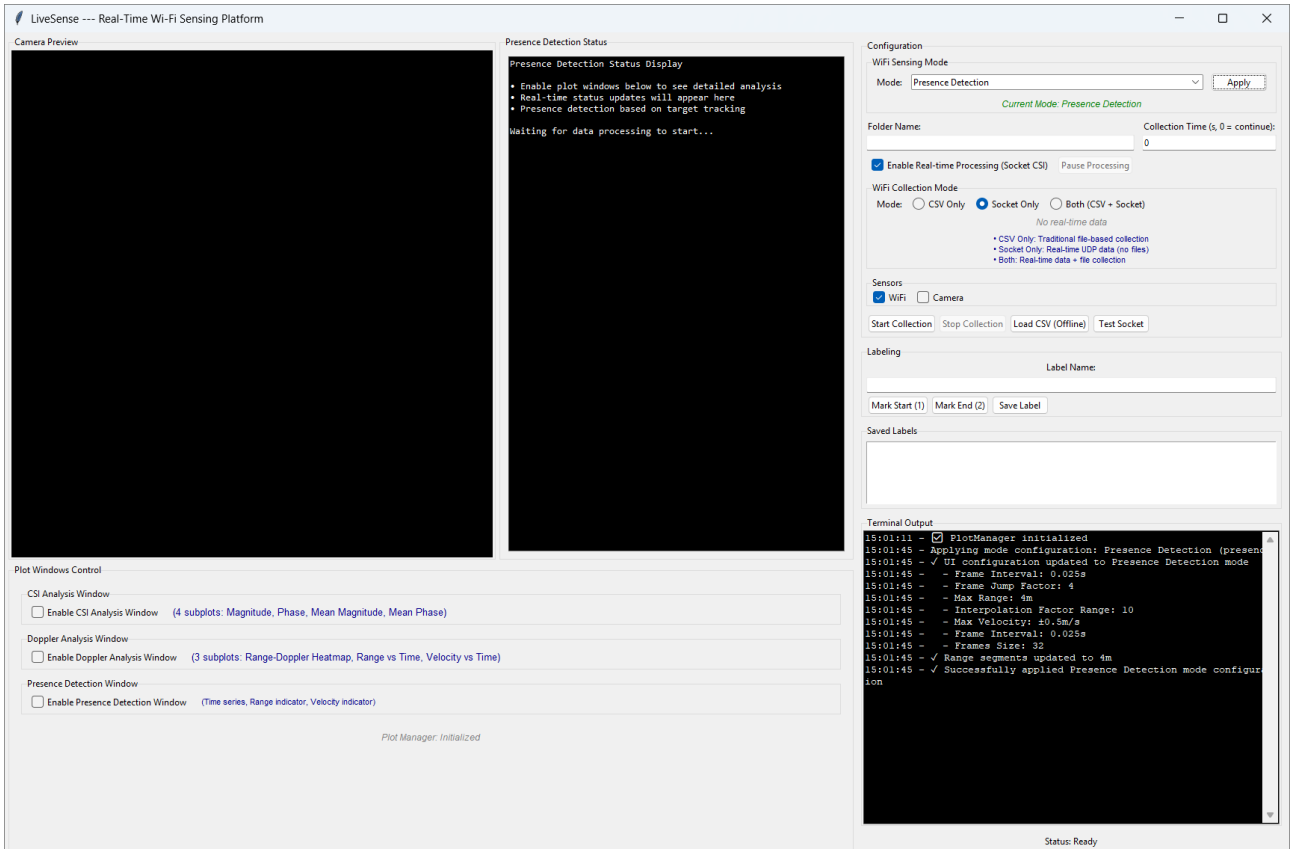

Figure 2-1 Wi-Fi LiveSensing platform

- **Self-Interference Cancellation:** On-device suppression of monostatic coupling and static clutter via per-bin Direct Current (DC) component subtraction over a sliding window.
- **Range-Doppler Processing:** Execution of Discrete Fourier Transforms (DFT) across subcarriers and Fast Fourier Transforms (FFT) over temporal windows to generate real-time Range-Doppler maps.
- **Operational Modes:** The system supports configurable modes optimized for specific use cases: *Gesture Mode* (prioritizing short-range accuracy via interpolation), *Presence Mode* (maximizing detection range), and *Efficiency Mode* (reducing computational load).

2.1.1.2 Hardware abstractions

The Wi-Fi subsystem implements a multi-layered abstraction stack that utilizes Python-based control to manage the commercial NICs.

Driver-Level Interface and CSI Collection The foundation of the abstraction layer is a specialized interface that communicates directly with the Wi-Fi driver via a dedicated Application Programming Interface (API). This API enables the software to control the underlying hardware parameters and request specific physical layer data that is typically discarded by standard network stacks.

- **CSI Extraction:** The system utilizes this API to capture and extract CSI specifically from the Long Training Fields (LTF) of received packets.
- **Synchronization:** The interface ensures the collection of fully synchronized CSI frames, exposing them to upper layers at sampling rates exceeding 40 Hz.
- **Non-Intrusive Operation:** The abstraction ensures that these sensing operations run in parallel with the standard network stack, preventing interference with simultaneous data communication.

Python-Based Software Core The sensing logic is abstracted into a flexible **Python** framework that runs on the host CPU (e.g., Intel Core i7). This high-level environment acts as the central controller for the hardware:

- **API-Driven Control:** The Python core uses the driver API to dynamically configure critical sensing parameters—such as bandwidth, frame rates, and detection thresholds—in real-time, without requiring firmware re-flashing.
- **Processing Pipeline:** The raw CSI data collected by the driver is ingested directly into the Python environment, where it undergoes time-phase synchronization, self-interference cancellation, and range-Doppler processing.
- **Visualization and Output:** The processed metrics are streamed to a Python/Qt-based Graphical User Interface (GUI), which visualizes the sensing outputs (e.g., heatmaps, velocity tracks) and provides an interactive layer for controlling the sensing modes (Gesture, Presence, or Efficiency).

2.1.2 Sub-6

Deliverable D3.1 [3] presented in section 3.2.2 the Sub-6 ISAC system. This solution is being reworked to allow building up an ISAC WAT that is based on a standard 5G Standalone (SA) implementation of OpenAirInterface (OAI).

2.1.2.1 Functional definition

This subsection focuses first on reporting about an add-on provided to the original ISAC platform, to then describe the current work in building up 5G ISAC solution using the same HW as per the original ISAC solution.

Background modeling

The sensing function of the ISAC system functions in a radar-like manner, exploiting the data communication waveform for sensing purposes. This means that all of the surrounding objects that reflect this waveform back are being detected, i.e. sensed by the ISAC system. While this is a desirable feature because it allows the entire environment to be sensed, not all objects within the environment are necessarily of interest. In many use cases, the stationary environment is not of interest. his stationary environment is usually referred to as clutter or background and is generally undesired. Therefore, it is usually removed to facilitate better detection of the objects of interest.

The developed sub-6 GHz ISAC system generates a heat map in polar coordinates, which shows the position of the object of interest. Nevertheless, the static clutter will also show background objects, which are not of interest, as well as artefacts which are created due to crosstalk between the transmitter and the receiver of the ISAC system. Both of them are masking the relatively low power reflections coming from the objects of interest, reducing the effective detection capability of the system. To remove the static background and artefacts due to crosstalk, they can be recorded and later removed from the sensing signal. The existing artefacts are embedded in the system and do not depend on the surrounding environment. They can be removed by performing reference measurements in an anechoic chamber, where no reflections are taking place. The measured artefacts can be later subtracted from the measurement signals. To reduce the effect of the noise on these measurements, usually more measurements are made and averaged. The static background is assumed to be static only over a limited period of time. This means that the ISAC system should perform background modelling before the sensing starts. This is performed by taking multiple sensing measurements and averaging them to reduce the effects of the noise present in the received signals. This procedure should be carried out when the background is not changing and no moving objects are present in the scene. In the developed sub-6 GHz system, reliable background modelling requires up to 10 seconds, making it challenging to apply in dynamic scenarios.

Since background modelling is challenging in dynamic environments and should be performed always when the background changes, a new approach was developed, which performs adaptive background modelling. This approach eliminates the need for a completely static scene during the background modelling procedure.

The heatmap generated during sensing of the environment is a matrix $S_{M\times N}$, where *M* represents the angles and *N* represents the distance. The values in the matrix represent the intensity of the reflection coming from angle *M* and distance *N*. In the non-adaptive background modelling case, the background is modelled as:

$$S_{BK} = \frac{1}{N}\sum_{i=1}^{N} S[i] \tag{2-1}$$

where *S[i]* is the i-th sensing measurement and N_{BK} is the number of sensing measurements taken to perform the background modelling. The obtained background model is later subtracted from every sensing measurement, to generate a heat map that contains only the new objects that entered the scene. This background model should be regenerated if the background changes or if the artefacts in the heatmap change due to, for example, a change in the temperature of the hardware.

To avoid a constant need of regenerating the background model, an adaptive approach was developed. Namely, the background model in this case is calculated as:

$$S_{BK}[n] = \alpha \cdot S_{BK}[n-1] + (1-\alpha)\cdot S[n] \tag{2-2}$$

where *S[n]* is the *n*-th sensing measurement, $S_{BK}[n-1]$ is the last estimated background model, α is the smoothing factor. This background model is again subtracted from every sensing measurement to obtain the heat map of the environment without background.

In Figure 2-2 a) the heatmap with implemented adaptive background modelling is shown. In Figure 2-2 b), the same heatmap is shown but without background modelling. It can be clearly noticed that the incorporation of adaptive background modelling improves the detection of the objects that enter the scene of interest.

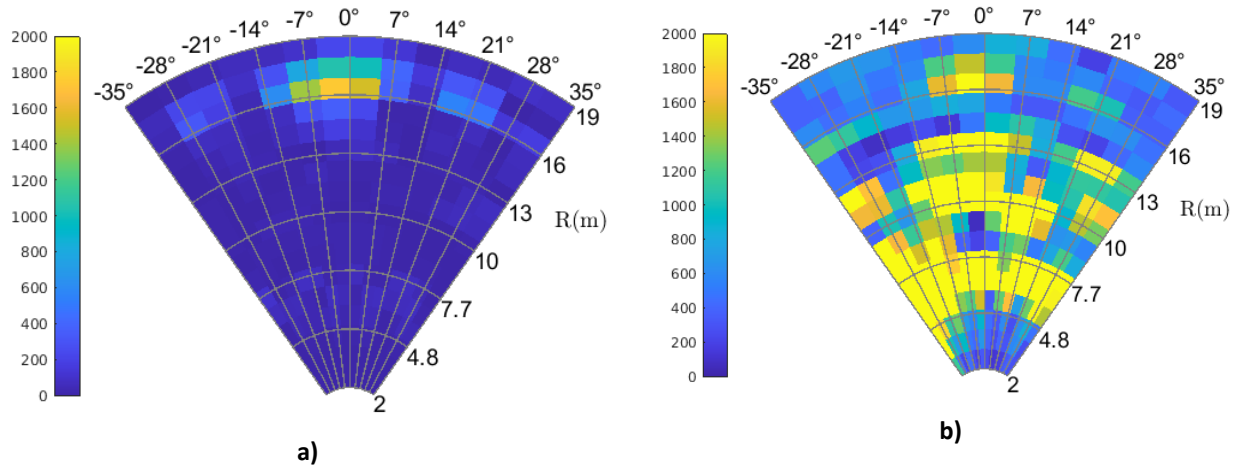

Figure 2-2 a) Sensing with dynamic background modelling, b) sensing without background modelling

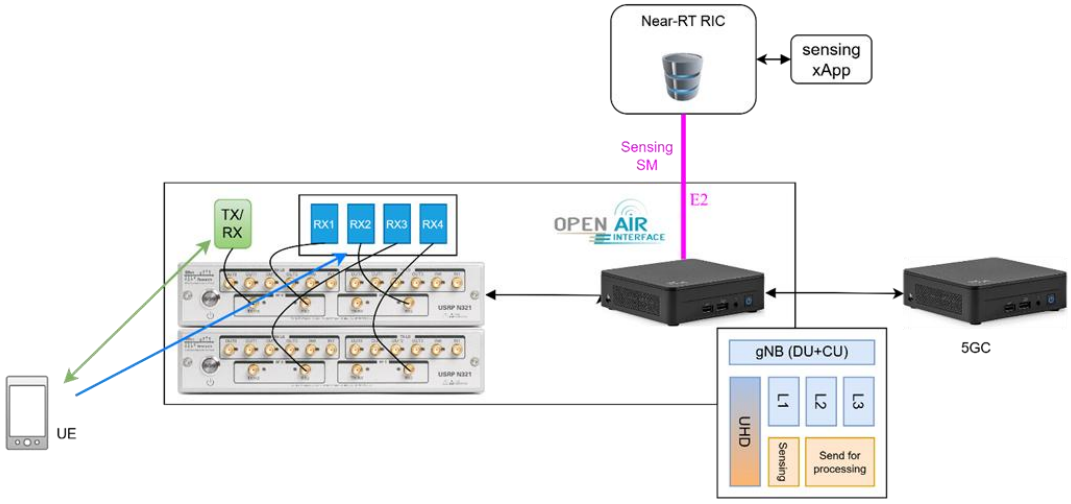

Figure 2-3 5G SA architecture with SDR-based sensing devices

5G support

The functionality of the sensing testbed proposed in D3.1 [3] is now being extended to support 5G communication and to feature radar capabilities. The setup depicted in Figure 2-3 represents the communication between a gNodeB (gNB) with a UE in a Time Division Duplex (TDD) fashion while, simultaneously, the gNB is able to receive the reflected signals simultaneously acting as a monostatic radar. The RU will have an OAI implementation of a gNB and an SDR platform (Ettus N321) to perform Over-The-Air (OTA) transmission/reception. The use of digital beamforming, as described in section 3.2.2.2 of D3.1, will be used to perform Angle-of-Arrival (AoA) estimation. This sensing system features 100 MHz bandwidth for sensing.

Moreover, the sensing Service Model (SM), proposed in deliverable D2.2 and being extended in deliverable D2.3 [2], is used to send the sensing data to the Near-RT RIC [5].

2.1.2.2 Hardware abstractions

The modification has made it possible to keep the antenna dedicated to TX/RX of the communications signal operating continuously in a TDD scheme (green antenna in the figure) while the rest of the antennas (in blue) operate in reception mode, receiving the reflected signals that are processed simultaneously to detect any changes in the surroundings around the sensing device.

The postprocessing of these I/Q samples can be either carried out at the sensing device or, alternatively, can be delegated to an xApp that will subscribe to the I/Q data available at the RIC. The available data at the sensing device is then exposed to the RAN via the E2 interface of the RIC (see section 2.3 of deliverable D2.3 [2] for more details).

2.1.3 mmWave

In deliverable D3.1 sec. 3.2.3 [3], a real-time mmWave ISAC system was presented, which is capable of bidirectional data transmission up to 5.8 Gbps, combined with monostatic Radio Detection and Ranging (RADAR) detection, which provides a range resolution of 6.7 cm and a maximum sensing rate of 2.1 kHz.

The system is built on an mmWave SDR platform operating in the 60 GHz band, extended with a real-time Orthogonal Frequency-Division Multiplexing (OFDM) baseband processor and additional components to support ISAC functionality. Key hardware elements include the AMD ZCU111 evaluation board with high-speed data converters, as well as dual phased array antenna modules for beam steering in the ±45° angular range.

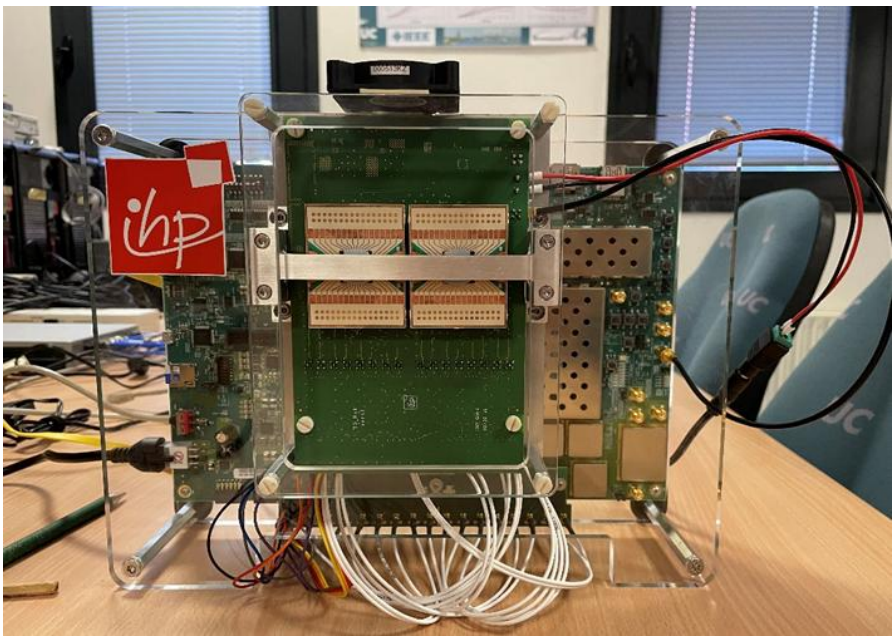

Figure 2-4 a) Xilinx RFSoC ZCU 111 board with SDR functionality and HW implemented real-time OFDM baseband processor, b) 60 GHz dual-module full-duplex RF frontend

2.1.3.1 Functional definition

In this implementation, the system operates at a sensing rate of 100 Hz, requiring a data transfer rate of 156.5 Mbps to collect the estimated Channel Coefficients (CHEs). The CHEs comprise 63 beams, covering different angular directions, and 1024 subcarriers, 828 of which are used for channel estimation. Following post-processing, a 1024-point inverse FFT (iFFT) is applied to the CHEs from all 63 beams, producing an environmental heatmap represented as a 63×128 (angle × range) matrix with double-precision resolution.

The system is able to define the start and stop beam indexes just to sweep in the azimuth plane a portion of all available 63 beams. It is supported only one consecutive range of beams.

2.1.3.2 Hardware abstractions

The added HW abstractions are related to the provision of E2 services, enabling E2 nodes to publish sensing data [5], which are described in **D2.3** [2] section 2.3.

2.1.4 5G NR

As illustrated in Figure 2-5, the O-RAN architecture introduces an open and programmable control framework for the 5G New Radio (NR) RAN through the separation of control functions into Near-RT RIC and Non-RT RIC domains.

2.1.4.1 Functional definition

The architecture is composed of a Near-RT RIC hosting xApps, and a Non-RT RIC hosting rApps. xApps operate in the near-real-time control loop, typically ranging from 10 ms to 1 s, and are responsible for time-sensitive RAN control (RC) and optimization functions. They interact with underlying E2 Nodes – e.g., gNB, gNB Centralized Unit (gNB-CU), gNB Distributed Unit (gNB-DU) – via the E2 interface using the E2AP. Through this interface, xApps can subscribe to measurements, receive telemetry data, and issue control actions. This requires xApps to understand the semantics of E2 SMs, including how to construct control messages and how to parse and analyze reports received from E2 Nodes in order to extract relevant RAN statistics and state information.

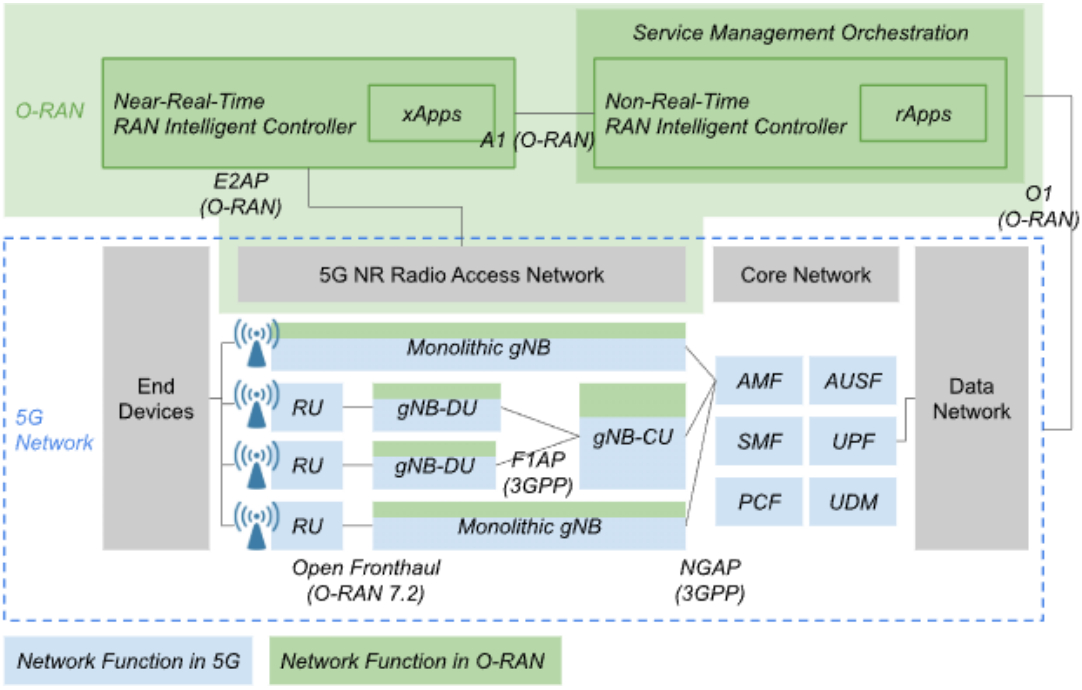

Figure 2-5 O-RAN integration into the 5G NR RAN

In contrast, rApps operate in the non-real-time domain (> 1 s) and focus on higher-level RAN optimization, orchestration, and policy management. rApps communicate with the Near-RT RIC via the A1 interface, through which they provide policies, guidance, and constraints, such as Service Level Agreement (SLA) objectives or energy saving rules, which influence near-real-time control decisions. Due to the relaxed latency requirements, rApps can leverage advanced techniques such as machine learning models, long-term data analytics, and agentic AI frame-works to enable intelligent and adaptive RC strategies.

By integrating O-RAN technologies into the 5G NR RAN, the architecture enables programmability and openness of RAN network functions, including the gNB, gNB-DU, and gNB-CU. These RAN functions incorporate O-RAN components such as the E2 Agent and E2 Termination, allowing the Near-RT RIC to interoperate with standard 5G protocol layers while maintaining compliance with 3GPP specifications.

2.1.4.2 Hardware abstractions - BubbleRAN MX-RIC Solution

BubbleRAN MX-RIC is a compact, efficient, and enterprise-grade O-RAN–compliant RIC platform designed to support both Near-Real-Time and Non-Real-Time RC. The platform natively supports multiple O-RAN standardized SMs, including Key Performance Measurement (KPM), RC, Cell Configuration Control (CCC), and Low Layer Control (LLC). A block diagram of the platform is shown in Figure 2-6.

In addition to standardized SMs, MX-RIC provides the flexibility to develop custom SMs to enable emerging RAN use cases, such as traffic control [6] and RAN slicing [7]. These custom SMs allow fine-grained programmability of RAN behavior while remaining compliant with the O-RAN architecture.

MX-RIC is highly programmable, modular, and extensible, and provides comprehensive Software Design Kits (SDKs) and APIs for rapid development and deployment of xApps and rApps. The platform supports C/C++ and Python-based development, enabling seamless integration of external analytics pipelines, optimization logic, and AI/ML models into the O-RAN control loop. MX-RIC enables ISAC with O-RAN LLC and RC SMs1.

[1] BubbleRAN MX-RIC: Enable ISAC with O-RAN LLC and RC SMs: https://www.youtube.com/watch?v=CGgvUCKy3M4

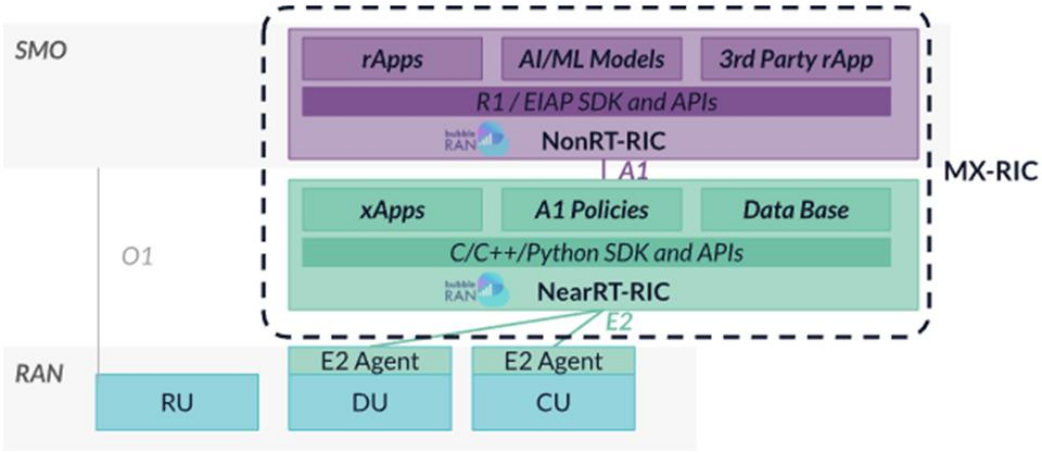

Figure 2-6 MX-RIC Block Diagram

Scenario 1: Real-Time I/Q Collection and Handover Control (Demo Video in Globecom2025)

This scenario demonstrates a closed-loop Near-RT RIC control workflow that combines real-time radio sensing with mobility control. The experimental setup consists of two gNB-DUs, one gNB-CU, and a COTS UE (Pixel 7). Each gNB-DU is deployed with a USRP B210 and operates in an OTA deployment.

Two monitoring xApps run on the Near-RT RIC and subscribe to two gNB-DUs via the LLC SM. These xApps collect Sounding Reference Signal (SRS) measurements, noise samples, and estimated channel frequency-domain information from both gNB-DUs in near real time, with an end-to-end (E2E) measurement latency of approximately 1 ms. The resulting I/Q samples are streamed to a Python-based real-time processing pipeline, which computes and visualizes key physical-layer metrics, including the Signal-to-Noise Ratio (SNR) and the peak of the Channel Impulse Response (CIR).

Based on these measurements, a simple threshold-based control policy is applied. When the observed SNR variation exceeds ±20 dB, a control xApp is triggered to issue a handover command via the RC SM. This command instructs the network to perform a F1 handover, migrating the UE connection from gNB-DU-1 to gNB-DU-2. This scenario demonstrates real-time sensing-assisted mobility control enabled by the Near-RT RIC and O-RAN SMs.

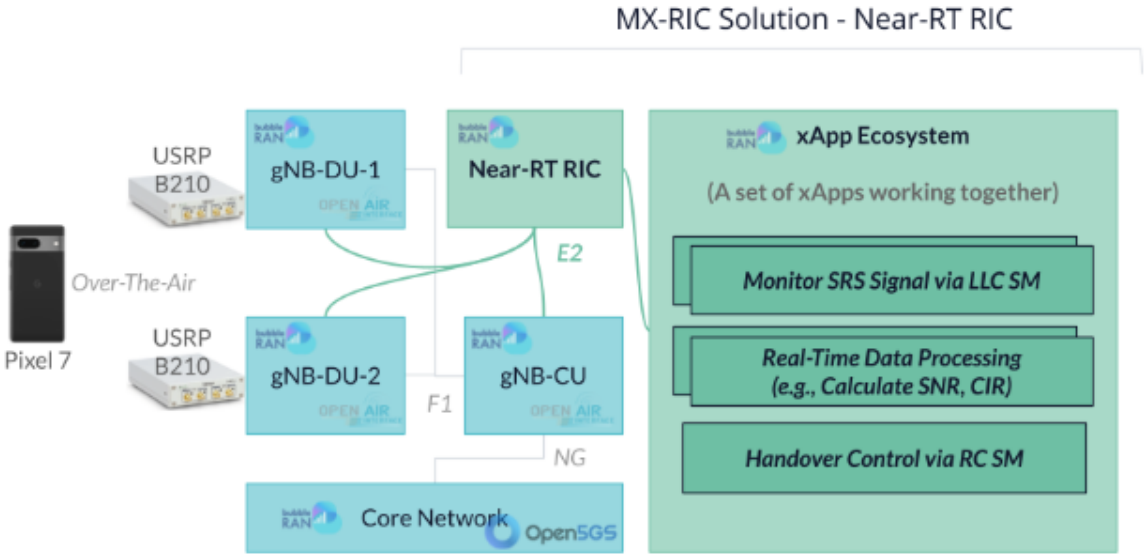

Figure 2-7 Block diagram of Scenario 1 implementation

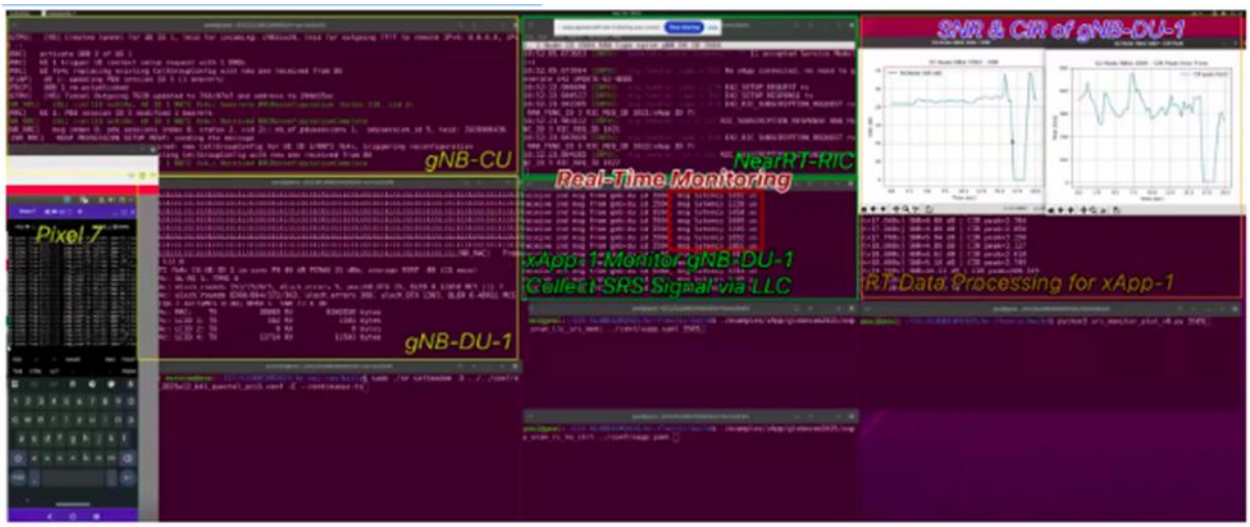

Figure 2-8 When UE is connected to gNB-DU-1

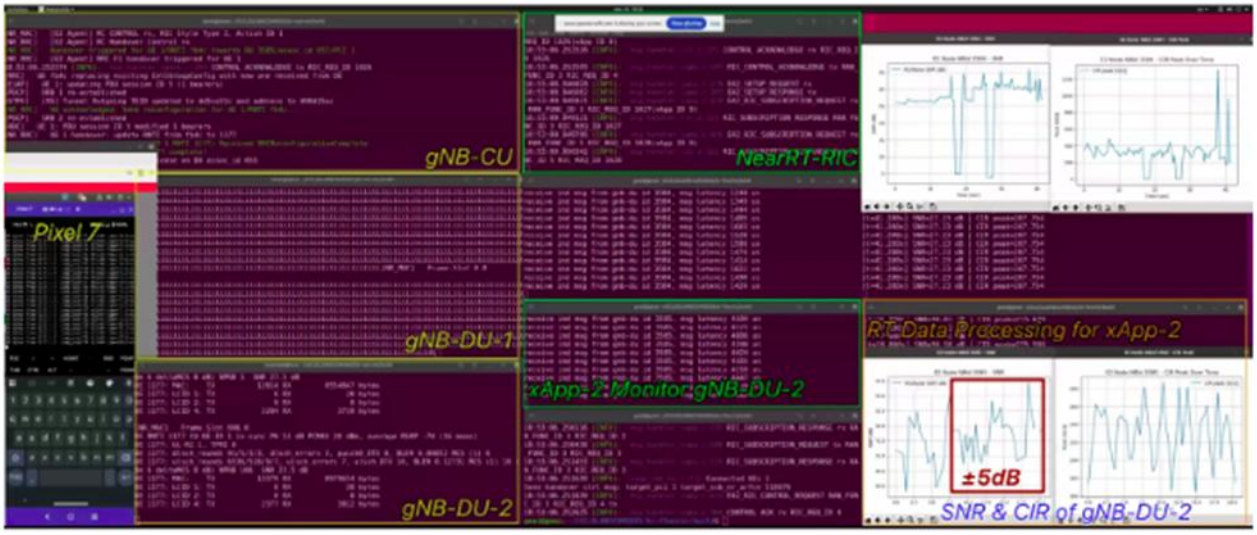

Figure 2-9 After handover to gNB-DU-2

Scenario 2: I/Q Collection with O-RAN 7.2 Deployment Under UE Mobility

In this scenario, I/Q samples are collected from a single gNB-DU deployed using the O-RAN 7.2 functional split, while the UE is physically moved to different locations at 50-second intervals (as depicted in Figure 2-10). The Near-RT RIC continuously gathers low-layer measurements via the LLC SM, enabling real-time observation of channel variations caused by UE mobility. This scenario highlights the capability of MX-RIC to support dynamic radio sensing and channel characterization under realistic mobility conditions. More details of this implementation will be included in **WP5** deliverables.

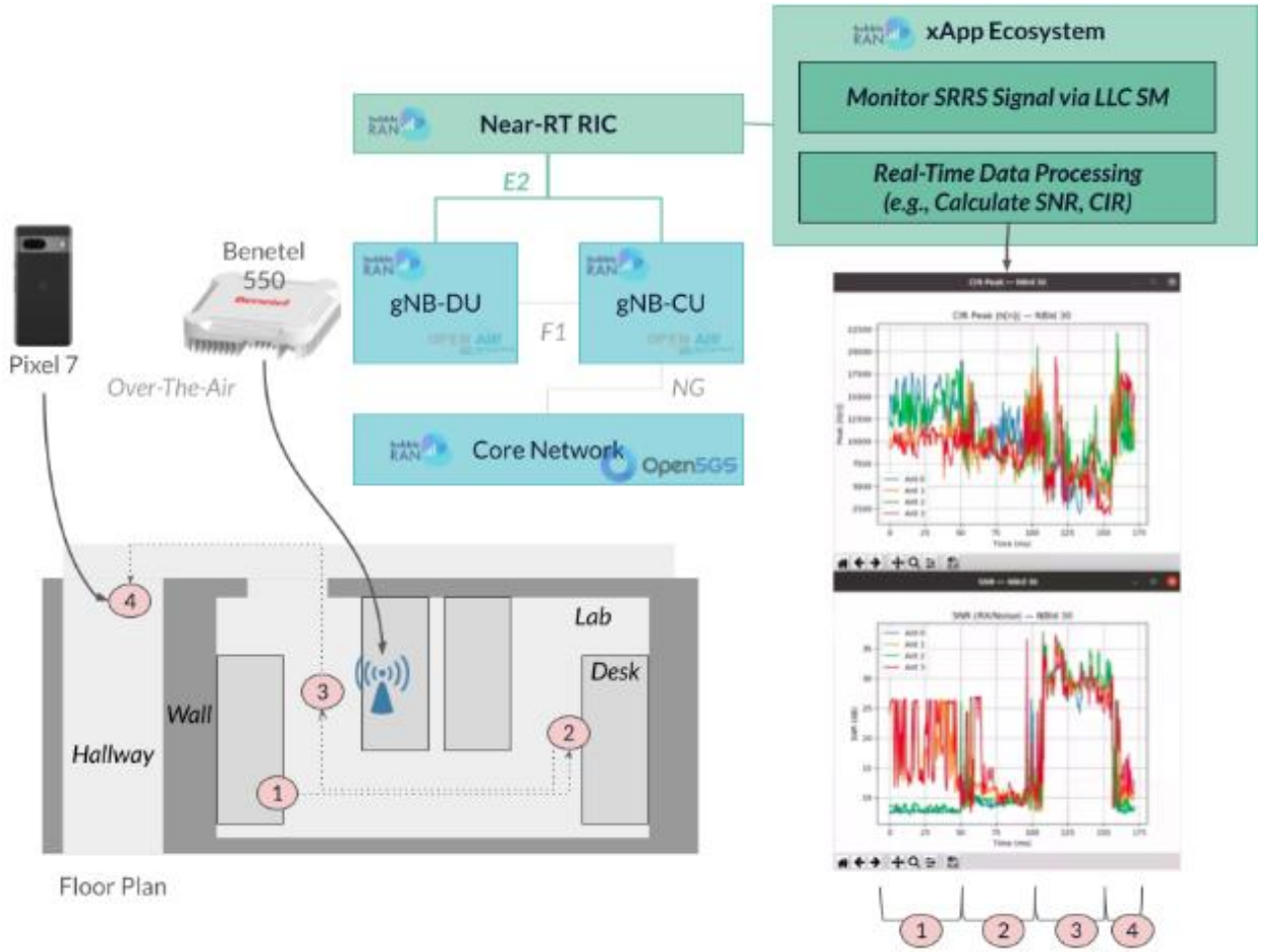

Figure 2-10 Block diagram of Scenario 2 implementation

2.2 Analog mmWave Front-End for ISAC

Aligned with objective 2.3 of 6G-SENSES, a mmWave front-end is projected for demonstration of indoor ISAC applications in mmWave regime. This new development has important features that makes it suitable for ISAC purposes, and will replace the front-end reported in **D3.1** (section 3.2.3) and section 2.1.3 of this document.

The wavelength at the 60 GHz band provides a practical balance between the chip and antenna dimensions, i.e. justifiable chip area and still manageable by Printed Circuit Board (PCB)-based implementation for the packaging and antenna implementation. Yet, the wavelength inside the medium, i.e. guided wavelength, needs careful design attention and so are the packaging interconnects between the chip and PCB, which demonstrate high parasitic effects with increasing frequency [8].

Although commercially available chipsets and front-end modules are available for 60 GHz, they are optimized and marketed mainly for communication throughput and do not exhibit the full sensing potential, envisioned for ISAC platforms. Hence, repurposing the available COTS items leads to suboptimal sensing performance. In contrast, the envisioned mmWave front-end in 6G-SENSES targets the optimized ISAC performance with ultra-low power and low DC supply voltage, making it suitable for battery operated devices and distributed deployments. The envisioned front-end module design is modular and scalable, e.g., allowing the number of MIMO chains to be adapted according to the application without changing the individual chain structure. This modularity, together with low power and intrinsic advantages of 60 GHz band, support a flexible wireless system implementation through a shared hardware for sensing and communication.

In 6G-SENSES, the module is structured into two main components based on the underlying technology: the front-end chipset being developed by **IHP** through its Silicon Germanium (SiGe) technology, and the antenna-in-package module being designed on printed circuit technology by **BI**. The results of each module for M13 to M24 are summarized as follows.

2.2.1 Analog front-end chipset

The 130-nm SiGe-based front-end transceiver design at 60 GHz and a Local Oscillator (LO) signal generation unit design at 30 GHz and their respective sub-components have been fabricated. An on-wafer measurement campaign has been conducted to verify the functionality and derive performance metrics.

The 30-GHz Driver Amplifier (DA) and 60-GHz Power Amplifier (PA) of the existing low-power transceiver Integrated Circuit (IC) [9] consume most of the dc power budget. Therefore, the designs have been updated and the fabricated test blocks have been characterized on-wafer, micrographs shown in Figure 2-11, with good agreement to the simulated results, small-signal gains of about 12.5 dB and 18 dB at 30 GHz and 60 GHz, respectively.

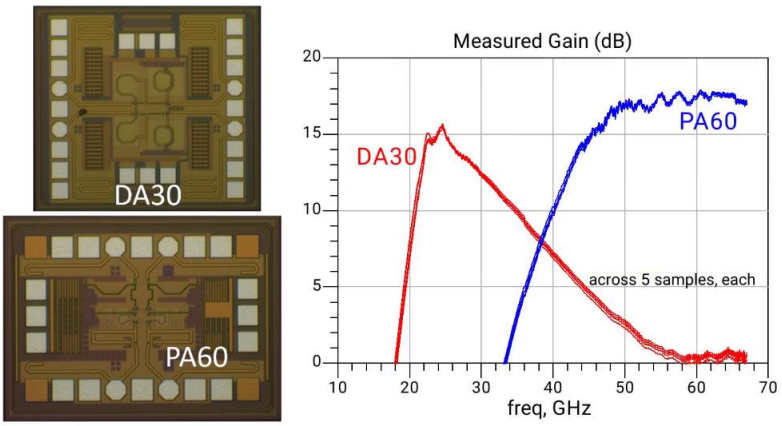

Figure 2-11 Micrographs of the fabricated 30-GHz DA and 60-GHz PA blocks

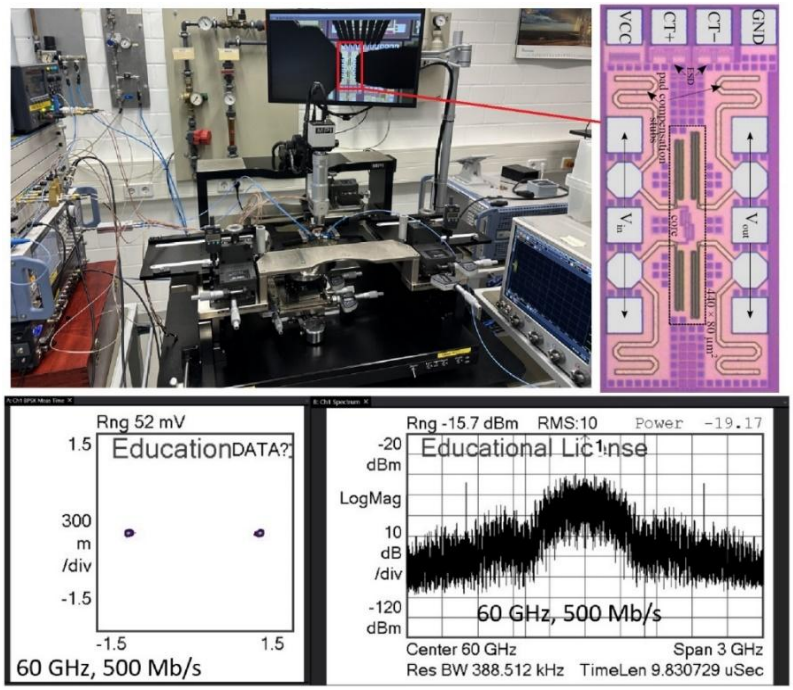

Figure 2-12 Measurement setup with the BPSK modulator probed and the key measured results at 60 GHz with 500 Mb/s

An additional modulated signal measurement campaign on the BPSK has been performed. The measured constellation diagrams and linearity look quite promising, and the losses of about 3.5 dB agree with earlier measurements. The performance at 60 GHz along with the chip micrograph are shown in Figure 2-12.

The new transceiver chip that integrates these amplifiers and modulators (BPSK modulator in the receiver and vector modulator in the transmitter part) have been fabricated in the same technology SG13G2, our advanced in-house 130-nm SiGe BiCMOS process, and characterized in both small-signal and large-signal domains with the help of a carrier board where the IC is mounted and partially bonded, except the high-frequency ports, which are to be contacted by RF probes. The chip micrograph on the carrier board and key measurement results are plotted in Figure 2-13 below.

The dc power consumption of about 85 mW is consistent across several carrier boards that are measured. The Tx and LO input-output power levels are measured across frequency. The Tx output power is above 10 dBm in the targeted band, as expected. The experiments have been repeated for the four quadrants of the vector modulator at the highest gain setting, showing good amplitude balance across the states. In addition, roughly 20 dB of analogue gain control is enabled with this vector modulator. The gain of the LO chain (input to output, for daisy-chaining and scaling the number of channels) is at least 3 dB in a wide band from 25 GHz to 40 GHz, allowing at least 1.5 dB of integration losses on both sides. Furthermore, a very high Tx-Rx isolation of more than 60 dB has been measured, which is quite promising for the front-end. Also, the measured rejection levels in sub-harmonic (Tx) and harmonic (LO) outputs are above 45 dB.

On the signal generation side, the sub-blocks of the highly-efficient 30-GHz signal source have been fabricated and characterized on-wafer as well. These include the Voltage Controlled Oscillator (VCO) and the frequency divider chips, as well as the combined version of the two for additional verification.

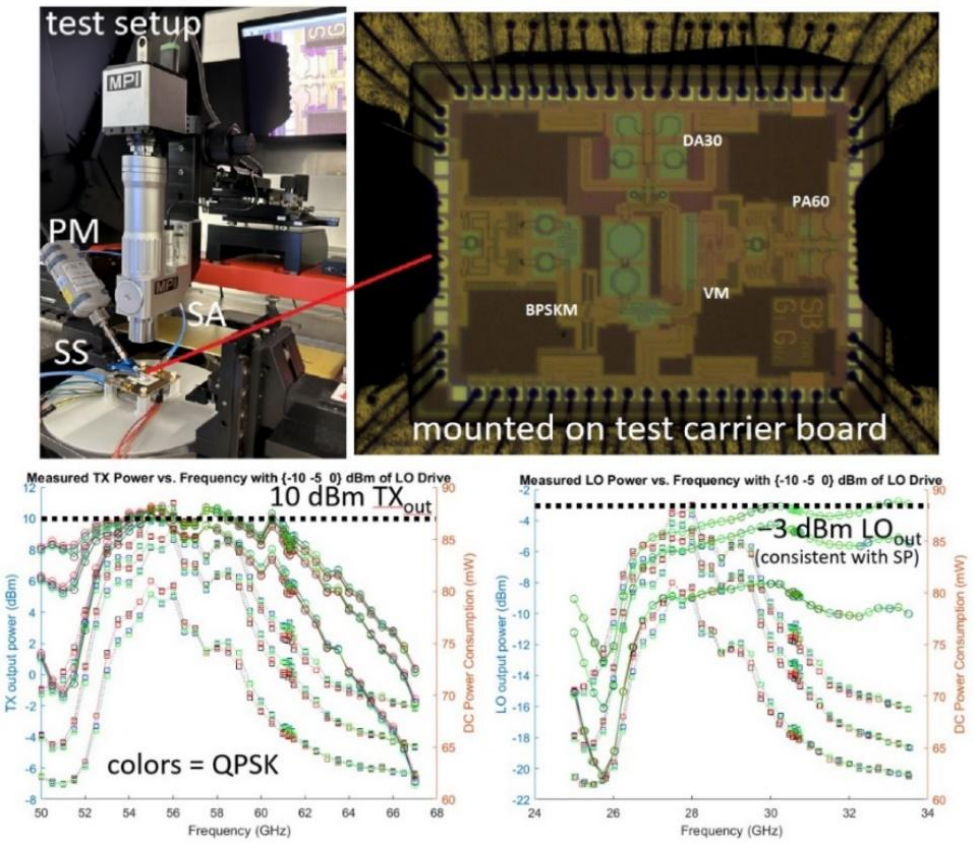

Figure 2-13 Measurement setup, TRx IC mounted on a carrier board for small- and large-signal tests, and the key measured results

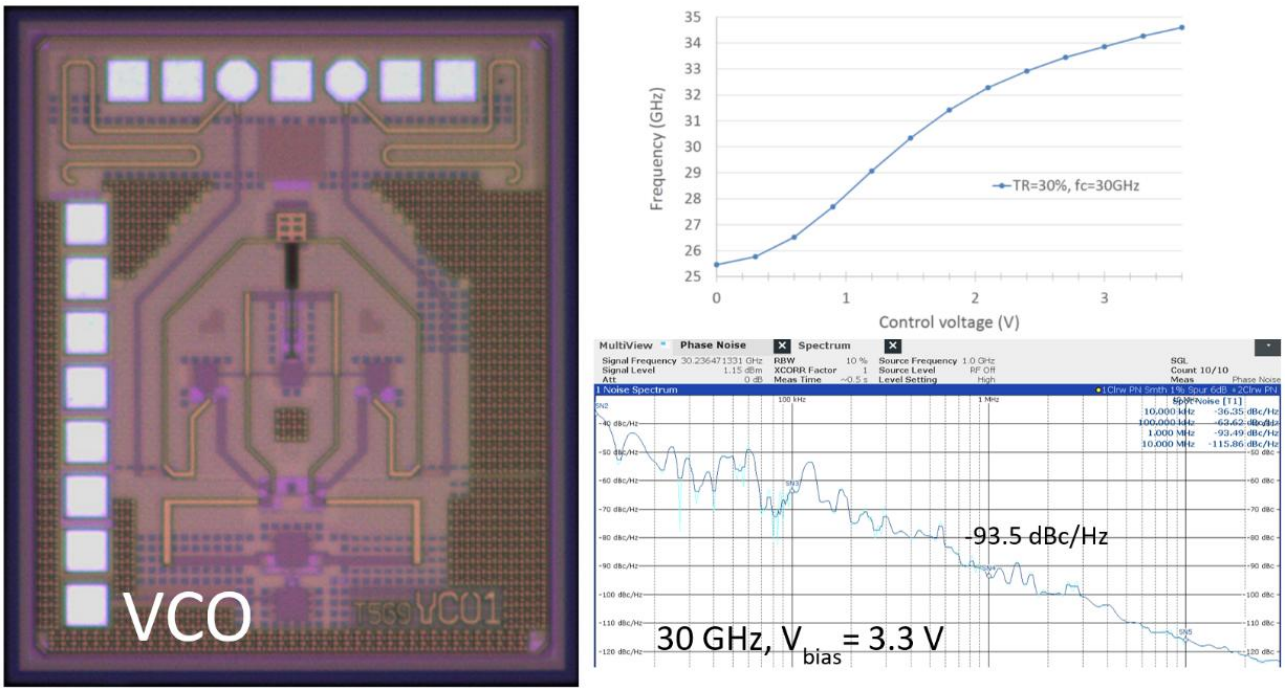

Figure 2-14 Micrograph of the VCO and the measured tuning range and phase noise

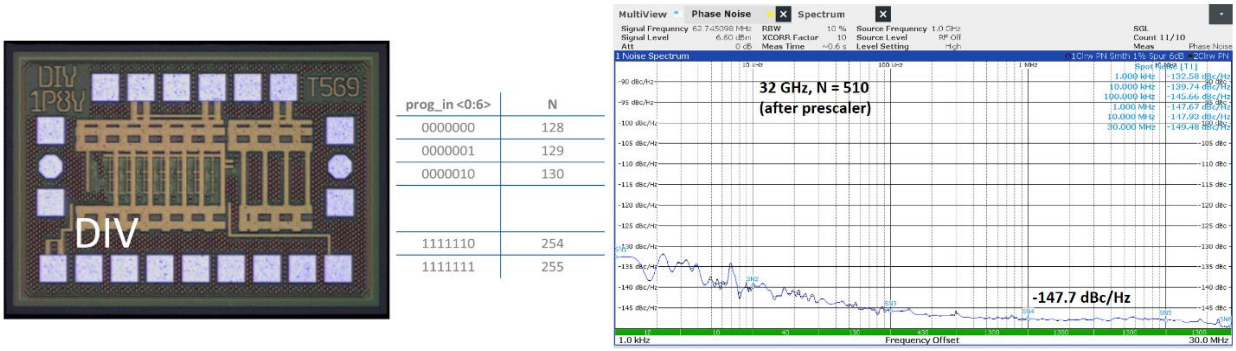

Figure 2-15 Micrograph of the programmable divider and its measured phase noise when combined with the VCO

The VCO chip, whose micrograph is shown in Figure 2-14, exhibits a measured wide tuning range above 30% around the center frequency of 30 GHz. It consumes a total of 21 mA from a supply voltage of 3.3 V. The measured phase noise at 30 GHz is shown in Figure 2-14 as well. At an offset frequency of 1 MHz, it is around −93.5 dBc/Hz, which is quite good considering the wide tuning range.

On the other hand, the programmable divider chip (division ratio: 128–255) and the combination with the VCO and the prescaler circuitry (division ratio: 256–510) work as expected as well, with a supply voltage of 1.8 V. At the highest division ratio, the measured phase noise at 1 MHz frequency offset is about −147.7 dBc/Hz, as shown in Figure 2-15. Considering the division ratio and the theoretical change in the phase noise level, i.e. 6×log2(510)≈54 dB, the measured results agree well with those of the VCO, reported above.

2.2.2 Antenna-in-package

The pad structure adopted by **IHP** for the intended 60 GHz transceiver chipset is furnished by open circuited stubs for 60 GHz RF Tx and Rx interfaces and 30 GHz LO interfaces in a differential configuration. This open circuited stub helps compensate for the pad parasitic during a wafer-prober based measurement setups. The length of the stub is set to get a high return loss at the frequency of operation. The pad structure and the simulated response are given in Figure 2-16.

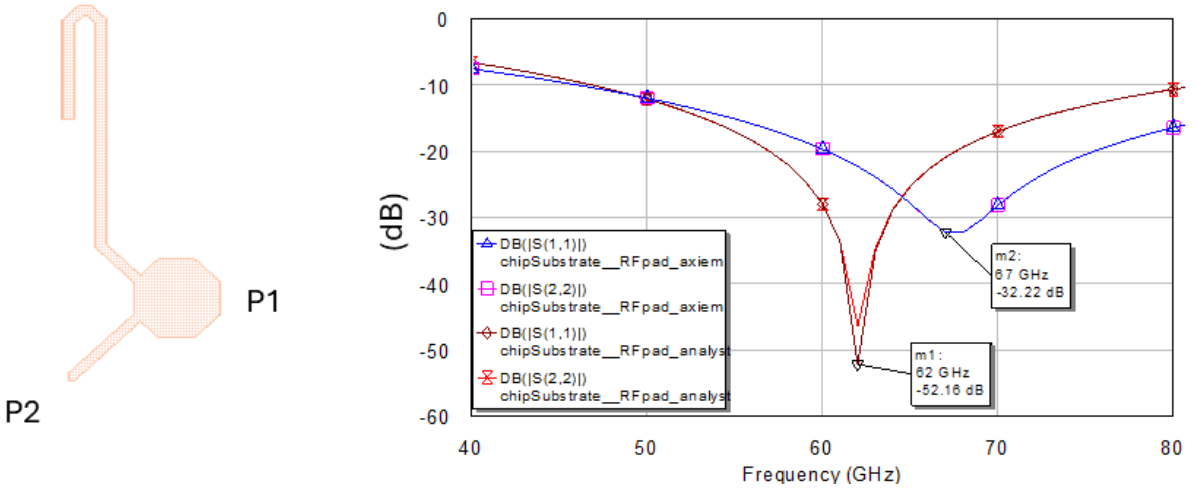

a) b)

Figure 2-16 a) 60 GHz transceiver chip pad structure, b) simulated response with two different EM solvers (AWR Axiem and AWR Analyst)

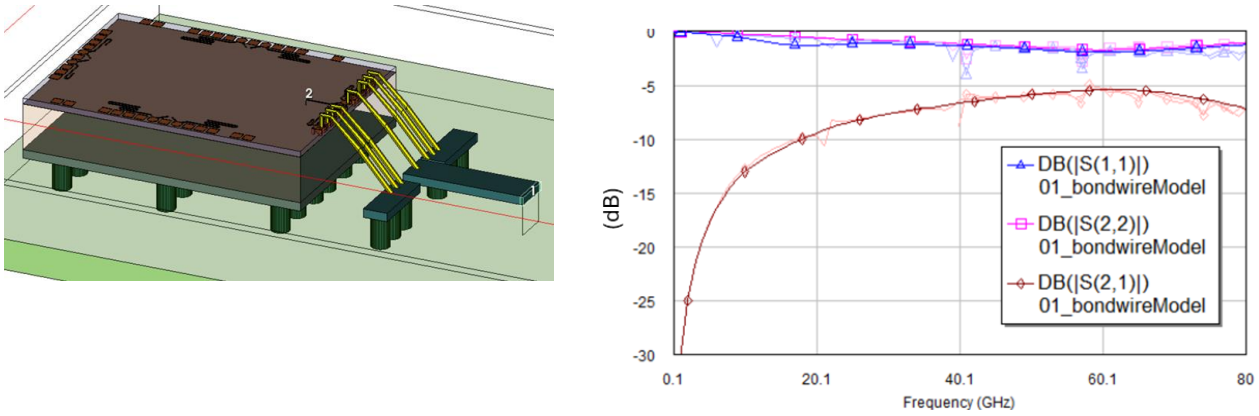

a) b)

Figure 2-17 3D simulation setup for the under development 60 GHz transceiver. Chipset mounted on a PCB with uncompensated chip-to-PCB bondwire interconnect and its simulation response

As a preliminary step, the response of an uncompensated bondwire is estimated by designing the chip-to-PCB interface on a 3D EM solver (Cadence AWR Analyst), shown in Figure 2-16. Port 1 is a microstrip port on the PCB on which the chip is mounted while Port 2 is a microstrip port on the chip. **IHP** SiGe stack up is considered for the chip while 127 µm high Rogers 3003 substrate with a dielectric constant of 3.00 and loss tangent of 0.001 is considered for the PCB. Chip grounding to GSG pads is provided through grounded bondwire pads on the PCB and several grounding bondwires to minimize the inductance at the current return path. The response shows that the bondwire interface is not usable without a compensation or matching network. Furthermore, the response of this bondwire interface deviates from a typical response, i.e. the high return loss at the lower frequencies continuously degrading with the increasing operating frequency [10], since the pad itself is not feasible for lower frequencies due to the open circuited stub.

Since a bondwire has a dominant parasitic inductance, creating a low pass effect, a compensation network is designed and simulated through an inductor-capacitor-inductor (LCL) approach [11]. Considering bondwire parasitic inductance as the first component in LCL network, a PCB pad with calculated dimensions serves as a capacitor against the ground plane, and the last inductor component is achieved through an auxiliary bondwire with a calculated length for a specific inductance. This way, one inductor and the capacitor of the

LCL network can be tuned to achieve passband at the frequency of operation. A novelty in this approach is implemented by replacing the auxiliary bondwire, which is a source of uncertainty due to its manufacturing tolerances and human error, a defected ground structure (DGS) is introduced. The DGS disturbs the returning current path under the desired microstrip on the PCB, increasing its inductance. This way, for the same DC resistance, a higher inductance from the PCB trace is achieved which, otherwise, requires a thinner trace, restricted by the PCB manufacturing resolutions. The downside is that multilayer PCB stack up complicates or affects the DGS performance. The 3D and simulation results are shown in Figure 2-18.

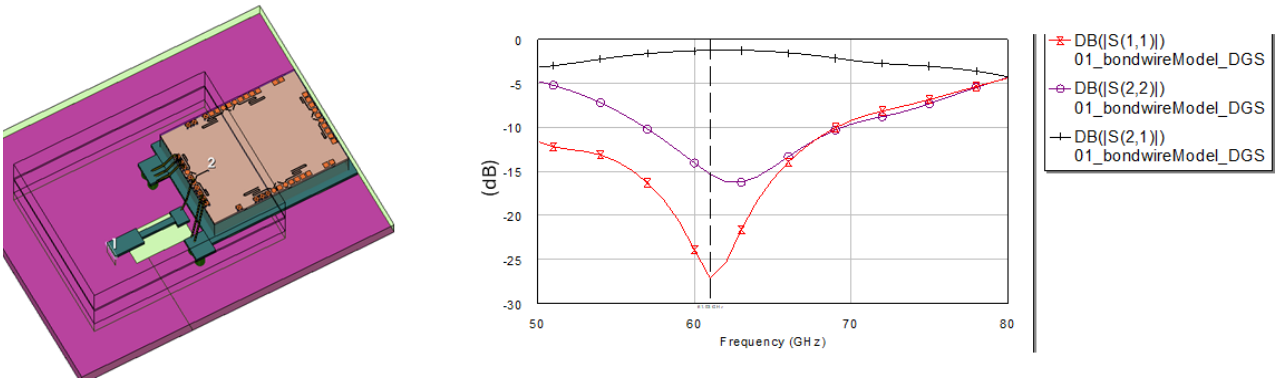

Figure 2-18 Simulation setup for the developed bondwire-inductance compensation with an auxiliary bondwire and PCB pad and its simulation response.

The approach shows 20 % fractional bandwidth at 60 GHz center frequency with 10 dB return loss, which fully covers our intended bandwidth 61- 61.5 GHz with significant margins.

To mitigate the root cause, parasitic inductance, of the bondwire, the length of the bondwire should be decreased, pushing the landing pad on the PCB closer to the chip. However, the approach is capped by the tool size of the bonding machine to operate without touching and damaging the chip. As an alternative, we have considered mounting the chip in a cavity on the PCB. This reduces the bond profile height and hence the total length without risking the lateral distances between the PCB pad and the chip. For such configurations specialized PCB stack-up is considered, shown in Figure 2-19, based on RO3003 as a primary substrate for RF routing and additional bottom copper layers for low frequency and digital signal routing.

In Figure 2-19, chip cavity 1 show 127 µm deep cavity, existing only in the top most dielectric. This type of configuration is easy to make, economical and offered by several PCB manufacturers. However, the optimal case is complete embedding the chip into the substrate and achieving a flush chip-PCB surface. For this, a deeper cavity down to the second dielectric level is required because the chip height is 200 µm. Considering the proposed PCB stacking with flush chip-PCB surface, both types of bondwire matching techniques are evaluated, i.e. with auxiliary bondwire and with DGS, as shown in Figure 2-20.

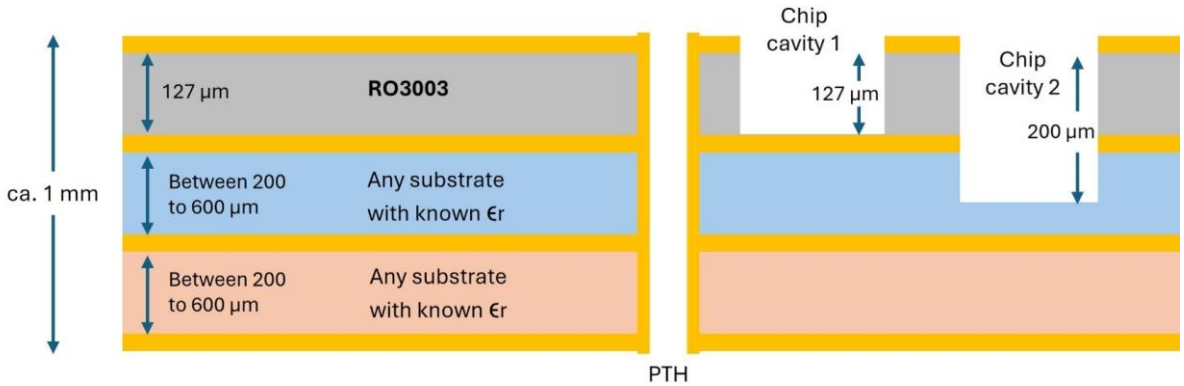

Figure 2-19 Proposed PCB stack-up for 60 GHz front-end module

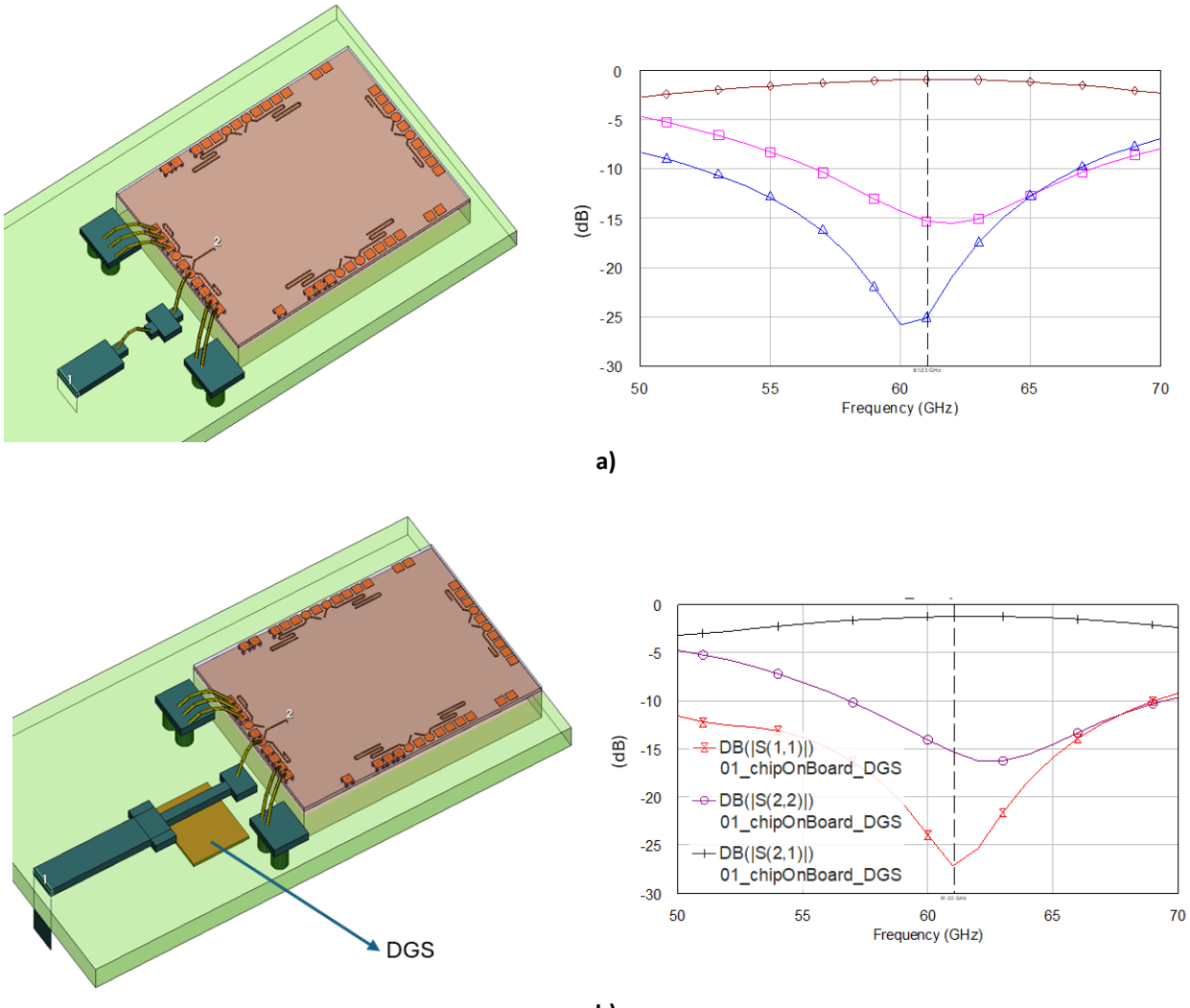

Figure 2-20 Bondwire parasitic compensation networks through LCL approach: (a) with auxiliary bondwire and (b) with DGS structure.

Both structures are single-ended and provide almost similar performance, i.e., >15 GHz of 10 dB matched input return loss on PCB as well as on chip side and insertion loss <2 dB. However, on the trade-off of tolerance uncertainty (with auxiliary bondwire) vs multilayer stacking complications (with DGS).

Currently, the chip-to-antenna interface with differential interface is under investigation and both approaches are under consideration. Since the actual transceiver interface is differential, the decision on the topology is dependent on the performance of the topologies in differential configuration. Further tasks in this module are development of differential packaging prototypes with the selected approaches and benchmarking in the laboratory.

In addition to packaging, antenna arrays are under design. For that purpose, three single element radiators have been designed and reported including patch radiator with inset feed, apertured coupled radiator with gain boosting metamaterial lens and dual port patch for full duplex operation (see Figure 2-21). A modular approach is planned by designing 1x4 array on a sperate PCB then the front-end module, connectable through an array of 1.85 mm precision coaxial connectors. The modular approach provides future application-specific antenna selection option for the same front-end.



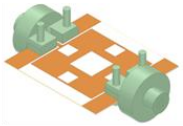
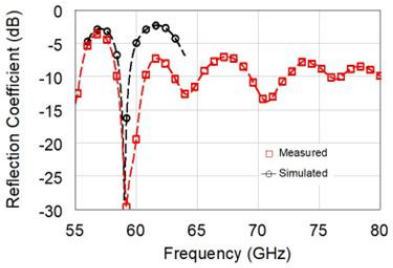

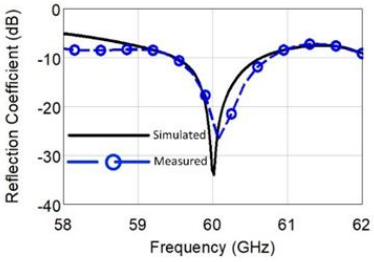

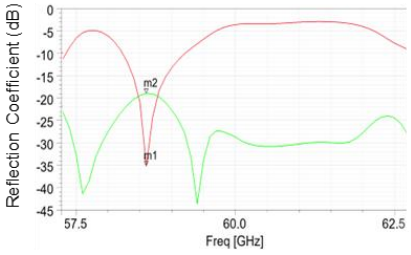

a) b) c)

Figure 2-21 Developed mmWave antenna elements. (a) inset feed, (b) aperture coupled metamaterial gain boosting lens and (c) dual port for simultaneous transmit receiver operation

2.2.3 Benchmarking of 6G-SENSES ISAC chip

This section intends to compare the V-Band chip that has been designed and fabricated in the context of 6G-SENSES with other solutions that are available in the literature (see for Table 2-1 details).

Table 2-1 Benchmark of the 6G-SENSES V-Band ISAC chip

Parameter (units)	[12] TMTT26'	[13] TMTT25'	[14] JSSC24'	[15] JSSC17'	[16] IFX 25'	6G-SENSES
Process	65-nm CMOS	65-nm CMOS	40-nm CMOS	130-nm SiGe BiCMOS	Infineon SiGe BiCMOS	130-nm SiGe BiCMOS
Integration	TRx + PLL	TRx	TRx + PLL	TRx	TRx+PLL	TRx[12]
ISAC	No	Yes	No	No	No	Yes
#TX/#RX	3/4	1/1	2/2	1/1	1/1	1/1
Bandwidth (BW) (GHz)	56–66	55–65	54–69	50–67	57–63	55–64
RX Conversion Gain (CG) (dB)	18–82	20–75	20–87	24	12–16	27
RX Noise Figure (NF) (dB)	7.8–10.7	5.8	9.4–10.5	9.8[sim.]	12–14	3.8[sim]
TX Saturated Output Power (P_{sat}) (dBm)	11.3–14.3	16	12.8	11.5	5	10.5
Supply Voltage (VDD) (V)	1.0/1.8	N/A	1.1	3.3	1.2/1.8/3.3	1.5
DC power level (Pdc) (mW)	674	500	695	594	574	85
Pdc/TX (mW)	N/A	N/A	78	181	N/A	50
Pdc/RX (mW)	N/A	N/A	115	226	N/A	16
Chip Area (mm^2)	13.44	3.15	9.9	3.72	16.4	4.32

[2] PLL not integrated. The fully-integrated PLL chip developed in-house consumes ≈200 mW in simulations.

In **WP5** deliverables, the ISAC solutions developed in the context of the project can be also benchmarked against those available in the literature and those developed in peer SNS JU projects.

2.3 6G-SENSES ISAC Experimental Evaluation

2.3.1 6G-SENSES PoC Target implementation

As presented in deliverable **D5.1** [17], 6G-SENSES is planning to provide a multi-WAT solution that offers sensing capabilities. While communicating with the UEs, the radar-based sensing technologies can sense the environment and provide sensing data with different granularities to the RIC. The *comm+sensing* technologies maintains the communication while inferring the position of the UEs. This way, the xApps behind the RIC can exploit *comm+sensing* merged data to anticipate communication impairments, and react optimizing the usage of radio resources.

Figure 2-22 presents a diagram where the ISAC building blocks referred to in this deliverable are depicted in the left-most part of the figure.

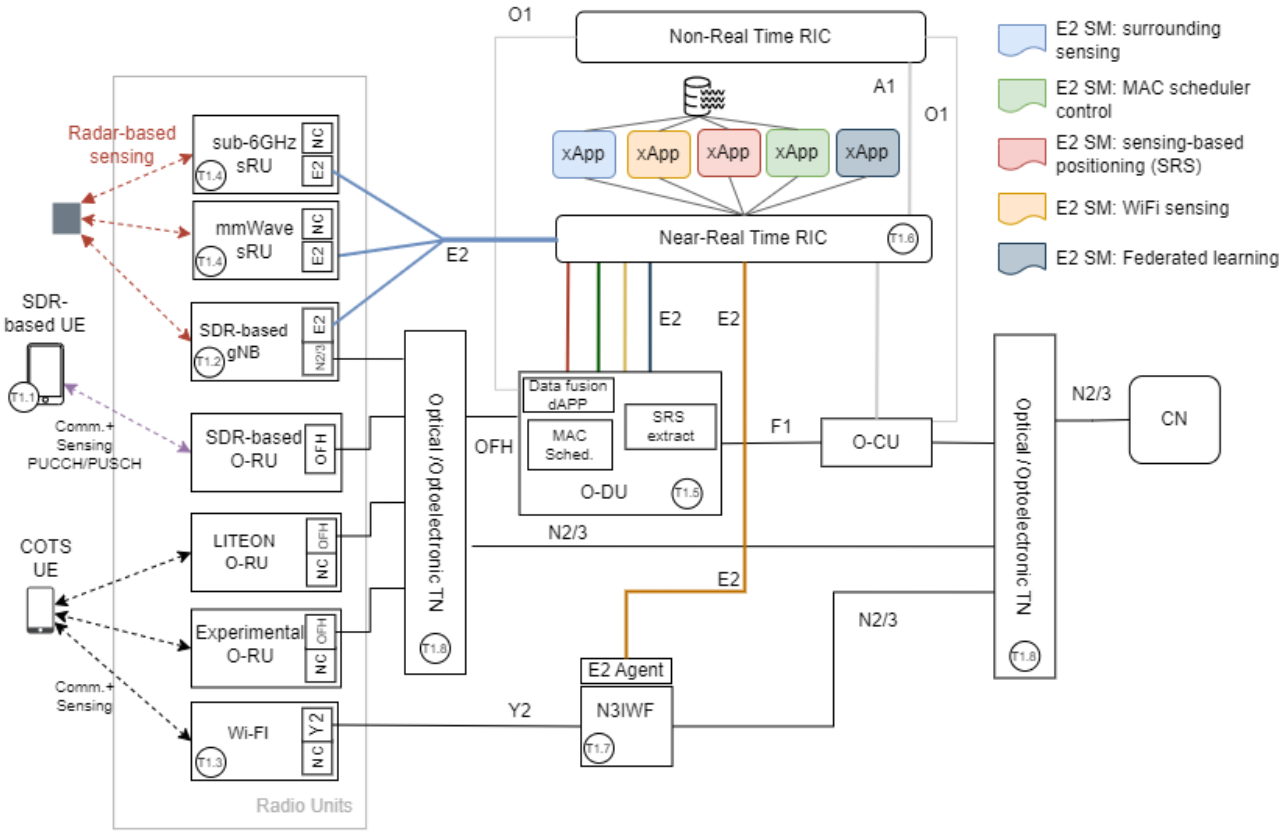

Figure 2-22 Implementation of the 6G-SENSES architecture for PoC#1

In addition to the Sub-6, mmWave and Wi-Fi ISAC solutions (reported in this deliverable and in **D3.1**), other experimental solutions such as an Orthogonal Time Frequency Space (OTFS)-ISAC implementation and the use of SDR-based O-RUs will be considered for showcasing during the last 6 months of the project. They potentially will not be integrated in a single platform but may be showcased as small-scale ISAC testbeds. The development of one of these examples (OTFS-ISAC) is presented below.

2.3.2 6G-SENSES OTFS-ISAC implementation

The OTFS implementation included in **D3.1** [3] is here being extended towards the completion of an OTFS-based ISAC platform that, potentially, could be integrated as another WAT as part of Figure 2-23.

As compared to theoretical work, practical experimentation is scarcer in OTFS. SDR-based first OTFS system was found in [18], in which hardware impairments were studied and comparison with OFDM waveform was done. An evaluation of the OTFS waveform on a 60 GHz testbed was carried out in [19] with a focus on the influence of RF impairments. Few synchronization challenges and results were illustrated in [20], while the impact of a Sampling Time Offset (STO) in hardware was analyzed and solutions were proposed in [21]. For ISAC scenarios, OTFS has also been considered for practical research [22] [23].

Here we accomplish a single-rate-based OTFS system on Universal Software Radio Peripheral (USRP) X310 SDR [24]. The system represents the downlink node part of an ISAC-based network, in which ISAC capability is performed at the base station, and our system acts as a downlink node, with which the base station is communicating. We performed experiments in a realistic office environment at a 5 GHz carrier frequency band and utilized a large bandwidth to match the increasing demand for future systems.

2.3.2.1 OTFS (communication) implementation on SDR

For practical implementation, synchronization is one of the most critical factors. On USRPs common challenges include Carrier Frequency Offset (CFO), STO and DC offset. Due to its natural resilience to Doppler, CFO does not need to be corrected, and it adds up with channel response on the Doppler axis [18]. STO causes additional peaks on the Delay axis and significantly increases the equalizer complexity. STO adds up as a part of the channel in the TF plane. However, for low-complexity Zak-OTFS systems, where the TF plane is not utilized, STO correction alleviates the equalizer task [21]. DC offset appears on the zero Doppler column. Simple subtraction of measured offset and uncomplicated IIR/FIR filtering are a few techniques to mitigate this effect.

For frame start, an m-sequence is utilized to perform cross-correlation at the receiver. The same cross-correlation result can also provide STO correction at low complexity [21]. To allow support for multiple waveforms in the future, an additional preamble for CFO correction is added. A symbol for TF-equalization is also added to support low-mobility scenarios. This symbol for TF-equalization is a single Physical Downlink Shared Channel (PDSCH) Demodulation Reference Signal (DMRS) of 5G [25], and it is generated with the help of the 5G Toolbox in MATLAB. Finally, the OTFS frame is added at the end, and the waveform is transmitted.

Our targeted environment is an office scenario, and our implementation of OTFS modulation for such an indoor environment is demonstrated in Figure 2-23. Multipath components can be easily compensated by TF equalization in indoor environments. Both MMSE and ZF solutions can be chosen for that. Furthermore, the fractional STO problem is also resolved as it becomes a part of channel response. Only the CFO is the main contributor to the spread at the Doppler axis in our targeted indoor environment. From the pilot row, we can estimate the channel and simply apply division on the DT matrix to mitigate CFO. This step is named as the “Final Equalizations” step in Figure 2-23. Finally, after complete equalization, OTFS information symbols are demodulated and converted back into bitstream.

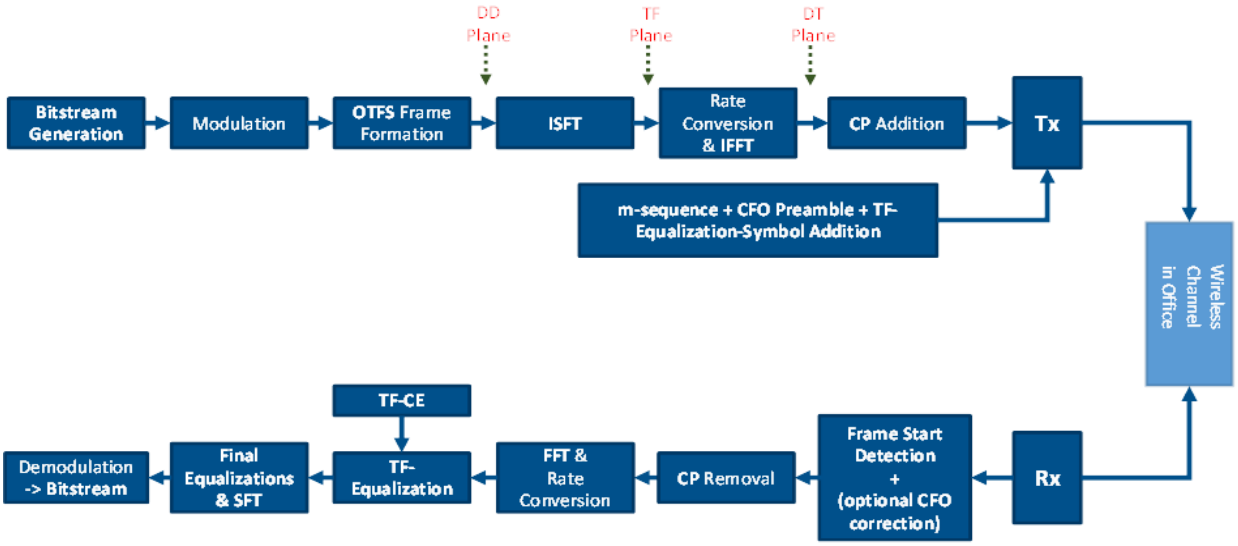

Figure 2-23 SDR-based OTFS system for an indoor office environment

Two USRPs were utilized to implement the experimentation. One USRP acts as a base station (named Tx USRP), which performs both communication and sensing tasks of an ISAC system simultaneously [26]. The second USRP (named Rx USRP) implements the communication receiver. No LO or reference clock sharing is provided between both USRPs. Synchronization, channel estimation, and all other receiver steps are performed with the received samples from USRP. This matches closely to the reality, where the user node only knows about the packet structure and preambles. The Rx USRP communicates via USRP Hardware Driver (UHD) with a Python script. This script is responsible firstly for performing the coarse synchronization, which enables it to get in the same transmission time window as the Tx USRP. After achieving initial synchronization, this script writes the samples to a file, which is immediately processed in MATLAB for further processing.

USRP X310 provides a maximum supported rate of 200 MSPs, which is utilized for our setup, and our OTFS system works with 150 MHz bandwidth. A subcarrier spacing Δf of 195.3125 kHz was selected, with 75% of the subcarriers allocated for data and 25% for null tones. Two different types of experiments were performed. The first one includes fixing 4-QAM as the desired modulation scheme and then fixing software gain of 5 dB for Tx USRP. The receiver system is then operated with different gains by setting the gain in software for the Rx USRP. BER and EVM are measured, and the system performance is demonstrated. The second experiment involves setting the Tx and Rx gains in the script at 5 dB and 23 dB respectively, while choosing BPSK, 4-QAM, and 16-QAM modulation schemes to validate the usability of various modulation schemes in the system. Table 2-2 provides the system constraints, and Figure 2-24 illustrates our setup in the indoor office environment.

Table 2-2 System Constraints

Constraints	Value
Carrier Frequency	5.150 GHz
Sampling Frequency	200 MSPs
Data Bandwidth	150 MHz
$\acute{M}$ Total Subcarriers	1024
M Delay bins	768
N Doppler bins	128
Subcarrier Spacing	195.3125 kHz
Tx Gain	0 dB

Figure 2-24 OTFS SDR System in indoor Office Environment

Table 2-3 System constraints for the experiments

Constraints	Value in Experiment 1	Value in Experiment 2
Rx Gain (dB)	[0, 1, 2, …, 12] and [0, 3, 6, …, 27]	23
Modulation Scheme	4-QAM	BPSK, 4-QAM & 16-QAM

Constraints for both experiments are illustrated in Table 2-3. Figure 2-25 displays the resulting graphs, in which Figure 2-25 a) shows the BER percentage and Figure 2-25 b) shows the EVM percentage vs. the Rx gain set in the script for USRP. Figure 2-25 c) displays EVM percentage results with Rx gain ranging from 0 dB to 27 dB.

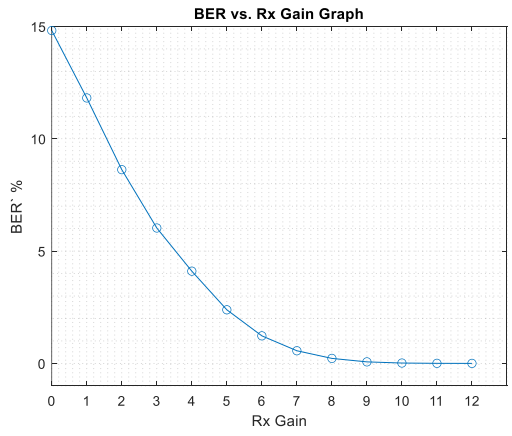

a)

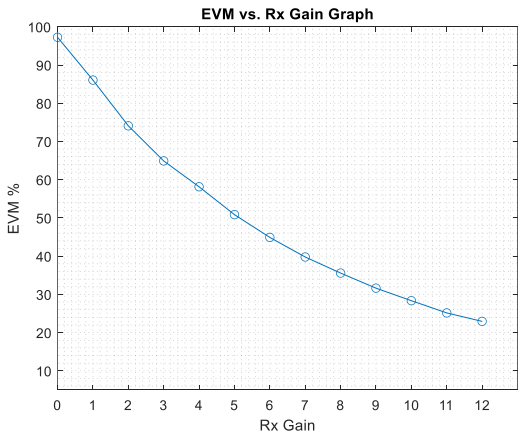

b)

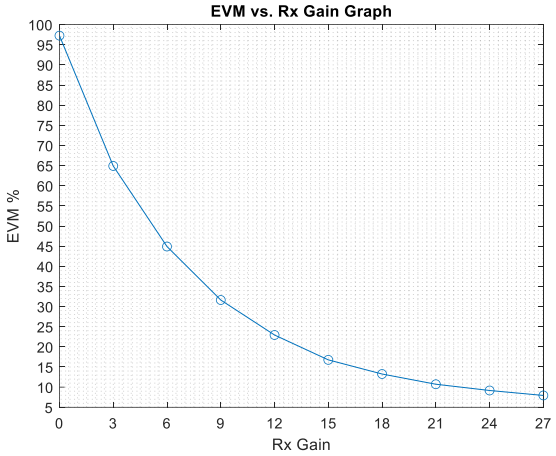

c)

Figure 2-25 Results of Experiment 1: (a) Resulting BER vs. Rx Gain. (b) Resulting EVM vs. Rx Gain. (c) Resulting EVM vs. Rx Gain at different Rx gains

Figure 2-26 displays the resulting constellation diagrams for our transmitted BPSK, 4-QAM, and 16-QAM symbols. It is evident from 16-QAM results, that in the current setting, higher modulation schemes (above 16-QAM) will require higher SNR.

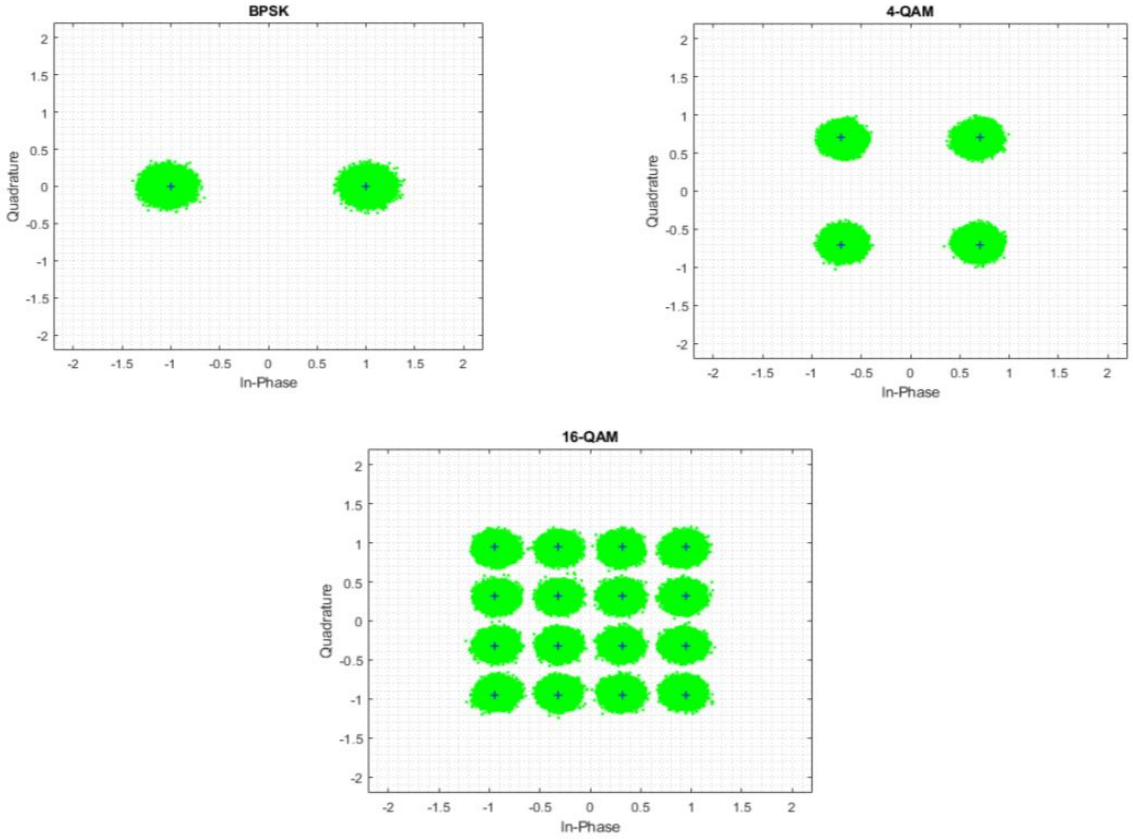

Figure 2-26 Results of Experiment 2. All of the selected modulation schemes are successfully recovered at receiver.

2.3.2.2 OTFS Sensing with SDR

In this case, we consider the case of sensing at a base station, which utilizes monostatic operation. The Local Oscillator (LO) can be shared internally between the transmitter and receiver processing chains. Moreover, multiple USRPs can also be utilized, as they can be synchronized via an external clock [24]. With a single USRP, the transmitter and receiver channel can be controlled via UHD driver in software, and synchronization can be achieved. Via UHD driver, multiple USRPs can be aligned in time, phase and frequency.

The residual effects from the connectors, front-end and antennas can also impact sensing results. These effects generally can impact the accuracy of results, as they cause SNR degradation. The impact from such components is mostly static and once analyzed, can be successfully minimized via pre-equalization. As the targeted implementation is based on SFT, low-complexity pre-equalization can be utilized in the TF plane.

A single USRP was utilized to implement our OTFS-based sensing system. A script was written to utilize UHD drivers for synchronization, and the received sensing samples from the device were imported into MATLAB for OTFS processing. The system parameters are demonstrated in Table 2-4. UBX-160 daughterboard was used in USRP X310, which provides a maximum bandwidth of 160 MHz and a maximum 6 GHz carrier frequency. The maximum supportable sampling rate of 200 MSps was utilized, with an occupied bandwidth of 150 MHz. This was done by choosing 768 data carriers out of a total of 1024. In the script, the gain of the transmitter chain was set at 0 dB, while the gain of the receiver chain was set to 23 dB. The transmitter power was chosen to test the minimum achievable accuracy at close targets. To prevent ADC saturation, maximum receiver gain was not utilized.

Table 2-4 System Parameters

Constraint	Value
f_c Carrier Frequency	5.250 GHz
Bandwidth B	150 MHz
F_s Sampling Frequency	200 Msps
Δf Subcarrier Spacing	195.3125 kHz
Cyclic Prefix Time T_{cp}	0.67 µs
M' Total Subcarriers	1024
M Occupied Subcarriers	768
N Symbols	128
Δd Range resolution	1 m
Δv Doppler resolution	38.55 m/s
L_D Factor for Periodogram in Delay	32
L_v Factor for Periodogram in Doppler	8
Tx Gain	0 dB
Rx Gain	23 dB

A combination of two antennas, with one having a wideband and the second one having a highly directed radiation pattern was chosen. Figure 2-27 shows the transmitter and receiver sensing antennas, along with the used USRP X310. This combination provided the optimal results with good accuracy.

The experiments were performed in both an office environment and in an anechoic chamber. Metal plates were used as reflectors for demonstration. In both scenarios OTFS RADAR was able to accurately detect targets. A high accuracy was achieved in both anechoic chamber and office scenarios for a single target.

The office scenario is illustrated in Figure 2-27. The scenario inside the anechoic chamber only contains the reflections from the desired targets. However, in an office scenario, it is different. There are multiple reflectors present in the environment, e.g., walls, floors, tables, doors, etc. These unwanted reflections can degrade the results, viz. accuracy of results. For the office scenario, multiple background sensing results were recorded. These background results were normalized and subtracted from the final results. Figure 2-28 presents the single and multi-target results.

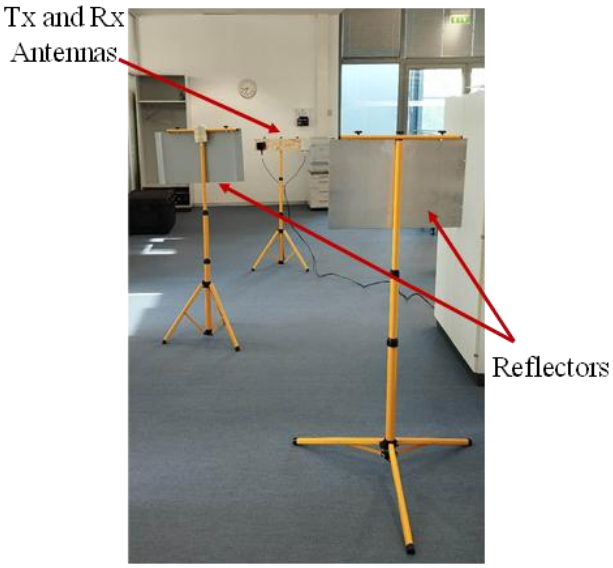

Figure 2-27 Office Scenario used for the sensing evaluation of OTFS

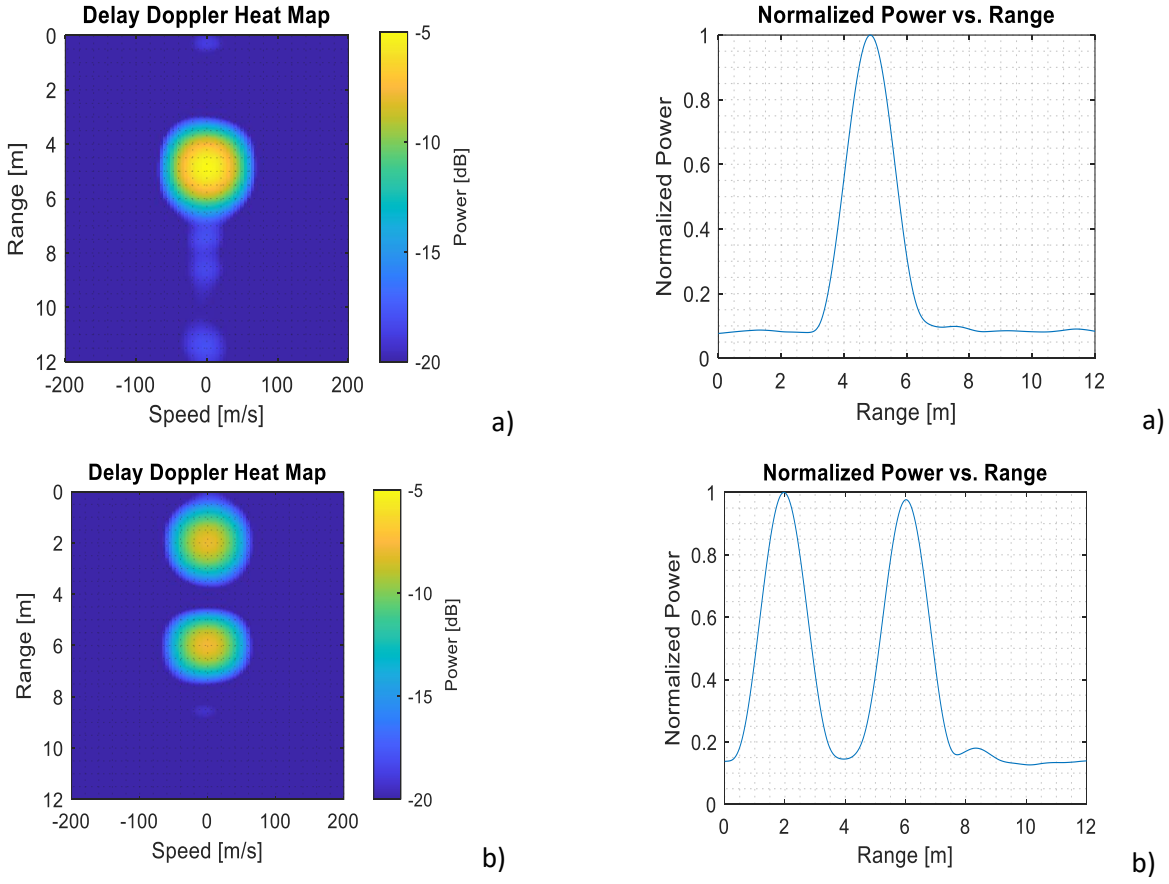

Figure 2-28 Sensing results in Office scenario: (a) single target, (b) two targets.

Multiple measurements were performed to verify the correct operability of the implemented OTFS-based sensing function. The difference in the results in the anechoic chamber and the office compared to the actual distance is illustrated in Figure 2-28 for a single target. Inside the anechoic chamber and office, for both scenarios, an accuracy of ±4 cm is achieved.

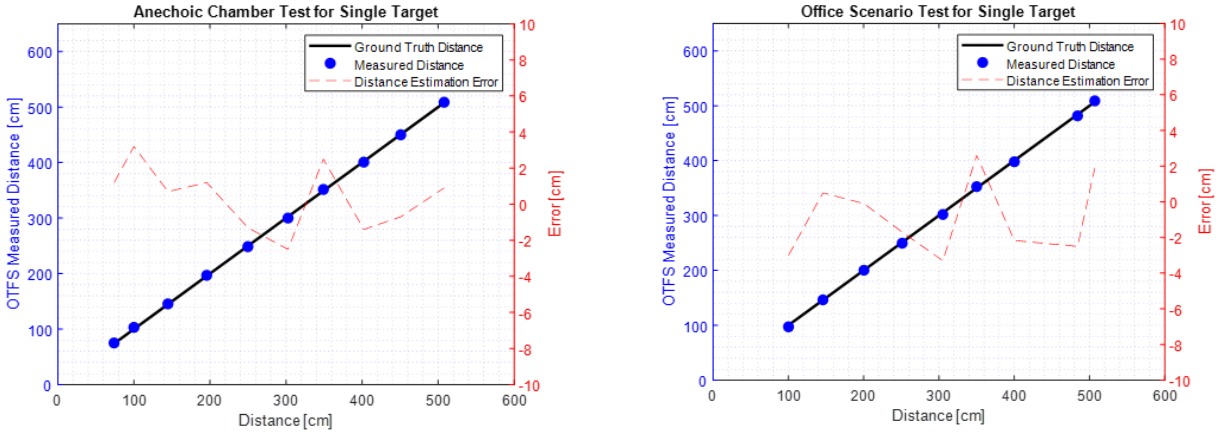

Figure 2-29 a) Anechoic chamber test for a single target, b) Office scenario test for a single target

3. Cell-Free MIMO activities

This section summarizes the CF-MIMO activities within the project, covering experimental CF-MIMO testbed investigations at **TUBS** and simulation-based algorithmic studies on CF-MIMO URA performed at **IHP**.

3.1 CF-MIMO Implementation

The CF-MIMO testbed developed at **TUBS** is dedicated to physical-layer research, with a particular focus on distributed signal processing, synchronization mechanisms, and cooperative beamforming. The detailed hardware architecture and implementation aspects have already been presented in deliverable **D3.1** [3]. Therefore, in **D3.2**, we only summarize the key system configurations of the testbed and focus primarily on experimental observations and performance plots under different operational modes. In this deliverable we briefly summarize the overall CF-MIMO testbed architecture and then focus on the three configurations supported by the current platform depicted in Figure 3-1.

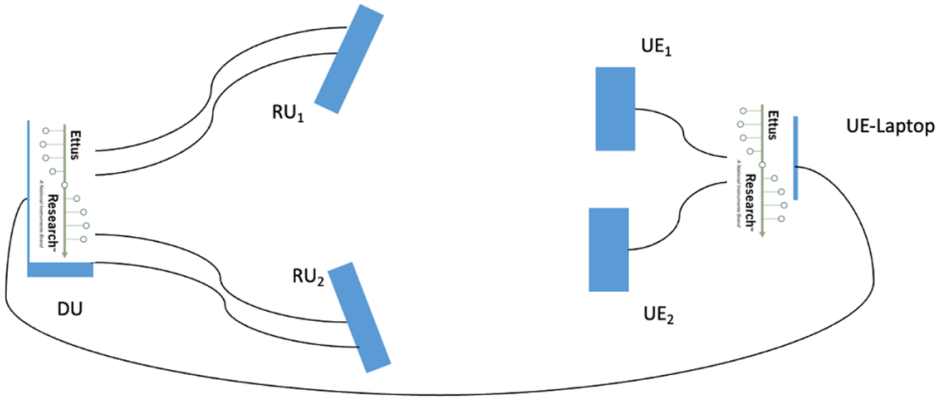

Figure 3-1 Massive MIMO System for CF-MIMO – Setup

The setup in Figure 3-1 provides a global view of the physical testbed, consisting of one centralized DU connected to two distributed RUs, which jointly serve two UEs. The setup illustrates how the DU, fronthaul, RUs, and UE are interconnected in the experimental platform. This section provides investigations on the three configurations of the platform, leaving the final integration details and experimental evaluation for **WP5** deliverables.

3.1.1 Configurations of the CF-MIMO platform

We investigate three transmission configurations implemented in the current platform, each representing a different level of cooperation between the two RUs.

3.1.1.1 Configuration A — Baseline (Non-Cooperative Transmission)

We consider two independent vector channels,

$$\mathrm{h}_{11} \in \mathbb{C}^{n_{\mathrm{tx}} \times 1}, \mathrm{h}_{22} \in \mathbb{C}^{n_{\mathrm{tx}} \times 1}, \tag{3-1}$$

representing the downlink channels from RU_1 to UE_1 and from RU_2 to UE_2, respectively. A single channel realization is assumed to be fixed during the SNR sweep.

Each RU applies maximum ratio transmission (MRT) based on its local CSI. The MRT beamforming directions are given by

$$\bar{\mathrm{w}}_1 = \frac{\mathrm{h}_{11}^*}{\| \mathrm{h}_{11} \|}, \bar{\mathrm{w}}_2 = \frac{\mathrm{h}_{22}^*}{\| \mathrm{h}_{22} \|}. \tag{3-2}$$

In this model, the transmit power is incorporated into the beamforming vectors. The beamformers are defined as

$$\mathrm{w}_1(p) = \sqrt{\frac{p}{2}}\,\bar{\mathrm{w}}_1, \mathrm{w}_2(p) = \sqrt{\frac{p}{2}}\,\bar{\mathrm{w}}_2, \tag{3-3}$$

where p denotes the SNR parameter in linear scale. Under this normalization, the total transmit power is given by

$$\| \mathrm{w}_1(p) \|^2 + \| \mathrm{w}_2(p) \|^2 = \frac{p}{2} + \frac{p}{2} = p. \tag{3-4}$$

Hence, the total transmit power is constrained to a parameter. It is parameterized by the SNR variable p. By varying p, the system performance can be evaluated over different SNR operating points while maintaining a consistent power normalization across all considered transmission schemes. Since no interference is present in the baseline configuration, the received signals at UE_1 and UE_2 are noise-limited. With the noise power normalized to unity, the resulting Signal-to-Interference-plus-Noise Ratios (SINRs) are

$$\mathrm{SINR}_1(p) = | \mathrm{h}_{11}^H \mathrm{w}_1(p) |^2, \ \mathrm{SINR}_2(p) = | \mathrm{h}_{22}^H \mathrm{w}_2(p) |^2. \tag{3-5}$$

The achievable rates of the two users are therefore

$$R_1(p) = \log_2(1 + \mathrm{SINR}_1(p)), \ \ R_2(p) = \log_2(1 + \mathrm{SINR}_2(p)). \tag{3-6}$$

The achievable sum-rate of the baseline scheme is given by

$$R_{\mathrm{sum}}(p) = R_1(p) + R_2(p). \tag{3-7}$$

The *SINR* sweep is performed by varying the scalar parameter p.

$$p = 10^{\mathrm{SNR_{dB}}/10}. \tag{3-8}$$

In this mode, the two RUs operate fully independently. RU_1 exclusively serves UE_1, and RU_2 exclusively serves UE_2, each relying solely on locally estimated CSI to compute its beamforming weights. Since all processing is performed per-RU without any exchange of phase information or channel estimates, no synchronization or coordination between RUs is required.

This configuration is straightforward to implement and robust to synchronization imperfections; however, it cannot exploit any cooperative gain across the distributed RUs. This baseline scheme corresponds to the lowest curve in the sum-rate versus *SINR* performance comparison and serves as a reference for evaluating the gains achieved by cooperative transmission strategies.

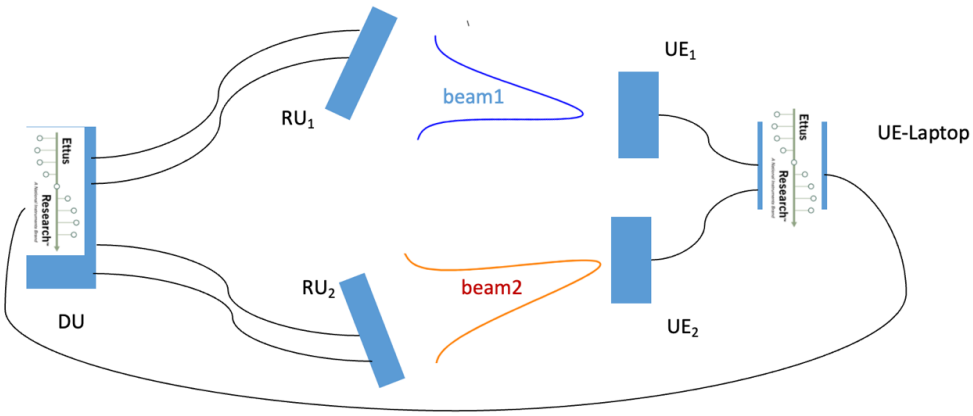

Figure 3-2 Configuration A: Two RUs serve two different UEs separately through beamforming

3.1.1.2 Configuration B — Cooperative Transmission on the Same RB (MISO-BC Model)

In this configuration, the two distributed RUs are jointly treated as a single multi-antenna transmitter. The downlink can therefore be modeled as a Multiple-Input Single-Output (**MISO**) **broadcast channel (MISO-BC)**, where the two UEs correspond to independent receivers served over the same time-frequency resource.

The joint beamforming vector applied at both RUs is constructed as a linear combination of the individual beamformers:

$$\mathbf{w} = \sqrt{\mathrm{p}_1}\mathbf{w_1} + \sqrt{\mathrm{p}_2}\mathbf{w_2} \tag{3-9}$$

where $\boldsymbol{w_1}$ and $\boldsymbol{w_2}$ denote the beamforming directions associated with UE_1 and UE_2, and p_1 and p_2 represent represent the allocated transmit powers subject to a total power constraint $\mathrm{p}_{\mathrm{total}}$. The powers satisfy:

$$\mathrm{p}_1 + \mathrm{p}_2 \leq \mathrm{p}_{\mathrm{total}} \tag{3-10}$$

The objective of this configuration is to determine the beamforming weights that maximize the system sum-rate:

$$\max_{w_1, w_2, p_1, p_2} R_1 + R_2 \tag{3-11}$$

subject to the total transmit power constraint.

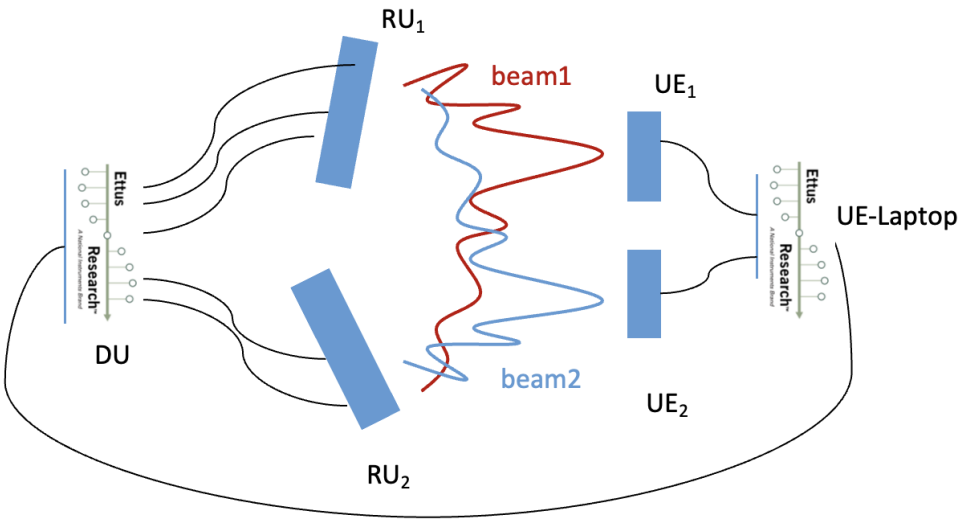

Figure 3-3 Configuration B: both RU_1 and RU_2 are serving UE_1 and UE_2 on the same RB

3.1.1.3 Configuration C — Phase-Aligned Multi-Beamsteering Transmission

In this configuration, depicted in Figure 3-4, each distributed RU independently serves both UEs using separate beamsteering vectors, while being subject to its own transmit power constraint. Unlike Configuration B, the RUs are not jointly treated as a single transmitter; instead, each RU allocates its local transmit power across multiple beams.

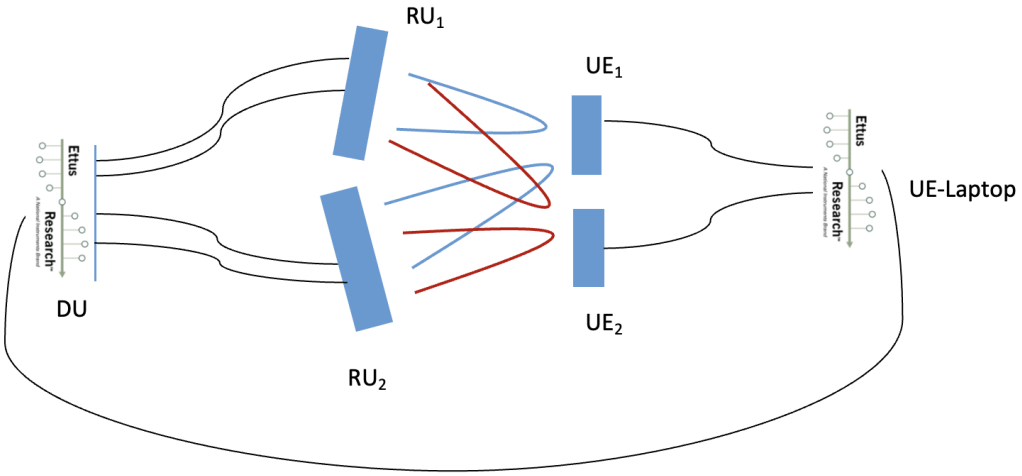

Figure 3-4 Configuration C: both RUs serve both UEs with different beams, accounting for synchronization and phase offsets

Each RU employs two beamforming directions, one for each UE.

Let v_{ij}denote the beamforming direction at RUi intended for UEj, where $i, j \in \{1,2\}$.

To maximize coherent signal combining, phase-aligned transmission is adopted. Specifically, the beamforming directions are chosen to compensate for the channel phase:

$$v_{ij} = e^{-j\angle h_{j,i}}, \tag{3-12}$$

where $h_{j,i}$denotes the channel coefficient from RU i to UE j.

Each RU distributes its available transmit power across the two beams. For RU_1, the effective transmit signal is

$$\mathbf{w}_1 = \begin{bmatrix} \sqrt{p_{11}}\, v_{11} \\ \sqrt{p_{21}}\, v_{21} \end{bmatrix}, p_{11} + p_{12} \le P_a, \tag{3-13}$$

where $p_{11}$and p_{12}denote the powers allocated by RU_1 to UE_1 and UE_2, respectively.

Similarly, for RU_2,

$$\mathbf{w}_2 = \begin{bmatrix} \sqrt{p_{12}}\, v_{12} \\ \sqrt{p_{22}}\, v_{22} \end{bmatrix}, p_{21} + p_{22} \le P_b. \tag{3-14}$$

In the simulations, equal per-RU power budgets are assumed:

$$P_a = P_b = \frac{P_{\text{total}}}{2}. \tag{3-15}$$

Each UE receives the superposition of the desired signal and the inter-user interference, which is treated as noise. The resulting SINRs are given by

$$\text{SINR}_1 = \frac{|\, \mathbf{h}_1^H \mathbf{w}_1 \,|^2}{\sigma^2 + |\, \mathbf{h}_1^H \mathbf{w}_2 \,|^2}, \text{SINR}_2 = \frac{|\, \mathbf{h}_2^H \mathbf{w}_2 \,|^2}{\sigma^2 + |\, \mathbf{h}_2^H \mathbf{w}_1 \,|^2}. \tag{3-16}$$

The achievable rates are

$$R_k = \log_2(1+\text{SINR}_k), k \in \{1,2\}. \tag{3-17}$$

The beamforming and power allocation parameters are jointly optimized to maximize the system sum-rate

$$\max_{\{p_{ij}\}} \; R_1 + R_2 \tag{3-18}$$

subject to the per-RU power constraints:

$$p_{11} + p_{12} \leq P_a,\; p_{21} + p_{22} \leq P_b. \tag{3-19}$$

Due to the low dimensionality of the power allocation variables, the optimization is solved via an exhaustive two-dimensional grid search over the per-RU power splits.

3.1.2 Simulation of the CF-MIMO Configurations

In this section, we evaluate the performance of the three transmission configurations introduced in the section 3.1.1, with a focus on the impact of different levels of cooperation, beamforming strategies, and synchronization constraints on the achievable sum-rate.

Figure 3-5 shows the achievable sum-rate versus SNR for the three considered transmission configurations. The cooperative MISO-BC scheme (Configuration B) achieves the highest sum-rate over the entire SNR range. By jointly designing the beamforming vectors and power allocation under a sum-rate, the system effectively exploits spatial cooperation and mitigates inter-user interference.

The baseline non-cooperative scheme (Configuration A) exhibits a moderate performance, where each RU serves a single UE independently using MRT beamforming. While no interference is present, the lack of cooperation limits the achievable spatial multiplexing gain.

Configuration C, which applies phase-aligned multi-beam transmission under per-RU power constraints, results in a lower sum-rate compared to both Configuration A and B. Although additional beams are transmitted, the per-RU power constraint and residual inter-user interference reduce the effective signal power per stream, leading to a more conservative sum-rate scaling with SNR.

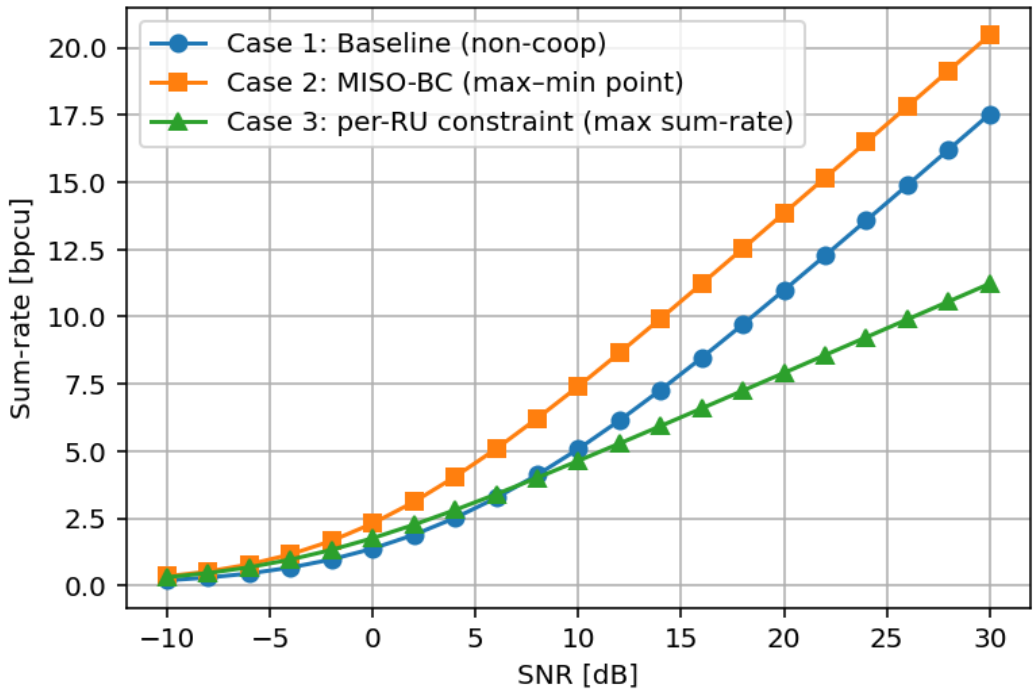

Figure 3-5 Comparison of Sum-Rate versus SINR for the three configurations

3.2 Unsourced Random Access in CF-mMIMO

As presented in deliverable D3.1 [3], we consider a CF scenario with several BSs and a massive number of users, where only Ka of them are active at any given time interval.

The received signal at each BS is processed to detect the transmitted pilot sequence and estimate the channel vectors and transmitted symbols. The transmitted symbols are then passed to the CPU to recover the message bits of the users.

At the CPU, the symbols belonging to the same active pilot indices from different BSs are combined. and the log-likelihood ratios (LLRs) of the corresponding message bits are extracted. The extracted LLRs are passed to a single-user polar decoder, and the decoded sequences satisfying the Cyclic Redundancy Check (CRC) check are added to the output list. After that, the successfully decoded messages are passed back to the BSs, where they are re-encoded and modulated, and their effects are subtracted from the received signal at the BSs. Then, the decoding operations are repeated using the residual signals. The decoding iterations continue until no new messages are decoded or a maximum number of predefined iterations are reached. The decoding process is illustrated in Figure 3-6.

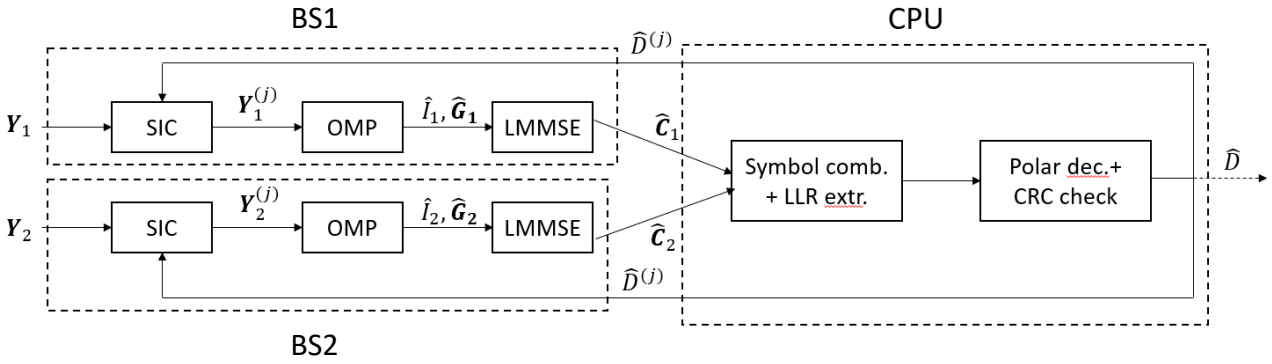

Figure 3-6 An illustration of the decoding process of the proposed scheme with two BSs and one CPU [27]

We evaluate the performance of the proposed scheme through Monte Carlo simulations. We set $n = 3200$ and $B = 100$. We assume that the BSs are randomly located in a $\mathrm{D} \times \mathrm{D}\ \mathrm{m}^2$ area according to a binomial point process, where $D = 550$. We employ Gaussian sequences as pilots, each element is selected from a zero-mean standard normal distribution. We utilize 5G polar codes with a code length of 1024, set the CRC length to 16, and the list size of the polar decoder to 8.

For the path-loss, the urban micro-cell propagation model in [8] is utilized with a center frequency of 2 GHz. Then, the large-scale fading coefficient $\beta_{i,m}$ can be written as

$$\beta_{\{i,m\}[dB]} = -30.5 - 36.7\, log_{10} d_{im} + \boldsymbol{F_{i,m}} \tag{3-20}$$

where d_{im} is the distance between the i-th user and the m-th BS, and $\boldsymbol{F_{i,m}} \sim CN(0,16)$ is the shadow fading. The small-scale fading coefficients are generated assuming a uniform linear array (ULA) at the BSs with half-wavelength antenna spacing.

We assess the effect of distributing the receive antennas in Figure 3-7 for $K_m = 7$ by evaluating the Per-User Probability of Error (PUPE) of the proposed scheme for $M = 1$ and $M_r = 100$, i.e., the centralized scenario, and comparing it with that of the two distributed scenarios where $M = 49$ and $M_r = 2$ and $M = 100$ and $M_r = 1$. We set the average symbol power to 10 mW and $\sigma^2 = -84$ dBm. The results in Figure 3-7 show that distributing the receive antennas significantly improves the system performance, as the PUPE decreases more than two orders of magnitude due to the fact that the system becomes more robust to the large-scale fading effects.

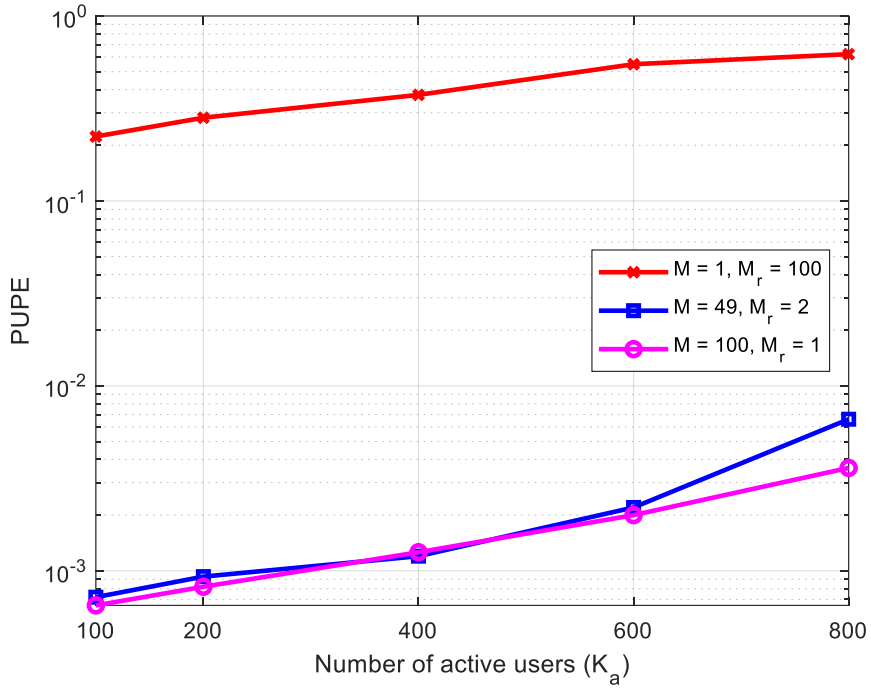

Figure 3-7 Comparison of PUPE versus the number of active users for different BS configurations

We investigate the effect of cooperation level on the system performance by comparing the performance of the proposed scheme with that of the scenario with no cooperation, i.e., each BS tries to decode K_m users without passing the symbol estimates to the CPU for $K_a = 200,800$, $M = 100$ and $M_r = 1$. The results in Figure 3-8 show that the cooperation between the BSs considerably improves the system performance as expected.

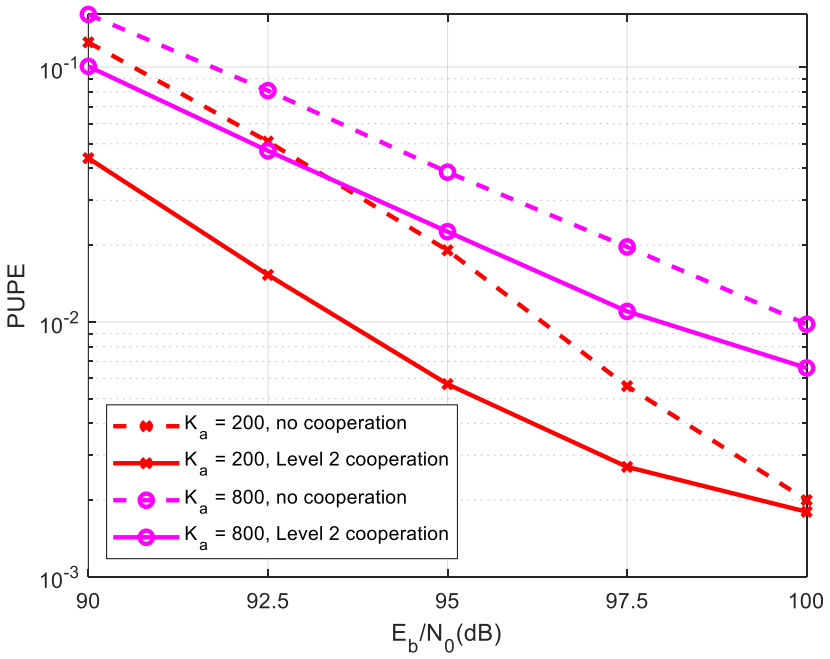

Figure 3-8 Comparison of PUPE between different cooperation levels

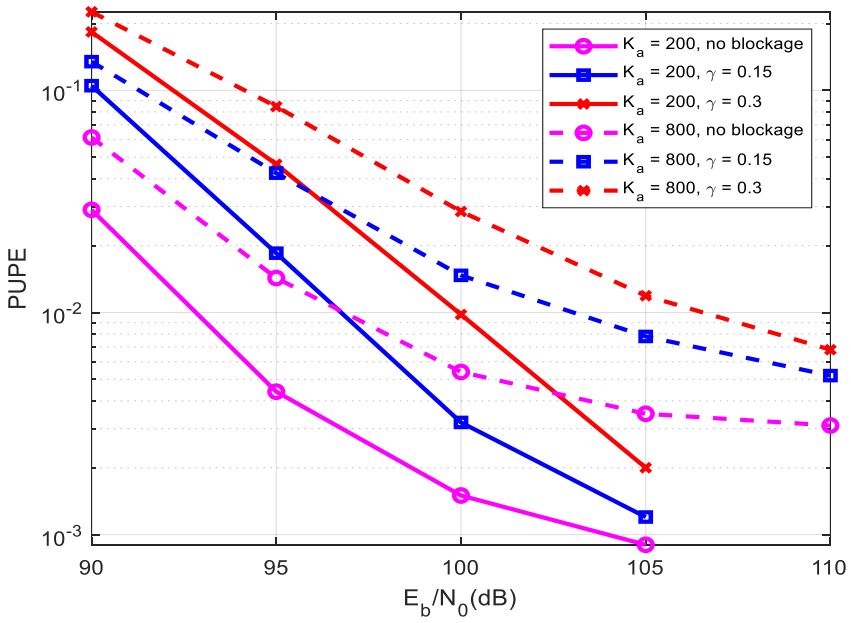

Figure 3-9 PUPE comparison of proposed scheme with and without blockage for $\gamma = 0.15, 0.3$.

We also explore the performance of the proposed scheme for the case that a user's transmission to an BS is blocked by a probability of γ in Figure 3-9 for $K_a = 200,800$ and γ = 0.15, 0.3. Note that even if a user's transmission to some BSs is blocked, its message can still be recovered by other BSs. The results in Figure 3-8 show that blockage degrades the system performance as expected; however, its effect is less pronounced for increasing E_b/N_0, especially for $\mathrm{K_a} = 200$.

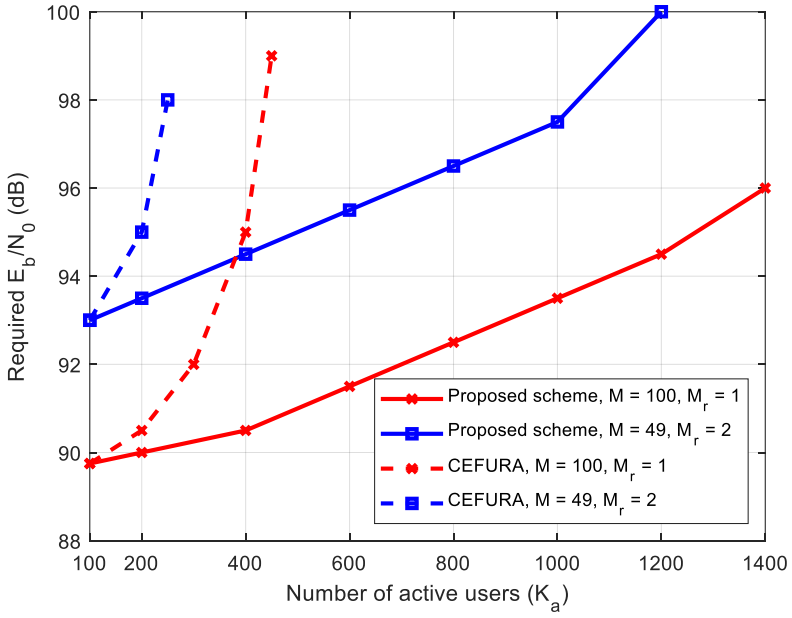

Figure 3-10 Comparison of the required E_b/N_0 versus the number of active users for PUPE $\mathrm{P_e} \leq 0.05$

Finally, we investigate the energy efficiency of the proposed scheme by calculating the required E_b/N_0 for a target PUPE of 0.05 and compare it with that of the scheme in [28] called CEFURA for K_m = 10. The required E_b/N_0 of the system can be calculated as

$$\frac{E_b}{N_0} = \frac{n_p P_p + n_d P_d}{B\sigma^2}. \quad (3\text{-}21)$$

where P_p and P_d are the symbol powers in the pilot and data part, respectively. The results in Fig. 6 demonstrate that our proposed scheme outperforms CEFURA by 4.5 dB for $K_a \leq 400$ for $M = 100$ and $M_r = 1$, and 1.5 dB for $K_a \leq 200$ for $M = 49$ and $M_r = 2$. In addition, it can support up to 1400 users for $M = 100$ and $M_r = 1$, and up to 1200 users for $M = 49$ and $M_r = 2$.

4. RIS support for improved spectral and energy efficiency

This chapter summarizes the work carried out in 6G-SENSES related to the design, optimization, and experimental evaluation of RISs in various 6G use cases. The state of the art of RIS technology, the main applications, and the integration of RIS in CF-MIMO systems and ISAC systems were described in deliverable **D3.1** [3]. In [3], we also reported initial research on beyond-diagonal RIS (BD-RIS) architectures, which increase the flexibility of the standard diagonal RIS (D-RIS) architecture, and their ability to minimize interference, RIS-based Offset Index Modulation, and active RIS in digital twin (DT)-based Ultra-Reliable Low-Latency Communications (URLLC) Internet-of-Things (IoT), among other topics. In this chapter, we expand and complete the report on scientific activities related to RIS design and its integration into the use cases envisaged in 6G-SENSES [4] and developed in the first 2 years of the project. Experimentation and testbed findings with RIS are initially presented, but most of the work will be conducted within **WP5**.

The chapter is structured as follows. In section 4.1 we present an outlook of the main research activities regarding RIS design. Section 4.2.1 describes the main RIS architectures that are being considered in the literature. The following sections briefly summarize the optimization problems considered, showing some illustrative results and drawing conclusions. In particular, spectral efficiency optimization is considered in section 4.2.2, energy efficiency optimization in URLLC networks is discussed in section 4.2.3, the combination of these two metrics to explore the trade-off between them is discussed in section 4.2.4, the synergies of RIS-assisted networks with advanced techniques such as Rate-Splitting Multiple Access (RSMA) are explored in section 4.2.5 and, finally, the results related to multi-RIS scenarios are presented in section 4.2.6.

4.1 Introduction and outlook

One of the WP3 building blocks in the 6G-SENSES architectural view is the use of RISs to improve some of the Key Performance Indicators (KPIs) identified by the R&D community as essential for 6G and detailed in deliverable **D2.1** [4]. RISs are passive (or nearly passive) metamaterial panels made of hundreds of low-cost, tunable cell elements that can dynamically control the reflection, refraction or absorption of incident electromagnetic waves. By intelligently adjusting the tunable elements (often using PIN diodes, or varactors), an RIS can modify wireless propagation environments, effectively turning walls or ceilings into programmable "smart mirrors" that focus, steer, or shape radio waves toward desired users while suppressing interference. As discussed in **D3.1** [3], RIS promises dramatic improvements in coverage, spectral efficiency, energy efficiency, without requiring additional active transmitters or excessive power consumption. Among the KPIs enhanced by RISs, in this chapter, we pay particular attention to the following:

- Spectral efficiency KPIs: increasing the capacity or throughput of links that may be weak or even blocked.
- Energy efficiency KPIs: reducing the transmission power required for a given performance (SINR, for example).
- SNR KPIs: boosting the received SNR, which can help meet the demanding requirements of 6G systems.

4.2 RIS simulation results

Most of the scenarios considered in this chapter are particular cases of the multi-cell MU-MIMO broadcast channel (BC) shown in Figure 4-1, which represents a multi-cell downlink channel composed of several multi-antenna Base Stations (BSs), each one serving several multi-antenna users. As is customary in many studies, we will assume perfect, instantaneous, and global CSI. Although this is an idealistic assumption, it will allow us to obtain the performance limits that can be achieved in RIS-assisted systems. The RIS capabilities depend on the hardware realization and variants such as simultaneously transmitting and reflecting (STAR) RIS

[30][31][32] and beyond diagonal (BD) RIS are studied [33]. RIS can also be intertwined with emerging technologies such as IoT, unmanned aerial vehicles (UAVs)-assisted systems, novel multiple access schemes such as RSMA, or URLLC systems using finite block length (FBL) coding. Among these aspects, we have paid particular attention to the analysis of different RIS architectures (RIS/BD-RIS/STAR-RIS), their optimization in URLLC systems, and the synergies resulting from their combination with multiple access strategies such as RSMA. Table 4-1 shows a summary of the results obtained in 6G-SENSES regarding RIS design and optimization, highlighting the RIS architectures, the scenarios in which they have been evaluated, the optimization criteria used in the design, and the main findings and partners involved in the derived publications. In this deliverable, we limit ourselves to the scientific results obtained in 6G-SENSES, the implementation and experimental evaluations on RIS will be described in deliverable D5.2 of WP5.

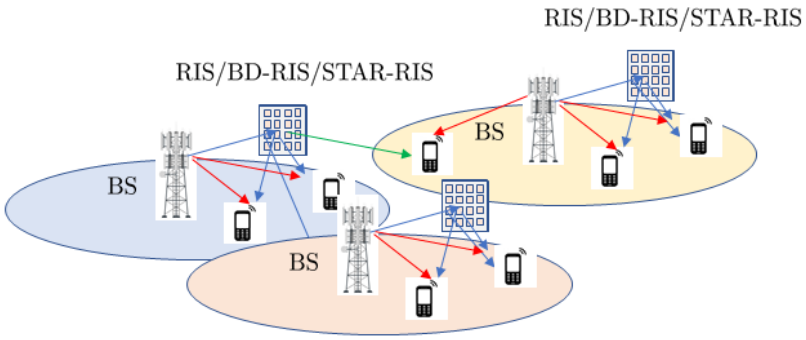

Figure 4-1 Multi-cell RIS-assisted MU-MIMO broadcast channel

Table 4-1 Summary of RIS architectures, considered scenarios, and optimization metrics (KPIs) indicating the references of the papers where they have been studied in detail

Derived publications	RIS architecture	Scenario	Optimization Criterion	Main findings	Partners
[35][36]	BD-RIS Locally passive	Point-to-point MIMO link, with unblocked direct link	Achievable Rate/Spectral Efficiency	i) Up to 20% Improvements wrt. to D-RIS. ii) Improvement increases with the number of streams, reflector elements, and Tx power	UC TUBS IHP
[38]	D-RIS/BD-RIS Locally passive	Point-to-point MIMO link with Line-of-Sight (LOS) through RIS channels	Achievable Rate/Spectral Efficiency	i) Closed-form solution for the BD-RIS. ii) Useful under Ricean channels with a weak direct link	UC IHP TUBS
[39]	D-RIS/Group-connected BD-RIS Locally passive/ globally passive	K-user MIMO Interference Channel/Multi-cell MU-MIMO	Interference leakage power	An optimized BD-RIS may increase the system's DoF by suppressing interference streams.	UC TUBS IHP
[40][41][42] [43][44]	D-RIS/BD-RIS/STAR-RIS Locally passive/ globally passive	MISO Broadcast Channel/ MU-MIMO URLLC system	Energy Efficiency maximization, Spectral Efficiency/Energy Efficiency Trade-off	i) In URLLC, RIS gains increase with more stringent require-ments. ii) The Energy Efficiency of BD-RIS highly depends on the static power consumption	UC TUBS
[45][46]	STAR-RIS Mode switching	MISO Broadcast Channel in URLLC	Fairness rate maximization/max-min rate with FBL coding + RSMA Max-min Energy Efficiency	i) STAR-RIS + RSMA contribute to enable URLLC in the downlink ii) STAR-RIS + RSMA enhances Energy Efficiency in URLLC scenarios	TUBS UC IHP

4.2.1 RIS architectures

RISs are commonly classified into three main architectures, based on how their reflecting elements manipulate the incident electromagnetic waves. *Diagonal-RIS* (also called conventional RIS) employs a diagonal phase-shift matrix in which each element can independently control only the phase (or the phase and amplitude) of its own reflected signal through a single tunable component (e.g., a PIN diode or varactor) [29]. *Beyond-diagonal RIS* (also known as fully-connected or multi-port RIS architectures) overcomes this limitation by using non-diagonal scattering matrices where each unit element is connected to multiple tunable impedances or ports, enabling mutually coupled control of amplitude and phase of reflected waves, thereby achieving higher flexibility and better performance at the cost of increased hardware complexity and power consumption [33]. To reduce the computational and circuit complexity of the fully-connected BD-RIS architecture, a group-connected architecture was proposed in [33]. The M reflective elements of a group-connected BD-RIS are partitioned into G groups, each of $M_g = M/G$ elements. The elements of each group are fully connected within their own group but remain disconnected from the other groups. *STAR-RIS* is a specialized BD-RIS that operates in full-space mode by supporting simultaneous reflection and refraction (transmission) toward both sides of the surface with independent phase and amplitude control for each direction; this is typically realized through multi-port elements or dual-surface designs, making STAR-RIS particularly suitable for full-coverage scenarios in 6G networks where users can be located on either side of the RIS panel [30][31][32].

Figure 4-2 shows a graphical representation of the different architectures studied in this deliverable and the structure of the resulting scattering matrix.

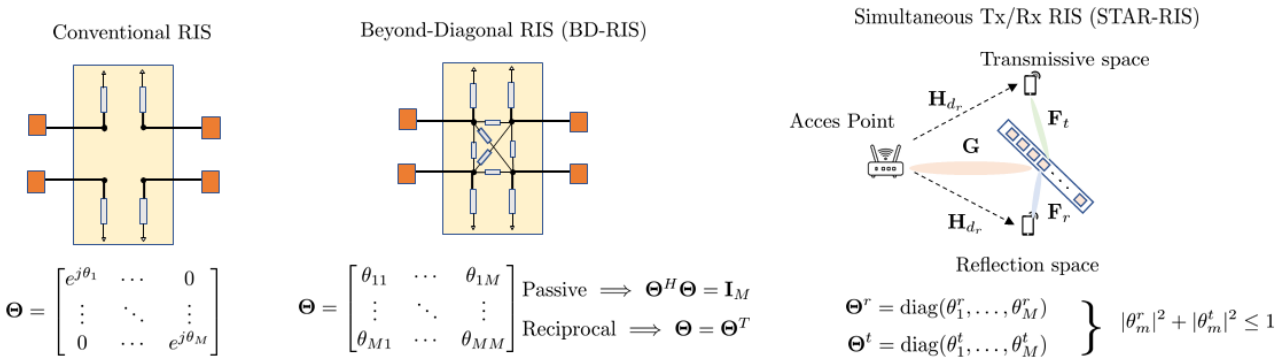

Figure 4-2 Diagonal-RIS (left), Beyond-diagonal RIS or BD-RIS (center), and Simultaneous Transmitting and Receiving RIS or STAR-RIS (right) architectures, indicating the constraints on the scattering matrix

The classical diagonal RIS constraint is given by [47]

$$T_1=\{\Theta=\text{diag}\left(e^{j\theta_1},\ldots,e^{j\theta_M}\right)\}. \tag{4-1}$$

The standard fully-connected BD-RIS constraint with symmetric (due to reciprocity) and unitary (lossless) RIS matrix is given by [33]

$$T_2=\{\Theta:\ \Theta^H\Theta=I,\quad \Theta=\Theta^T\}, \tag{4-2}$$

Whereas the STAR-RIS architecture providing full coverage yields to following RIS matrix

$$T_3=\begin{cases}\Theta^r=\text{diag}(\theta_1^r,\ldots,\theta_M^r)\\ \Theta^t=\text{diag}(\theta_1^t,\ldots,\theta_M^t)\end{cases}\qquad |\theta_m^r|^2+|\theta_m^r|^2=1. \tag{4-3}$$

The previous architectures, which are all passive and lossless, can be relaxed in their power constraint by making them locally passive, which translates into a generic restriction of the form $\boldsymbol{\Theta}^H\boldsymbol{\Theta}\leq\mathbf{I}$. Another relaxation

used in the literature and considered in our research is known as globally passive, which means that the power reflected by the surface must be less than the incident power (although some elements may amplify the power and others attenuate it). For a detailed description of all these restrictions, their formulation, and their implications for RIS design, we refer the reader to the related literature [48].

More recently, the optimal RIS architecture in terms of requiring the fewest number of tunable elements or circuit complexity has been shown to be the so-called Q-stem architecture [34][49], for which the number of tunable impedances grows approximately as MN_{DOF}, where M is the number of RIS elements and N_{DOF} represents the number of degrees of freedom of the system (i.e., the number of interference-free streams that the system supports). For comparison, the number of tunable impedances in the fully-connected BD-RIS architecture is M(M-1)/2.

4.2.2 Spectral efficiency maximization in BD-RIS-assisted MIMO systems

As a first illustrative example of the scenarios and problems considered within WP3 in 6G-SENSES, we consider the rate maximization of a MIMO link assisted by a BD-RIS, as depicted in Figure 4-3. The MIMO system, with N_T transmit antennas and N_R receive antennas, is assisted by a fully connected BD-RIS with M elements. The equivalent MIMO channel indicated also in Figure 4-3 is

$$H_{eq}(\Theta)=H_d+F\Theta G^H, \tag{4-4}$$

where $\boldsymbol{G}$ is the channel from the Tx to the BD-RIS, $\boldsymbol{F}$ is the channel from the BD-RIS to the Rx, $\boldsymbol{H_d}$ is the MIMO direct link, and $\boldsymbol{\Theta}$ is the BD-RIS scattering matrix with M elements, modelled as unitary (passive lossless) and symmetric (due to reciprocity).

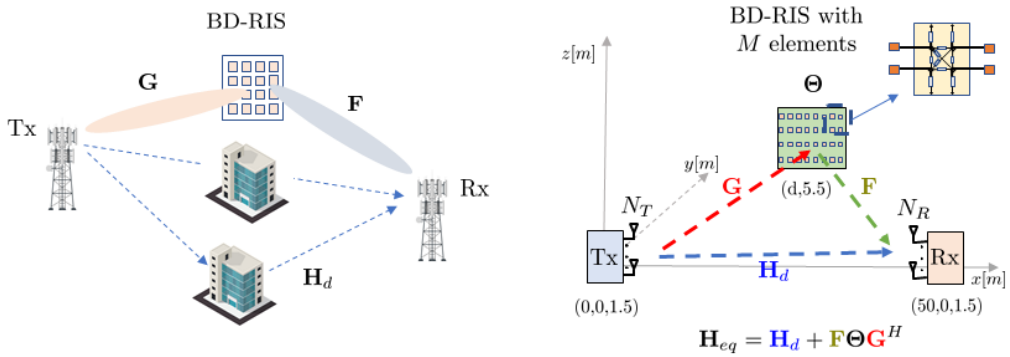

Figure 4-3 BD-RIS-assisted MIMO link. The left panel shows a typical deployment with the BD-RIS strategically deployed to have a dominant path (Ricean channels). The right panel shows the scenario used in the simulations.

For a fixed transmit covariance matrix, which can be absorbed into the equivalent channel given in (4-4), the rate maximization problem is

$$\max_{\Theta \in T_2} \; log\ det\left(I+\frac{1}{\sigma^2} H_{eq}(\Theta)H_{eq}(\Theta)^H\right), \tag{4-5}$$

which is a non-convex problem whose difficulty lies in the constraints that the scattering matrix, $\boldsymbol{\Theta}$, must satisfy. In [35][36], two algorithms with different levels of computational complexity have been proposed that allow us to obtain a stationary point of the cost function. The details of these algorithms can be found in the aforementioned publications.

As an example, in Figure 4-4, we show a simulation result obtained in a 4 x 4 MIMO system with the Tx located at coordinates (0,0,1.5) [m] and the Rx at coordinates (50,0,1.5) [m]. A fully-connected BD-RIS with M elements is located close to the Rx at coordinates (50,3,3) [m] to assist the Tx-Rx communication. The channels through the BD-RIS have a dominant line-of-sight (LoS) path and are therefore modelled as Rician

with factor K=3 and path loss exponent α = 2. The direct channel is modelled as a Rayleigh channel with path loss exponent that we take as α = 3.75 or α = 8 to model scenarios where the direct link is obstructed. The rest of the scenario parameters are taken from [35]. The results shown are the average of 200 independent simulations (channel realizations) keeping the Tx, Rx and BD-RIS positions fixed.

Figure 4-4 compares the achievable rate and the computational complexity of the following methods:

- The method proposed in [35], which applies a minorize-maximization (MM) algorithm and then optimizes the surrogate function using a manifold optimization (MO) algorithm on the manifold of unitary matrices (labeled as SPAWC'24).
- The method recently proposed in [36], which applies a new manifold optimization algorithm on the manifold of unitary *and symmetric* matrices (labeled as ICASSP'26).
- Some state-of-the-art competitors such as the method in [37], a suboptimal but closed-form solution with very low computational complexity, and an MO algorithm that disregards the symmetry constraint and then projects the solution.

As shown in Figure 4-4, the method in [36] provides optimal results with a computational cost comparable to that of the suboptimal method in [37], which does not work if there is no a sufficiently strong direct channel.

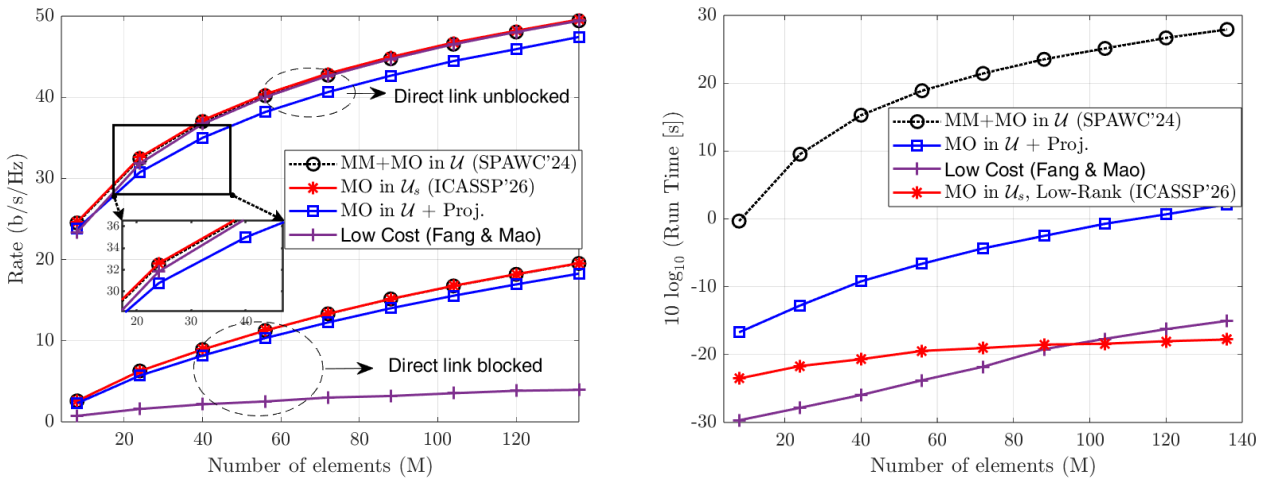

Figure 4-4 Rate (left panel) and computational complexity (right panel) vs number of BD-RIS elements in a 4x4 MIMO link

As part of the research carried out within 6G-SENSES, we have also considered a scenario of particular interest in which the channels to and from the BD-RIS, channels ***G*** and ***F*** in (4-4) are LoS while the direct link is non-line-of-sight (NLoS). LoS models are common in RIS-assisted scenarios [29], as it is a common scenario that occurs when the RIS has been deployed at a sufficient height. In [38], we derive an expression for the achievable rate in this situation that greatly simplifies the optimization problem and allows us to derive the optimal unitary and symmetric scattering BD-RIS matrix in closed form.

4.2.3 Energy efficiency maximization in MU-MIMO systems

Another set of 6G-SENSES research activities has been aimed at optimizing the different RIS architectures described in subsection 4.2.3 to achieve the energy-efficiency KPIs demanded by 6G. In this section, we present a brief summary of the main ideas and results described in [40][41][42][43][44][45][46], For further details, we refer the reader to these publications.

Let us consider a multi-cell RIS-assisted downlink channel comprising L BSs, as shown in Figure 4-1. Each BS has N_{BS} transmission antennas and serves K multiple-antenna users. Additionally, we assume that there are

L reflective passive RISs (one per cell) to assist the BSs, all of them for simplicity with M elements. A simplified model for the energy efficiency of user *k* is defined as

$$e_k = \frac{r_k}{P_c + \eta tr(Q_k)} \tag{4-6}$$

Where r_k is the transmission rate, η^{-1} is the power efficiency of the transmit devices at the BS and P_c is the constant power consumption of the system (including the devices of the BS, RIS and UE devices), and $\boldsymbol{Q}_k$ is the transmit covariance matrix for user k. Based on this expression, various problems involving the joint optimization of RISs and covariance matrices can be considered. A typical example is the maximization of the minimum energy efficiency, which amounts to solving

$$\max_{\{Q_k\},\ \{\Theta \in T_2\}} e \qquad s.t. \quad e_k = \frac{r_k}{P_c + \eta tr(Q_k)} \geq e \tag{4-7}$$

As we can see, these are complex fractional optimization problems, whose solution requires sophisticated optimization techniques, such as those described in [41][50]. Other cost functions, such as the global energy efficiency (energy efficiency summed over all users) or weighted versions of Eq. (4-7), have also been considered.

Within 6G-SENSES Use Case#2 (Ubiquitous Connectivity & Immersive Services) [4], a typical scenario is that of URLLC requiring extreme reliability (with packet error rate as low as 10^{-5} to 10^{-9}) and very short transmission delays (often targeted at 0.5 ms latency). URLLC scenarios often arise in industrial automation, autonomous vehicles, remote surgery, and tactile internet applications. URLLC scenarios make necessary to work on the so-called FBL coding regime, in which conventional Shannon's rate expressions are no longer valid. More specifically, FBL coding scenarios imply that the achievable rate follows an expression of the form [51]

$$r_k = log(1+\gamma_k) - Q^{-1}(\varepsilon)\sqrt{\frac{v_k}{n}}, \tag{4-8}$$

where *n* is the packet length, ε, is the decoding error probability and v_k is the channel dispersion term, and γ_k is the SINR for user *k,* which for single-antenna UEs is given by

$$\gamma_k = \frac{\left|h_k^H(\Theta)w_k\right|^2}{\sigma^2 + \sum_{i\neq k}\left|h_k^H(\Theta)w_i\right|^2}. \tag{4-9}$$

An achievable value for the channel dispersion term – in Eq. (4-8) – of Gaussian signals in interference-limited systems is [52]

$$v_k = 2\,\frac{\gamma_k}{1+\gamma_k}. \tag{4-10}$$

Therefore, the channel dispersion is a penalty term in the FBL rate expressions that must be considered in URLLC SE or EE optimization problems. A comprehensive framework for solving these problems can be found at [41]. As an example, Figure 4-5 shows the energy efficiency in a downlink channel in which a BS equipped with N_{BS} = 2 antennas serves K=6 users aided by a STAR-RIS. The users have 2 antennas each. Half of the users are in the reflection space of the RIS and the other half is in its refraction space. For URLLC the codeword length is *n*=256 bits and the packet error rate is $\varepsilon = 10^{-5}$. We observe that the STAR-RIS can substantially increase the sum energy efficiency of the network. Moreover, STAR-RIS outperforms reflective RIS when the users are located in both reflection and refraction spaces Additionally, STAR-RIS provides higher gains when there are more demanding latency and reliability constraints.

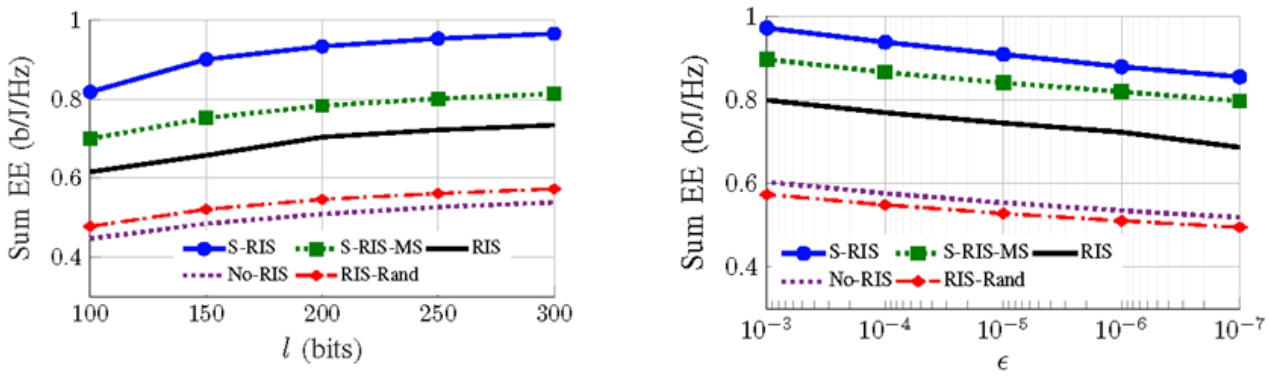

Figure 4-5 Energy-Efficiency vs. packet length (left) and decoding error probability (right) in a RIS-aided MU-MIMO system. The architecture is a STAR-RIS with M=60 elements operating in a mode-switching scheme.

4.2.4 SE/EE trade-off region

Optimizing the spectral efficiency with different RIS architectures as those described in Sec. 4.2.1 leads to the conclusion that more complex architectures (e.g., BD-RIS with a globally passive power constraint) logically lead to a higher spectral efficiency. On the other hand, the optimization of energy efficiency is clearly dependent on the RIS architecture considered, since each one has different circuitry and complexity requirements. And typically, the more complex architectures require higher (static) power. This raises the following question: does the spectral efficiency improvement provided by more complex RIS architectures justify the (possible) energy efficiency decrease caused by the additional circuitry required? This is the question we have posed in [43]. To answer it, we define the following metric to evaluate the Spectral-Energy-Efficiency trade-off

$$\zeta_k = \alpha r_k + \frac{(1-\alpha)\, r_k}{P_c + \eta tr(Q_k)}, \tag{4-11}$$

which can be optimized combining alternating optimization (AO) and the fractional matrix programming (FMP) solver proposed in [50].

A critical aspect to analyse the Spectral-Energy-Efficiency trade-off is how we model the static power consumption term in (4-11). To this end, we employ the model described in [42]

$$P_c = \frac{P_{BS}+P_{RIS}}{K} + P_{UE} = P_t + \frac{P_{RIS}}{K}, \tag{4-12}$$

where P_{BS}, P_{UE} and P_{RIS} are the static power consumption to operate the BS, the RIS and the UE, respectively. The static power of the RIS depends on the considered architecture (cf. Sec. 4.2.1) and the number of tunable impedances and reflecting elements. For a diagonal RIS architecture with M reflecting elements we have

$$P_{RIS} = P^D_{RIS,0} + M P^D_{RIS,n}, \tag{4-13}$$

where $P^D_{RIS,0}$ is the static power of the diagonal architecture, and $P^D_{RIS,n}$ is the static power of each tunable circuit, which for the diagonal architecture coincides with the number of reflecting elements. For a fully-connected BD-RIS architecture the static power model is

$$P_{BD\text{-}RIS} = P^{BD}_{RIS,0} + \frac{M(M-1)}{2} P^{BD}_{RIS,n}, \tag{4-14}$$

since the number of tunable impedances in this architecture grows as $M(M-1)/2$ with the number of elements M. This is the energy consumption model we have used in [41][42][43][44], which has allowed us to answer the question posed in this section.

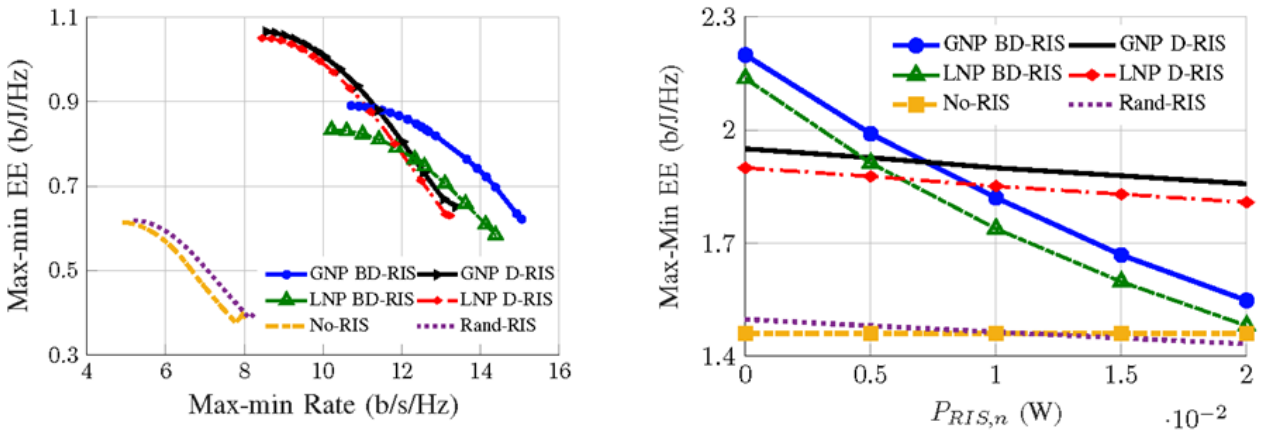

Figure 4-6 Left) Max-min energy efficiency vs. Max-min rate for different RIS architectures in a multi-cell downlink channel with 2 BSs and K=2 UEs per cell. Right) Max-min energy efficiency vs. static power consumption per tunable circuit.

As an example, Figure 4-6 shows the Spectral-Energy-Efficiency tradeoff of different passive RIS architectures in a MU-MIMO URLLC BC, and the impact of the static power consumption per circuit element on the energy efficiency. The BD-RIS enhances the max-min rate and energy efficiency compared to systems operating without RIS. However, BD-RIS may be less energy efficient than its diagonal counterpart, as BD-RIS has a much higher number of circuit elements, yielding a higher static power consumption. Hence, if the EE is the primary concern, the number of circuit elements enabling BD-RIS needs to be carefully optimized to account for the high static power consumption.

4.2.5 RIS-aided RSMA for URLLC networks

To address the challenges in dense URLLC communication networks to deliver the required service to multiple devices, RIS-assisted URLLC networks must also employ other advanced interference management techniques, such as RSMA [53]. In the simplest version of RSMA, the BS leverages a 1-layer rate-splitting (RS) design, where the message of each user is divided into two parts: common and private. The common message is intended to be detected by all users, whereas the private messages are detected only by their respective intended users. Careful resource allocation, encompassing beamforming and RIS optimization, is required to exploit the synergy between the three. In [45][46], we have studied in detail the combination of these technologies showing the resulting synergies. The optimization of the precoders for the common and private messages and the RIS is performed through an AO algorithm relying on minorization-maximization. Intrinsically, integrating RSMA with STAR-RIS in MU-MIMO BCs significantly enhances energy efficiency in URLLC scenarios. By formulating and solving a max-min energy efficiency optimization problem using an AO and the FMP framework of [33], the proposed energy-efficient scheme effectively addresses the challenges posed by stringent latency and reliability requirements. Numerical results show that the achievable second-order max-min rates of the proposed scheme outperform the baselines significantly. Multiple-Input Single-Output (MISO), RSMA, and STAR-RIS all contribute to enabling URLLC compared to the baseline schemes where only one or two technologies are used.

4.2.6 Multi-RIS models

Another extension of RIS-assisted networks is the use of multiple RIS to overcome obstacles and enable communications with users who do not have a direct LoS to the transmitter. Multiple-RIS can be used in this scenario, as depicted in Figure 4-7, where the transmitter and receiver do not have a LoS channel, as it is blocked by the geometry. Instead, two RISs are deployed to forward the signal. However, because the RISs are passive and do not fully radiate the impinging power towards the intended direction, a non-negligible fraction of the field from *RIS 2* “leaks” back toward *RIS 1*.

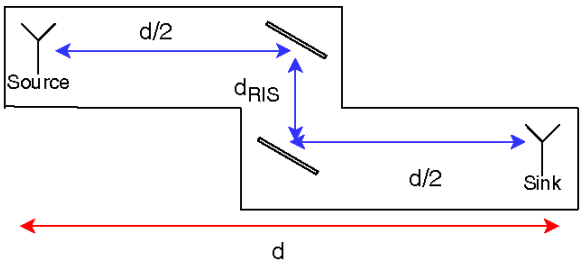

Figure 4-7 Multi-RIS scenario

This establishes a recursive scattering loop, referring to as the ping-pong effect between *RIS 1* and *RIS 2*, which creates multiple higher-order bounces and substantially modifies the effective E2E channel. In [54] we have studied this, usually neglected, ping-pong effect in multi-RIS links, developing to this end a proper physical modelling. By proper modelling and exact solution in the Single-Input Single-Output (SISO) case, we show that the ping-pong effect has an impact on the optimal RIS strategy and also effects the achievable performance.

As an illustrative example, we consider the scenario in Figure 4-7, where the Tx is located at coordinates (0, d_{RIS}, 2) [m], the Rx has coordinates (d, 0, 2) [m], RIS 1 is at (d/2, d_{RIS}, 2) [m] and RIS 2 is at (d/2, 0, 2). Thus, the distance along the x-axis between Tx and Rx is d [m] and the distance along the y-axis between RIS is d_{RIS} [m]. Both RISs are uniform planar arrays with element separation $\lambda/2$ and M=100 elements. The carrier frequency is fc = 10 GHz, the bandwidth is B = 20 MHz and the power transmitted is P = 1 W. The channels *S ->RIS 1* and *RIS 2 -> D* are modeled as Rician with factor K=3 and path loss exponent α = 3. The two RIS are close to each other and, therefore, the *RIS 1 -> RIS 2* link is modeled as a near-field channel according to the model in [55], with a path loss exponent α = 2. The results shown are the average of 200 independent simulations (channel realizations) keeping the Tx, Rx and RISs positions fixed as in Figure 4-7.

Figure 4-8 left) shows the rate achieved by the three channel models: i) considering the ping-pong effect and the specular component resulting from a physically-compliant RIS modelling [56], ii) without the ping-pong effect but with the specular component (two signal paths), and iii) without the ping-pong effect and without the specular component (standard one signal path). The RIS are unitary matrices with a global phase difference optimized to maximize the equivalent channel gain using the numerical procedure described in [54]. We observe that the ping-pong channel allows for a slight improvement in the rate, but the ping-pong effect quickly disappears as the distance between RIS increases.

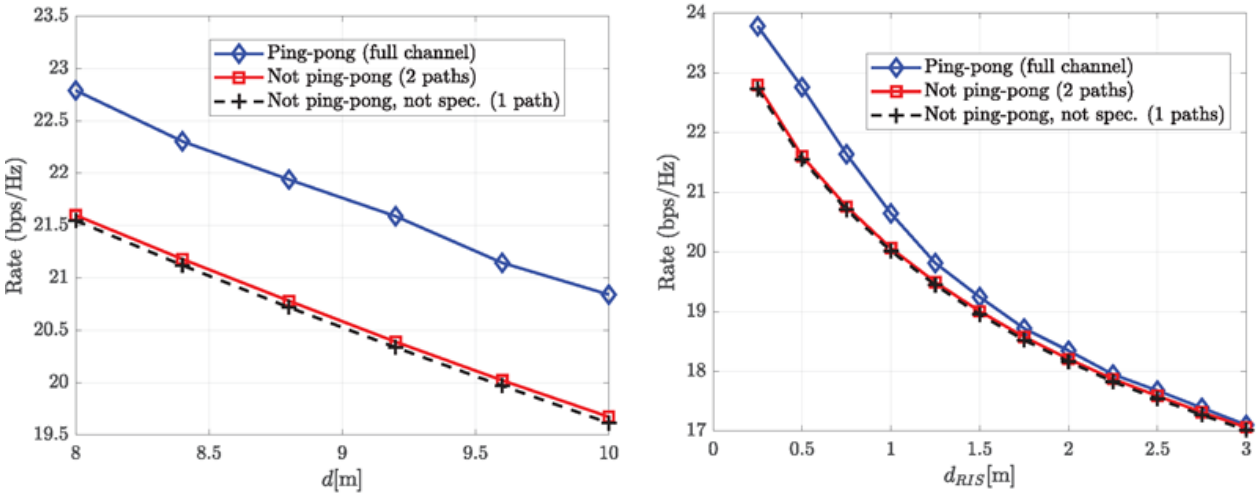

Figure 4-8 left) Achievable rate of the different channel models versus d (Tx-Rx distance on the x-axis) for a fixed dRIS = 0.5 [m]. right) Achievable rate of the different channel models versus dRIS (distance between RISs on the y-axis) for a fixed d=8 [m].

4.3 Laboratory Implementation of RIS-assisted CF-mMIMO

To experimentally evaluate the influence of RISs on indoor wireless propagation, a set of controlled measurements was carried out using a programmable RIS prototype. The setup consists of RISs positioned between a transmitter and receiver. All measurements were performed in a static laboratory environment to isolate the effect of RIS-induced reflections. Three representative link configurations were evaluated:

1. **Case 1. Transmitter ⟶ RIS ⟶ Receiver**
   Reflection without using the RIS functionality; this case serves as a reference (benchmark).
2. **Case 2: Transmitter ⟶ RIS ⟶ Receiver**
   Reflection using one activated RIS panel, as shown in Figure 4-9 a) and Figure 4-9 b).
3. **Case 3: Transmitter ⟶ RIS 1 ⟶ RIS 2⟶ Receiver**
   Reflection using two RIS panels with the RIS functionality turned off.
4. **Case 4: Transmitter ⟶ RIS 1 ⟶ RIS 2 ⟶ Receiver**
   Reflection using two activated RIS panels, as shown in Figure 4-10 a) and Figure 4-10 b).

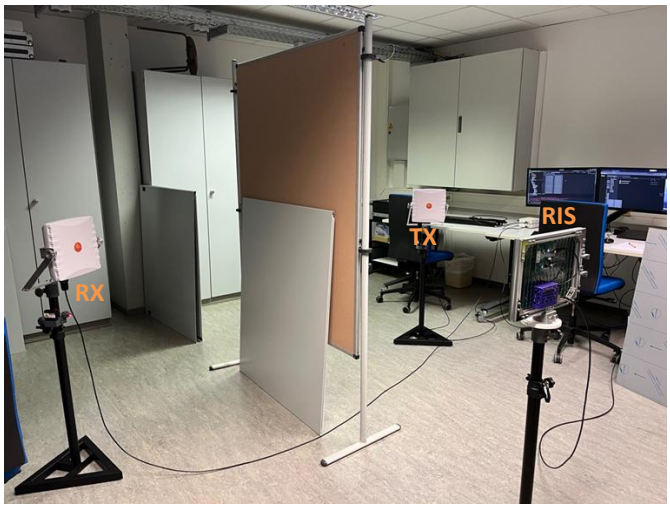

a)

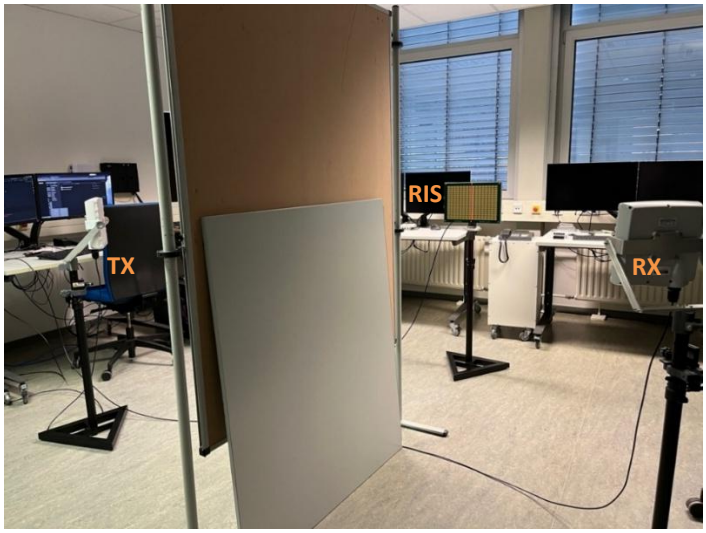

b)

Figure 4-9 a) View from the transmitter side, b) View from the receiver side

a)

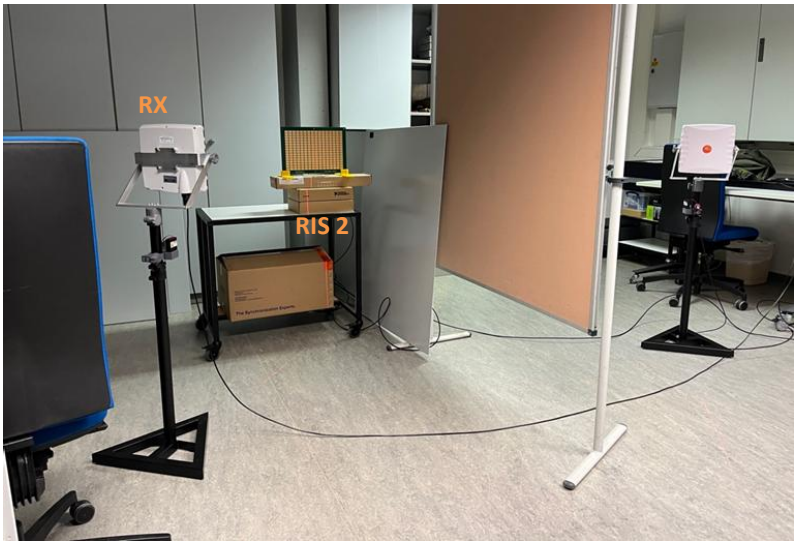

b)

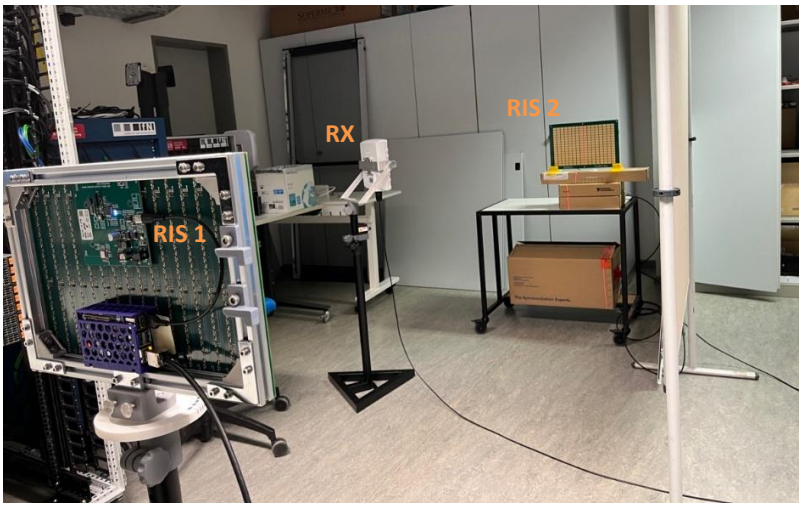

c)

Figure 4-10 a) View from the transmitter side, b) View from the first RIS side, c) View from the second RIS side

For each scenario, we recorded the instantaneous SNR over time, as well as its average value. The measured SNR traces for the four configurations are depicted in Figure 4-11, showing a clear degradation with increasing reflection complexity. These experiments highlight the practical effects of RIS placement and multi-hop reflections on achievable signal quality.

To better interpret the results in Figure 4-11, a single-RIS reference configuration with enabled RIS functionality is first considered. By selecting an incidence angle of 45° and a corresponding reflection angle of 45°, with the RIS panel oriented at 0°, the reflection geometry satisfies the law of reflection. Under this ideal condition, the reflected signal can be efficiently steered toward the receiver, leading to the maximum achievable SNR. This configuration is therefore used as a benchmark.

Next, the RIS position is modified such that the incidence angle changes to −13°, while the reflection angle toward the receiver remains fixed at 45° and the RIS orientation is unchanged. In this case, the reflection geometry no longer satisfies the ideal reflection condition. These configurations correspond to **Case 1** and **Case 2** measurements. When the RIS functionality is enabled, the received SNR decreases compared to the benchmark case due to the geometric mismatch. If the same configuration is maintained but the RIS functionality is disabled, the SNR further degrades, highlighting the contribution of active RIS phase control even under non-ideal reflection conditions.

For the **Case 3** and **Case 4** configurations, a cascaded reflection scenario is considered. The signal impinges on the *RIS 1* with an incidence angle of −43°, is reflected toward *RIS 2* arranged approximately orthogonally, and is finally reflected toward the receiver at an angle of 43°. In this dual-RIS setup, the use of RIS functionality results in a further reduction of the received SNR compared to the single-RIS cases, due to the increased propagation loss and reflection complexity. When the RIS functionality is disabled, no measurable SNR is observed, as the overall propagation geometry no longer satisfies the reflection conditions required for effective signal delivery.

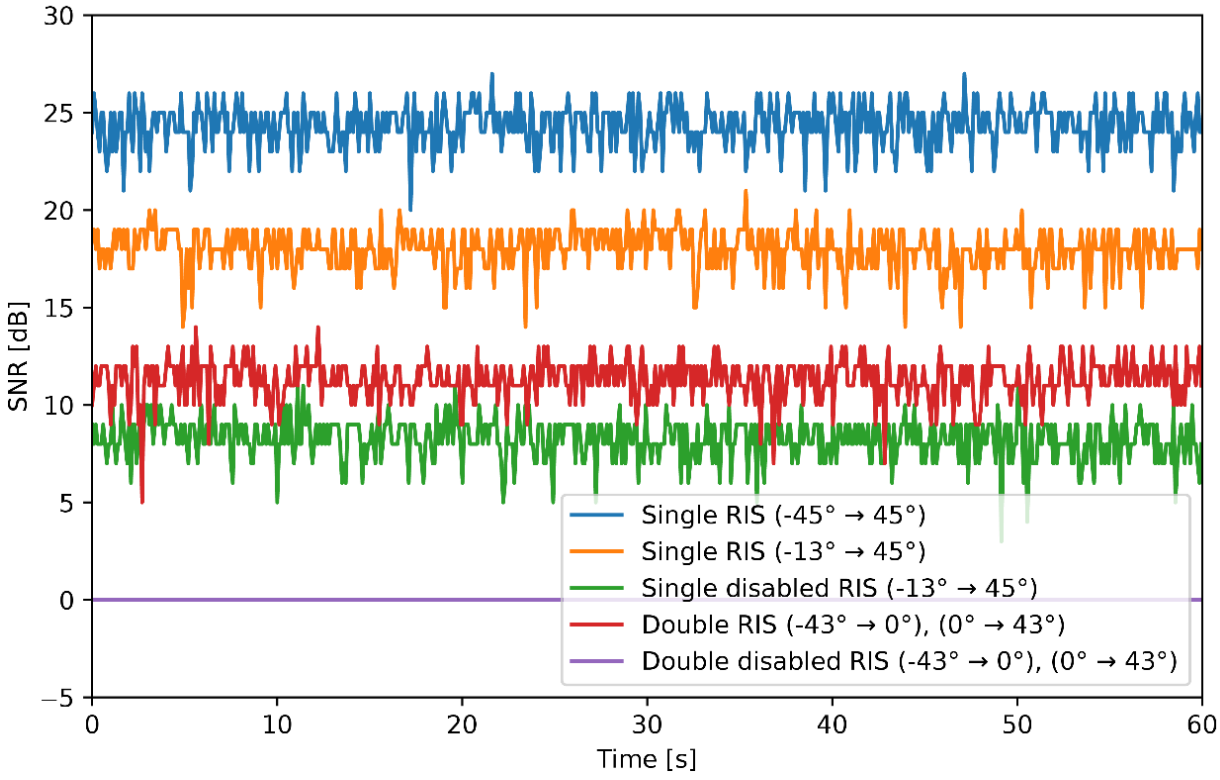

Figure 4-11 Results for all link configuration cases

5. Conclusions

This deliverable has presented the outcomes of **WP3** activities in the 6G-SENSES project, focusing on the development, implementation, and experimental validation of key infrastructure building blocks for future 6G systems. The work reported in **D3.2** consolidates advances in Cell-Free MIMO (CF-MIMO), Integrated Sensing and Communication (ISAC), and Reconfigurable Intelligent Surfaces (RIS), providing a coherent technical foundation for subsequent proof-of-concept (PoC) demonstrations.

ISAC-related developments demonstrate the practicality of joint communication and sensing across heterogeneous technologies and frequency bands. The investigated solutions span sub-6 GHz, mmWave, and Wi-Fi–based sensing, covering both 3GPP and non-3GPP access technologies. In particular, OTFS-based ISAC implementations have been experimentally validated on SDR platforms, highlighting robustness against multipath and Doppler effects in realistic indoor environments. Together, these results confirm that ISAC can be realized as a technology-agnostic framework capable of supporting diverse sensing functionalities while maintaining compatibility with future cellular architectures.

The CF-MIMO activities validate the feasibility of distributed radio access architectures through testbed-based implementations and experimental evaluations. Multiple cooperation configurations and processing modes have been investigated, demonstrating the benefits of distributed signal processing, synchronization, and coordinated transmission. These results confirm the suitability of CF-MIMO as a scalable and flexible enabler for high-capacity and reliable 6G access networks.

The RIS activities provide a comprehensive investigation of programmable radio environments, addressing spectral efficiency, energy efficiency, and reliability enhancement. Different RIS architectures, including d-RIS, BD-RIS, STAR-RIS, and multi-RIS configurations, have been analysed, highlighting both achievable performance gains and the impact of architectural complexity. The results underline the importance of accurate modelling and system-level considerations when deploying RIS-assisted links, particularly in NLoS and multi-hop scenarios.

Overall, **WP3** developments have reached a level of maturity that enables their use as technical inputs for the PoC activities planned in **WP5**. The validated architectures, experimental platforms, and performance insights reported in this deliverable provide a solid basis for system-level integration and further evaluation. As such, **D3.2** establishes a key milestone toward the realization of the 6G-SENSES vision, supporting the transition from foundational research to integrated PoC demonstrations in the last period of the project.

6. References

[1] 6G-SENSES deliverable D2.2, “System architecture and preliminary evaluations”, https://6g-senses.eu/wp-content/uploads/2025/11/2025-03-05-6G-SENSES_Deliverable_2_2_vf_pending_EU-review.pdf, March 2025.

[2] 6G-SENSES deliverable D2.3, “6G-SENSES architecture evaluation and benchmarking”, http://6g-senses.eu/wp-content/uploads/2026/01/2026-01-02-6G-SENSES_D2.3_v_final.pdf, January 2026.

[3] 6G-SENSES deliverable D3.1, “Initial report on the development of 6G-SENSES infrastructure building blocks”, January 2025, https://6g-senses.eu/wp-content/uploads/2025/07/2025-01-15-6G-SENSES_D3.1_v1_0-FINAL.pdf.

[4] 6G-SENSES deliverable D2.1, “Report on 6G-SENSES use cases, network architecture, KPIs and supported RAN functions”, September 2024, https://6g-senses.eu/wp-content/uploads/2024/10/2024-09-30-6G-SENSES_Deliverable_2_1_vf.pdf.

[5] F. Khan, L. Diez, N. Maletic, J. Gutiérrez, M. Petri, R. Agüero, “RIC meets ISAC: On ensuring sensing latency requirements over O-RAN”, submitted to ICC 2026.

[6] M. Irazabal and N. Nikaein, "TC-RAN: A Programmable Traffic Control Service Model for 5G/6G SD-RAN," in *IEEE Journal on Selected Areas in Communications*, vol. 42, no. 2, pp. 406-419, Feb. 2024, doi: 10.1109/JSAC.2023.3336162.

[7] C. -C. Chen, C. -Y. Chang and N. Nikaein, "FlexSlice: Flexible and real-time programmable RAN slicing framework," in *IEEE Global Communications Conference (GLOBECOM 2023)*, Kuala Lumpur, Malaysia, 2023, pp. 3807-3812, doi: 10.1109/GLOBECOM54140.2023.10437791.

[8] S. R. Zahran et al., "Bondwire Integration Challenges in E-band Systems: from PCB to Die Level," *2023 53rd European Microwave Conference (EuMC)*, Berlin, Germany, 2023, pp. 846-849, doi: 10.23919/EuMC58039.2023.10290383.

[9] B. Sutbas, H. J. Ng, M. H. Eissa and G. Kahmen, "A Low-Power V-Band Radar Transceiver Front-End Chip Using 1.5 V Supply in 130-nm SiGe BiCMOS," in *IEEE Transactions on Microwave Theory and Techniques*, vol. 71, no. 11, pp. 4855-4868, Nov. 2023, doi: 10.1109/TMTT.2023.3269519.

[10] M. Umar, M. Laabs, N. Neumann and D. Plettemeier, "Bondwire Model and Compensation Network for 60 GHz Chip-to-PCB Interconnects," in *IEEE Antennas and Wireless Propagation Letters*, vol. 20, no. 11, pp. 2196-2200, Nov. 2021, doi: 10.1109/LAWP.2021.3108499.

[11] S. D. Joseph and E. A. Ball, "Analysis of Bondwires and RF Compensation Circuits in E-Band," in *IEEE Transactions on Components, Packaging and Manufacturing Technology*, vol. 15, no. 9, pp. 1986-1995, Sept. 2025, doi: 10.1109/TCPMT.2025.3594505.

[12] J. Chen et al., "A 56–66-GHz FMCW Radar Transceiver With Wide Chirp Bandwidth for Indoor Sensing Applications," in *IEEE Transactions on Microwave Theory and Techniques*, doi: 10.1109/TMTT.2025.3633165.

[13] L. Lu et al., "Design of a 60-GHz Joint Radar–Communication Transceiver With a Highly Reused Architecture Utilizing Reconfigurable Dual-Mode Gilbert Cells," in *IEEE Transactions on Microwave Theory and Techniques*, vol. 73, no. 1, pp. 245-257, Jan. 2025.

[14] C. Xu et al., "A Packaged 54-to-69-GHz Wideband 2T2R FMCW Radar Transceiver Employing Cascaded-PLL Topology and PTAT-Enhanced Temperature Compensation in 40-nm CMOS," in *IEEE Journal of Solid-State Circuits*, vol. 59, no. 10, pp. 3156-3171, Oct. 2024.

[15] H. J. Ng, M. Kucharski, W. Ahmad and D. Kissinger, "Multi-Purpose Fully Differential 61- and 122-GHz Radar Transceivers for Scalable MIMO Sensor Platforms," in *IEEE Journal of Solid-State Circuits*, vol. 52, no. 9, pp. 2242-2255, Sept. 2017.

[16] 60 GHz radar sensor with antennas in package, BGT60UTR11AIP datasheet V1.3, Infineon, Feb. 2025.

[17] 6G-SENSES deliverable D5.1, "Testing Methodologies and Testbed Setup", November 2025, https://6g-senses.eu/wp-content/uploads/2025/11/2025-11-09-6G-SENSES_Deliverable_5_1_vf_pending_EU-review.pdf

[18] T. Thaj and E. Viterbo, "OTFS modem SDR implementation and experimental study of receiver impairment effects", in *IEEE International Conference on Communications Workshops*, ICC Workshops 2019 - Proceedings. https://doi.org/10.1109/ICCW.2019.8757167.

[19] R. Marsalek, J. Blumenstein, D. Schutzenhofer, and M. Pospisil, "OTFS Modulation and Influence of Wideband RF Impairments Measured on a 60 GHz Testbed", *IEEE Workshop on Signal Processing Advances in Wireless Communications, SPAWC*, *2020-May*. https://doi.org/10.1109/SPAWC48557.2020.9154257.

[20] M. Nauman, L. Lopacinski, N. Maletic, M. Scheide, M. Krstic, E. Grass, "6G and Beyond: Hardware-in-the-Loop Experiments with OTFS Modulation Using SDR", Workshop on Microwave Theory and Techniques in Wireless Communications (MTTW), 2023.

[21] M. Nauman, L. Lopacinski, N. Maletic, M. Scheide, J. Gutiérrez, M. Krstic, "OTFS Modulation: Synchronization Challenges, Solutions, and Experimental Results". *14th International ITG Conference on Systems, Communications, and Coding* (SCC 2025).

[22] P. Karpovich, T. P. Zielinski, R. Maksymiuk, P. Samczyński, K. Abratkiewicz, and P. Tomikowski, "Field Tests of a Random-Padded OTFSM Waveform in a Joint Sensing and Communication System", in *IEEE International Conference on Communications (ICC 2023)*, May, 6442–6448. https://doi.org/10.1109/ICC45041.2023.10279296.

[23] X. Wei, L. Zhang, W. Yuan, F. Liu and S. Li, "SDR System Design and Implementation on Delay-Doppler Communications and Sensing" in *IEEE Wireless Communications and Networking Conference, WCNC*, *2023-March*. https://doi.org/10.1109/WCNC55385.2023.10118889.

[24] *X300/X310 - Ettus Knowledge Base*. (n.d.). Retrieved June 6, 2023, from https://kb.ettus.com/X300/X310.

[25] TSGR. (2020). TS 138 211 - V16.2.0 - 5G; NR; Physical channels and modulation (3GPP TS 38.211 version 16.2.0 Release 16). https://portal.etsi.org/TB/ETSIDeliverableStatus.aspx

[26] M. Nauman, L. Lopacinski, N. Maletic, M. Scheide, J. Gutiérrez, M. Krstic, "OTFS Sensing with SDR: Experimental Results and Analysis", in *Proc. 101st IEEE Vehicular Technology Conference (VTC 2025)*.

[27] M. Özates, M. Kazemi, E. Jorswieck and D. Gündüz, "ODMA-Based Cell-Free Unsourced Random Access with Successive Interference Cancellation," in *IEEE 101st Vehicular Technology Conference (VTC2025-Spring)*, Oslo, Norway, 2025, pp. 1-5.

[28] M. Gkagkos, J.-F. Chamberland, C. N. Georghiades and K. R. Narayanan, "Scalable cell-free massive MIMO unsourced random access system", arXiv:2304.06105, 2023.

[29] Q. Wu, S. Zhang, B. Zheng, C. You and R. Zhang, "Intelligent reflecting surface-aided wireless communications: A tutorial," in *IEEE Transactions on Communications*, vol. 69, no. 5, pp. 3313-3351, May 2021, doi: 10.1109/TCOMM.2021.3051897.

[30] Y. Liu et al., "STAR: simultaneous transmission and reflection for 360° coverage by intelligent surfaces," *IEEE Wireless Communications*, vol. 28, no. 6, pp. 102-109, December 2021, doi: 10.1109/MWC.001.2100191.

[31] J. Xu, Y. Liu, X. Mu, R. Schober and H. V. Poor, "STAR-RISs: A correlated T&R phase-shift model and practical phase-shift configuration strategies," *IEEE Journal of Selected Topics in Signal Processing*, vol. 16, no. 5, pp. 1097-1111, Aug. 2022, doi: 10.1109/JSTSP.2022.3175030.

[32] "GR RIS 006 V1.1.1: Simultaneously transmitting and reflecting RIS" ETSI, Tech. Rep., June. 2025.

[33] H. Li, S. Shen and B. Clerckx, "Beyond diagonal reconfigurable intelligent surfaces: From transmitting and reflecting modes to single-, group-, and fully-connected architectures," *IEEE Transactions on Wireless Communications*, vol. 22, no. 4, pp. 2311-2324, April 2023, doi: 10.1109/TWC.2022.3210706.

[34] X. Zhou, T. Fang and Y. Mao, "A novel Q-stem connected architecture for beyond-diagonal reconfigurable intelligent surfaces," *IEEE International Conference on Communications (ICC 2025)*, Montreal, QC, Canada, 2025, pp. 6880-6885, doi: 10.1109/ICC52391.2025.11162091.

[35] I. Santamaria, M. Soleymani, E. Jorswieck and J. Gutiérrez, "MIMO capacity maximization with beyond-diagonal RIS," *2024 IEEE 25th International Workshop on Signal Processing Advances in Wireless Communications* (SPAWC), Lucca, Italy, 2024, pp. 936-940, doi: 10.1109/SPAWC60668.2024.10694491.

[36] I. Santamaria, M. Soleymani, E. Jorswieck, J. Gutiérrez and C. Beltrán, "Riemannian optimization on the manifold of unitary and symmetric matrices," submitted to *51st International Conference on Acoustics, Speech, and Signal Processing, ICASSP 2026*, Barcelona, May 2026.

[37] T. Fang and Y. Mao, "A low-complexity beamforming design for beyond-diagonal RIS aided multi-user networks," *IEEE Communications Letters*, vol. 28, no. 1, pp. 203-207, Jan. 2024, doi: 10.1109/LCOMM.2023.3333411.

[38] I. Santamaria, J. Gutiérrez, M. Soleymani and E. Jorswieck, "Rate analysis and optimization of LoS beyond diagonal RIS-assisted MIMO systems," *IEEE Communications Letters*, vol. 29, no. 6, pp. 1325-1329, June 2025, doi: 10.1109/LCOMM.2025.3560380.

[39] I. Santamaria, M. Soleymani, E. Jorswieck and J. Gutiérrez, "Interference minimization in beyond-diagonal RIS-assisted MIMO interference channels," *IEEE Open Journal of Vehicular Technology*, vol. 6, pp. 1005-1017, 2025, doi: 10.1109/OJVT.2025.3555425.

[40] M. Soleymani, A. Zappone, E. Jorswieck, M. Di Renzo and I. Santamaria, "Rate region of RIS-aided URLLC broadcast channels: diagonal versus beyond diagonal globally passive RIS," *IEEE Wireless Communications Letters*, vol. 14, no. 2, pp. 320-324, Feb. 2025, doi: 10.1109/LWC.2024.3500100.

[41] M. Soleymani, I. Santamaria, E. A. Jorswieck, R. Schober, and L. Hanzo, "Optimization of the downlink spectral- and energy- efficiency of RIS-aided multi-user URLLC MIMO systems," *IEEE Transactions on Communications*, vol. 73, no. 5, pp. 3497-3513, May 2025, doi: 10.1109/TCOMM.2024.3480988.

[42] M. Soleymani, I. Santamaria, E. Jorswieck, M. Di Renzo and J. Gutiérrez, "Energy efficiency comparison of RIS architectures in MISO broadcast channels," *2024 IEEE 25th International Workshop on Signal Processing Advances in Wireless Communications* (SPAWC), Lucca, Italy, 2024, pp. 701-705, doi: 10.1109/SPAWC60668.2024.10694177.

[43] M. Soleymani, A. Zappone, E. Jorswieck, M. Di Renzo and I. Santamaria, "Spectral-energy efficiency tradeoff of nearly-passive in MIMO URLLC downlink: diagonal vs. beyond diagonal," *IEEE Wireless Communications Letters*, vol. 15, pp. 890-894, 2026, doi: 10.1109/LWC.2025.3641845.

[44] M. Soleymani, I. Santamaria, E. Jorswieck, R. Schober and L. Hanzo, "Energy efficiency optimization of finite block length STAR-RIS-aided MU-MIMO broadcast channels," *2025 IEEE 26th International Workshop on Signal Processing and Artificial Intelligence for Wireless Communications (SPAWC)*, Surrey, United Kingdom, 2025, pp. 1-5, doi: 10.1109/SPAWC66079.2025.11143431.

[45] M. Soleymani, I. Santamaria, E. Jorswieck, R. Schober and L. Hanzo, "STAR-RIS-aided RSMA for the URLLC multi-user MIMO downlink," *2025 28th International Workshop on Smart Antennas (WSA)*, Erlangen, Germany, 2025, pp. 85-90, doi: 10.1109/WSA65299.2025.11202796.

[46] E. A. Jorswieck, M. Soleymani, I. Santamaria and J. Gutiérrez, "URLLC networks enabled by STAR-RIS, rate splitting, and multiple antennas," *International Conference on Mobile and Miniaturized Terahertz Systems (ICMMTS)*, Dubai, United Arab Emirates, 2025, pp. 1-5, doi: 10.1109/ICMMTS62835.2025.10926047.

[47] M. Di Renzo et al., "Smart radio environments empowered by reconfigurable intelligent surfaces: How it works, state of research, and the road ahead," *IEEE Journal on Selected Areas in Communications*, vol. 38, no. 11, pp. 2450-2525, Nov. 2020, doi: 10.1109/JSAC.2020.3007211.

[48] R. K. Fotock, A. Zappone and M. D. Renzo, "Energy efficiency optimization in RIS-aided wireless networks: active versus nearly-passive RIS with global reflection constraints," *IEEE Transactions on Communications*, vol. 72, no. 1, pp. 257-272, Jan. 2024, doi: 10.1109/TCOMM.2023.3320700.

[49] Z. Wu and B. Clerckx, "Beyond-diagonal RIS in multiuser MIMO: Graph theoretic modeling and optimal architectures with low complexity," *IEEE Transactions on Information Theory*, vol. 71, no. 11, pp. 8506-8523, Nov. 2025, doi: 10.1109/TIT.2025.3609435.

[50] M. Soleymani, E. Jorswieck, R. Schober and L. Hanzo, "A framework for fractional matrix programming problems with applications in FBL MU-MIMO," *IEEE Transactions on Wireless Communications*, doi: 10.1109/TWC.2025.3590162.

[51] Y. Polyanskiy, H. V. Poor and S. Verdú, "Channel coding rate in the finite blocklength regime," *IEEE Transactions on Information Theory*, vol. 56, no. 5, pp. 2307-2359, May 2010, doi: 10.1109/TIT.2010.2043769.

[52] J. Scarlett, V. Y. F. Tan and G. Durisi, "The dispersion of nearest-neighbor decoding for additive non-Gaussian channels," *IEEE Transactions on Information Theory*, vol. 63, no. 1, pp. 81-92, Jan. 2017, doi: 10.1109/TIT.2016.2620161.

[53] B. Clerckx et al., "A primer on rate-splitting multiple access: tutorial, myths, and frequently asked questions," *IEEE Journal on Selected Areas in Communications*, vol. 41, no. 5, pp. 1265-1308, May 2023, doi: 10.1109/JSAC.2023.3242718.

[54] E. A. Jorswieck, M. Soleymani, I. Santamaria and J. Gutiérrez, "Physics-compliant three-hop RIS models: specular component and ping-pong effect," submitted to *2026 International Conference on Mobile and Miniaturized Terahertz Systems (ICMMTS)*, Skukuza, South Africa, 2026.

[55] M. Haghshenas, P. Ramezani, M. Magarini and E. Björnson, "Parametric channel estimation with short pilots in RIS-assisted near- and far-field communications," *IEEE Transactions on Wireless Communications*, vol. 23, no. 8, pp. 10366-10382, Aug. 2024, doi: 10.1109/TWC.2024.3371715.

[56] J. A. Nossek, D. Semmler, M. Joham and W. Utschick, "Physically consistent modeling of wireless links with reconfigurable intelligent surfaces using multiport network analysis," *IEEE Wireless Communications Letters*, vol. 13, no. 8, pp. 2240-2244, Aug. 2024, doi: 10.1109/LWC.2024.3410528.

7. Acronyms

Acronym	Description
AO	Alternating Optimization
AoA	Angle-of-Arrival
API	Application Programming Interface
BC	Broadcast Channel
BD	Beyond-Diagonal
BD-RIS	Beyond-Diagonal RIS
BS	Base Station
CBF	Coordinated Beamforming
CCC	Cell Configuration Control
CFO	Carrier Frequency Offset
CHE	Channel Coefficient
CIR	Channel Impulse Response
COTS	Commercial Off-The-Shelf
CRC	Cyclic Redundancy Check
CSI	Channel State Information
D-RIS	Diagonal RIS
DA	Driver Amplifier
DFT	Discrete Fourier Transform
DGS	Defected Ground Structure
DMRS	Demodulation Reference Signal
DoF	Degree of Freedom
DT	Digital Twin
DU	Distributed Unit
E2AP	E2 Application Protocol
E2E	End-to-End
E2SM	E2 Service Model
FBL	Finite Block Length
FFT	Fast Fourier Transform
FMP	Fractional Matrix Programming
gNB	gNodeB
GUI	Graphical User Interface
IC	Integrated Circuit

IE	Information Element
IFFT	inverse Fast Fourier Transform
IoT	Internet-of-Things
KPI	Key Performance Indicator
KPM	Key Performance Measurement
LCL	inductor-capacitor-inductor
LLC	Low Layer Control
LLR	Log-Likelihood Ratio
LO	Local Oscillator
LoS	Line-of-Sight
LTF	Long Training Field
MISO	Multiple-Input Single-Output
MO	Manifold Optimization
MRT	Maximum Ratio Transmission
NIC	Network Interface Card
NLoS	Non-Line-of-Sight
OAI	OpenAirInterface
OFDM	Orthogonal Frequency-Division Multiplexing
OTA	Over-The-Air
OTFS	Orthogonal Time Frequency Space
PA	Power Amplifier
PCB	Printed Circuit Board
PDSCH	Physical Downlink Shared Channel
PoC	Proof of Concept
PUPE	Per-User Probability of Error
RADAR	Radio Detection and Ranging
RC	RAN Control
RIS	Reconfigurable Intelligent Surface
RS	Rate-Splitting
RSMA	Rate-Splitting Multiple Access
RU	Radio Unit
SA	Standalone
SCTP	Stream Control Transmission Protocol
SDK	Software Design Kit
SDR	Software Defined Radio

SEE	Spectral Energy Efficiency
SiGe	Silicon Germanium
SINR	Signal-to-Interference-plus-Noise Ratio
SISO	Single-Input Single-Output
SLA	Service Level Agreement
SM	Service Model
SNR	Signal-to-Noise Ratio
SRS	Sounding Reference Signal
STAR-RIS	Simultaneously Transmitting and Reflecting RIS
STO	Sampling Time Offset
TDD	Time Division Duplex
UAVs	Unmanned Aerial Vehicles
UHD	USRP Hardware Driver
URLLC	Ultra-Reliable Low-Latency Communications
USRP	Universal Software Radio Peripheral
VCO	Voltage Controlled Oscillator
WAT	Wireless Access Technology